

Copyright
by
Matthew Michael Andringa
2006

**The Dissertation Committee for Matthew Michael Andringa certifies that this
is the approved version of the following dissertation:**

Unpowered Wireless Sensors for Structural Health Monitoring

Committee:

Dean P. Neikirk, Supervisor

Sharon L. Wood

Francis X. Bostick

John A. Pearce

Mircea D. Driga

Unpowered Wireless Sensors for Structural Health Monitoring

by

Matthew Michael Andringa, B.S.E.E.; M.S.E.

Dissertation

Presented to the Faculty of the Graduate School of

The University of Texas at Austin

in Partial Fulfillment

of the Requirements

for the Degree of

Doctor of Philosophy

The University of Texas at Austin

December 2006

Dedication

To Hayley, for her continuous love and support.

Acknowledgements

There are many individuals who have supported the work presented in this dissertation. Dr. Dean Neikirk has been an invaluable resource both as a technical advisor as well as a sounding board and mentor. Although conversations with him often meant more work for me, I believe he helped improve the quality of this work immensely. I also appreciate the help of all the members of Team Neikirk for their assistance with technical questions as well as the general support all graduate students need from one another.

Concrete is not often an area of in-depth study for electrical engineers. Dr. Sharon Wood and all of her students in Civil Engineering who have worked on this project, including Kristi Grizzle, Jarkko Simonen, Nate Dickerson, and John Puryear, have contributed a great deal to creating practical sensor designs and continually improving the design through thorough testing.

I'd also like to thank my parents and my fiancée, Hayley, for their continual support throughout my graduate school career. They were also kind enough to help with the editing of this document.

I have many more friends who have supported me along the way, providing simple words of encouragement and much needed stress-relief. Thanks Courtney for the constant check-ups on my progress. Finally, I'd like to thank my dog Raven, who sat by me throughout the writing process even though she would have rather been out going for walks in the beautiful fall weather.

This work was funded in part by the Texas Advanced Technology Program and the National Science Foundation.

Unpowered Wireless Sensors for Structural Health Monitoring

Publication No. _____

Matthew Michael Andringa, Ph.D.

The University of Texas at Austin, 2006

Supervisor: Dean P. Neikirk

The rapid advancement of wireless technology has allowed the development of new sensor technologies for many different applications. Unfortunately, many of the sensor systems have a substantial cost and require a continuous power source. A new class of sensors is proposed for use in situations where cost and long-term durability are of major concern. For example, corrosion of steel reinforced concrete is a worldwide problem, with potential damages estimated at billions of dollars in the United States alone. A simple low-cost resonant-based embeddable sensor platform is proposed. The sensor is wirelessly powered and interrogated through a magnetically coupled reader coil. The sensor circuit is analyzed and a series of design guidelines are developed. Two prototype sensors, one to detect corrosion of steel reinforcement in concrete and one to measure conductivity, are proposed and tested both in the laboratory as well as in actual reinforced concrete members. The use of the wireless platform for other types of sensors is also discussed. Results indicate that the sensor platform performs well and may aid in the early detection of corrosion in reinforced concrete.

Table of Contents

List of Tables	x
List of Figures.....	xi
CHAPTER 1 Introduction	1
1.1 Structural Health Monitoring.....	1
1.1.1 Reinforced Concrete Structures	2
1.2 Embedded Sensors	4
1.3 Scope of Work	5
CHAPTER 2 Design Considerations.....	7
2.1 Design Guidelines	7
2.1.1 Cost	7
2.1.2 Durability	8
2.1.3 Power and Communication.....	8
2.1.4 Reliability.....	8
2.2 Current Passive Wireless Sensors.....	9
2.2.1 EAS Tags	9
2.2.2 RFID Tags.....	11
2.3 Sensors in Concrete.....	13
2.3.1 Smart Pebble™	13
2.3.2 Smart Aggregate	14
2.3.3 ECI-1	14

CHAPTER 3 Sensor Basics.....	15
3.1 Sensor Platform.....	15
3.1.1 Capacitance Based Sensor	16
3.1.2 Resistance Based Sensor.....	20
3.2 Quality Factor	38
3.2.1 Resistance Dependence.....	41
3.2.2 Coupling Factor Dependence.....	43
3.2.3 Coil Resistance Effects	44
3.2.4 L and C Effects	49
3.3 Design Considerations	51
 CHAPTER 4 Embedded Corrosion Sensor.....	 54
4.1 Expanded Circuit Model	54
4.1.1 Physical Based Circuit Values	54
4.1.2 Coil Geometry Considerations.....	58
4.2 Curve Fitting	64
4.3 Corrosion Sensor.....	68
4.3.1 Reference Coil	69
4.3.2 Next Generation Prototype	73
4.3.3 Concrete Tests.....	78
4.3.4 Potential Improvements	83
 CHAPTER 5 Conductivity Sensor	 86
5.1 Concrete Resistivity	86
5.2 Modified Circuit Topology	89
5.3 Prototype Sensor	90
5.4 Salt Water Tests	93

5.5	Tests in Concrete.....	103
5.6	Curing Tests.....	108
5.7	Potential Improvements	115
5.8	Conclusions.....	117
CHAPTER 6 Looking Forward.....		118
6.1	Additional Potential Sensors.....	118
6.1.1	Temperature Sensor	118
6.1.2	Humidity Sensor	122
6.1.3	Micro-fluidic Analysis.....	123
6.2	Alternate Measurement Techniques	124
6.3	Summary	126
CHAPTER 7 Conclusion.....		128
7.1	Motivation of Work	128
7.2	Sensor Design Guidelines.....	130
7.3	Prototype Sensors.....	132
7.4	Alternatives	135
7.5	Final Thoughts	136
References.....		139
Vita		144

List of Tables

Table 4.1	Current sensor design parameters	76
Table 5.1	There is not a consensus on what values of concrete resistivity are associated with what level of corrosion risk	88
Table 5.2	Curve fitting results for estimating σ_m based on the measured pseudoQ	101
Table 5.3	Conductivity sensor position with respect to salt water pond	104

List of Figures

Figure 1.1 Concrete damage due to corrosion of the reinforcing steel.....	2
Figure 1.2 The hermetically sealed sensor is embedded in the concrete and wirelessly interrogated through a magnetically coupled reader coil	6
Figure 2.1 Commercial EAS Tag: This tag consists of several layers including a “pancake coil” inductor, a capacitor, and an adhesive layer.....	10
Figure 3.1 Schematic diagram of magnetically coupled circuit and corresponding impedance measurement	15
Figure 3.2 The resonant frequency of the sensor can be changed based on the state of a switch connecting a second capacitor.....	16
Figure 3.3 Prototype corrosion sensor consisting of inductor coil, two capacitors, and an exposed steel wire acting as a switch	17
Figure 3.4 Accelerated corrosion tests in concrete were conducted by creating salt water ponds on sections of the loaded concrete slabs	18
Figure 3.5 Corrosion sensor response in concrete showing, from left to right, an intact steel sensing wire, the transition region, and a broken sensing wire	19
Figure 3.6. Modified corrosion sensor circuit model using a resistor to depict the corroding steel wire.....	19
Figure 3.7 Changes in the magnitude (left) and phase (right) of the reader coil input impedance due to a change in sensor resistance are visible in both the magnitude and phase.....	21

Figure 3.8 The maximum change in the magnitude of the reader coil impedance is proportional to R_{tag}^{-1}	23
Figure 3.9 change in the calculated phase of the reader coil input impedance due to the tag is proportional to R_{tag}^{-1}	24
Figure 3.10 Observing the imaginary part of Z_{in} explains the behavior of the magnitude and phase observed above.....	26
Figure 3.11 Modified circuit diagram showing the parasitic resistance of the two inductor coils.....	27
Figure 3.12 The parasitic resistance of the tag coil limits the maximum magnitude deviation as the tag resistance goes to zero.....	28
Figure 3.13 The tag inductor coil resistance limits the maximum phase dip achieved at low transducer resistances	29
Figure 3.14 The parasitic resistance of the reader coil primarily affects lower frequencies where R is comparable to ωL_{reader}	30
Figure 3.15 Despite the clear change in the phase of the measured impedance, the change due to the tag resistance is largely unaffected by the reader coil resistance.....	31
Figure 3.16 Due to the finite tag coil resistance, the sensitivity of the circuit goes to zero when $R_{\text{transducer}} \ll R_{\text{tag coil}}$	34
Figure 3.17 The sensitivity of the phase to $R_{\text{transducer}}$ appears to approach a constant when $R_{\text{transducer}}$ becomes large.....	35
Figure 3.18 The coupling between the reader and tag coil is a function of the coil geometry as well as how they are aligned with one another.....	36
Figure 3.19 As two coils are moved apart, the coupling factor falls as one over the distance cubed.....	37
Figure 3.20 Both the magnitude and phase show a strong dependence on the coupling between the reader and tag.....	38

Figure 3.21 Simple RLC resonant circuit used for analyzing the quality factor	39
Figure 3.22 pseudoQ is calculated from the width of the resonance (FWHM) and the frequency at which the minimum phase occurs	41
Figure 3.23 Similar to the magnitude and phase deviations discussed above, pseudoQ is a function of R_{tag}^{-1} . The pseudoQ saturates at low sensor resistance when the phase of the impedance saturates at -90 degrees	42
Figure 3.24 For low coupling factors, pseudoQ is independent of coupling factor	43
Figure 3.25 When the coupling between the reader and tag becomes very high, the phase saturates at -90 degrees and $\Delta\omega$ becomes very wide, approaching infinity	44
Figure 3.26 Finite reader coil resistance has little effect on the calculated pseudoQ	45
Figure 3.27 Finite tag coil resistance lowers the maximum value of pseudoQ achieved as the transducer resistance becomes small	46
Figure 3.28 Extending the range of $R_{\text{transducer}}$ reveals that the relationship between pseudoQ and R changes around $R = \omega_0 L_{\text{tag}}$	47
Figure 3.29 The behavior of $\omega_{\theta\text{min}}$ helps explain the behavior of pseudoQ as $R_{\text{transducer}}$ becomes large	47
Figure 3.30 There is a region of relatively flat sensitivity when $R_{\text{transducer}}$ is greater than $R_{\text{tag coil}}$ and less than $\omega_0 L_{\text{tag}}$	49
Figure 3.31 Changing the tag inductance does not affect the behavior of the normalized circuit	50
Figure 4.1 The inductance of short solenoids can be computed based on the length, radius, and number of turns using Nagaoka's formula	55

Figure 4.2 The full circuit model also includes a parasitic capacitance from the reader coil connector	58
Figure 4.3 The critical frequency at which an optimum coil can be wound is a function of the loss in the capacitor	63
Figure 4.4 The baseline of the phase data is fit by windowing out the resonant tag behavior.....	65
Figure 4.5 Example curve fit using polynomial baseline and Lorentzian.	67
Figure 4.6 The curve fitting results agree quite well with the results calculated based on the known baseline reader coil impedance	68
Figure 4.7 Schematic diagram of the circuit modified to include a reference resonance which is present regardless of the state of the sensor	70
Figure 4.8 The high frequency (HF) resonance response is reduced by the presence of the low frequency (LF) resonance	70
Figure 4.9 In the non-ideal circuit, the presence of the reference circuit affects the pseudoQ of the sensor circuit, however, this effect is small.....	73
Figure 4.10 Second generation prototype corrosion sensor using concentric sense and reference inductor coils	74
Figure 4.11 The reader coil radius that produces the largest phase dip is dependent on the spacing between the reader and tag	77
Figure 4.12 Contour plot showing the phase data vs. time of a sensor embedded in concrete. The sensor wire breaks around day 285 causing the sense phase dip to disappear and the reference phase dip to become much stronger.....	79
Figure 4.13 A plot of pseudoQ vs. time for a sensor embedded in concrete shows a relatively quick transition from an intact to a broken sensing wire	79

Figure 4.14 Autopsies of the test slabs (left) revealed that there was a correlation between sensors with broken sensing wires and reinforcement corrosion (right)	80
Figure 4.15 A depiction of several unexpected behaviors encountered during field testing of the corrosion sensors	81
Figure 4.16 The steel sensing wire has been connected to the rebar to attempt to make it part of the larger electrochemical corrosion macrocell.....	84
Figure 4.17 A second external wire connected via an RF choke may provide a better DC connection to the rebar	84
Figure 5.1 There is a correlation between the corrosion rate as measured by the corrosion current and concrete resistivity	87
Figure 5.2 Modified circuit topology with the transducer in parallel with C_{sense} to allow the use of high-impedance transducers.....	89
Figure 5.3 The pseudoQ of the parallel circuit configuration is a strong function of $G_{\text{transducer}}^{-1}$	90
Figure 5.4 Arrangement of a simple two-wire conductivity probe.....	91
Figure 5.5 Prototype wireless conductivity sensor and matching wired reference probe.....	93
Figure 5.6 The phase of the impedance response of the conductivity sensor is clearly affected by the change in the conductivity of the salt water	95
Figure 5.7 As expected, the pseudoQ of the sense circuit is dependent on the conductivity of the salt water	95
Figure 5.8 Both the wired and wireless conductivity sensors agree quite well with the commercial conductivity meter.....	98
Figure 5.9 Curve fitting can be used to relate the measured pseudoQ of the conductivity sensor to the conductivity of the medium	101

Figure 5.10 The prediction bounds of the fit grow wider as pseudoQ approaches the intrinsic Q of the sensor	102
Figure 5.11 The pseudoQ of the conductivity sensors in the slab ponding area exhibit a periodic nature that coincides with the wet-dry cycle of the salt water pond.....	104
Figure 5.12 Test jig to allow substitution of the material between the reader and sensor without changing the reader and sensor alignment or spacing	106
Figure 5.13 The relative conductivity extracted from the slab sensors shows a clear dependence on the salt water ponding cycle	108
Figure 5.14 Conductivity (left) and corrosion sensor (right) in place in test slab before casting concrete	109
Figure 5.15 Final arrangement of reader coils and wireless probe after casting concrete	110
Figure 5.16 The pseudoQ of the conductivity sensor increased rapidly immediately after casting the concrete and then continued to increase at a slower rate throughout the measurement period	112
Figure 5.17 The conductance extracted from the wired and wireless probe agree quite well during the initial curing period	113
Figure 5.18 As the pseudoQ of the wireless sensor approaches the intrinsic pseudoQ, the error between the wired and wireless probes increases	114
Figure 5.19 Concrete resistivity as a function of curing time.....	115
 Figure 6.1 Both the pseudoQ and resonant frequency of the sensor are temperature dependent.....	 119
Figure 6.2 The resonant frequency of the corrosion reference circuit in the curing slab shows the same temperature dependence as the previous example	120

Figure 6.3 Demonstration of a capacitance-based wireless humidity sensor.	123
Figure 6.4 Example schematic of a Q-meter circuit which could be used to interrogate the sensor tags.....	125
Figure 7.1 Circuit diagram of resistance-based sensor circuit with reference resonance.....	131
Figure 7.2 Wireless sensors in place during typical construction process.....	137

CHAPTER 1

Introduction

1.1 STRUCTURAL HEALTH MONITORING

Today's world is increasingly going wireless. From cellular phones and wireless internet to computer mice and home theatre systems, these devices surround us, and more are appearing all the time. Given enough time and money, just about any system that uses some form of electronic communication can be made wireless. While some of these applications are more for convenience or show, there are other applications which can greatly benefit from the use of wireless technologies.

One area that may benefit from wireless technology is the growing interest in structural health monitoring. Our society depends heavily on a network of buildings, bridges, roadways, dams, and other such structures and unlike many of the disposable products of today's society, these structures are designed to last tens to hundreds of years. These structures must be periodically inspected throughout their lifetimes to ensure that they are able to safely perform their intended functions in light of degradation from normal use and aging. In addition, after catastrophic events, such as an earthquake or blast loading, it is desirable to be able to quickly and accurately assess the integrity of the structure [1]. Monitoring the structural health of the civil infrastructure presents unique challenges due to its typically large size, unique designs, continuous exposure to the environment, infrequent inspection, and long design life.

1.1.1 Reinforced Concrete Structures

The field of structural health monitoring encompasses a range of problems for many different structures. One particular area of interest is monitoring concrete structures for corrosion of the reinforcing and prestressing steel. Bridges and roadways subjected to deicing salts and/or marine environments are especially susceptible to corrosion. As of 2001, “approximately 15% of highway bridges were structurally deficient, primarily due to corrosion of steel and steel reinforcement” [2]. The direct costs of replacing and/or repairing these bridges is estimated at \$8.3 billion annually, while the indirect costs due to traffic delays and lost productivity are estimated at ten times that amount. Figure 1.1 illustrates an example of damage to concrete caused by corrosion of the reinforcing steel.



Figure 1.1 Concrete damage due to corrosion of the reinforcing steel [3].

Several methods currently exist for monitoring corrosion in reinforced concrete structures, each with their own benefits and limitations. One of the most basic methods is visual inspection. In this case, the exterior of the structure is

checked for visible signs of corrosion, including cracking, spalling, and rust staining [3]. Unfortunately, by the time visible signs of corrosion are present, the damage to the structure is usually extensive, requiring costly repairs or replacement. On the other hand, visual inspections are useful when used in conjunction with other methods of corrosion inspection.

Other inspection processes rely on acoustic techniques. These techniques involve some mechanism of inducing acoustic waves in the concrete, such as striking the concrete with a hammer or dragging a chain across the surface, and listening to the sound that is produced. A hollow sound can indicate the presence of cracks before they are visible [3]. Recent research in this area aims to improve upon the method by using a piezoelectric transducer to feed acoustic data to a computer where it can be analyzed in an attempt to determine differences in the response due to corroded and un-corroded rebar [4].

A commonly used electrical method for monitoring corrosion in steel reinforced concrete is the half-cell potential method. Concrete and corroding rebar together form an electrochemical half-cell. The potential of this half-cell is measured against a reference half-cell which is placed in contact with the surface of the concrete. This data is then correlated to a probability of corrosion. Unfortunately, factors such as differing oxygen concentrations, carbonation, concrete patch repair, surface conduction effects, or the presence of corrosion inhibitors can all shift the half-cell potentials, making the data difficult to interpret [5]. Another electrical technique is the use of linear polarization resistance, which provides an indication of the corrosion current in the rebar. Both the half-cell potential and linear polarization resistance measurements require direct electrical connection to the reinforcing steel. Access to the reinforcement must either be provided at the time of construction or concrete must be removed at a later date in order to make the measurements, which can be costly and time consuming. Also,

these methods cannot be used with epoxy-coated or galvanized steel reinforcement [5, 6].

Each of the aforementioned inspection techniques involves looking from the outside of the concrete in an attempt to discern what is happening on the inside. By placing sensors inside of the concrete, it may be possible to gain more accurate and therefore more useful information on the actual state of the reinforcing steel.

1.2 EMBEDDED SENSORS

Embedding a sensor inside a structure allows access to areas that are not readily accessible using other non-invasive inspection methods. Although embedded sensors have some advantages over external sensors, it is important to realize that placing sensors in inaccessible locations can also create complications. For example, an external sensor allows immediate access to the sensor itself for data collection. With an embedded sensor, extra thought must be put into how the data will be retrieved. Two obvious possibilities for retrieving information from embedded sensors are through either wired or wireless networks. For short range communications, wired networks often provide greater bandwidth at a lower cost. However, although the sensor itself may be cheaper using a wired communication link, it is important to realize that there will be an additional cost incurred at the time of installation to run wiring and connect the sensors together. Anything penetrating the surface of the concrete, including wires, also provides a potential ingress path for harmful contaminants, such as moisture and chloride ions.

Another important consideration when designing an embedded sensor is how to power the device. For wired sensor networks, powering the devices is simply a matter of a few additional wires, or even combining power and data lines into a single two-wire system. Typically, wireless devices rely on battery power. Depending on the needs of the device, batteries can be relatively inexpensive or rather costly. Also, batteries have a finite lifetime after which they need to be

replaced or recharged. If replacing or recharging is not an option, the sensor is effectively lost once the battery dies. An alternative to using batteries to power wireless devices is to use “unpowered” or passive sensors. It is possible to transmit power without wires using either far-field electromagnetic fields, such as in microwave power schemes, or near-field electric and/or magnetic fields, such as in a transformer. Strictly speaking, the devices are powered by energy from the electric or magnetic field; however, the terms “passive” and “unpowered” are used to convey the fact that the devices have no onboard power supply of their own.

Passive wireless sensors would be ideal for many structural health monitoring applications. Wireless communication would most likely make installation easier and cheaper, while the unpowered nature of the sensor would allow the sensors to be embedded inside walls, cast into concrete, and placed in other areas where maintenance and battery replacement is either cost prohibitive or impossible. Barring unexpected failure of the sensors themselves, such passive devices should be able to last the lifetime of the structures they are designed to monitor.

1.3 SCOPE OF WORK

This dissertation expands on the previous work of several researchers at The University of Texas at Austin [7-11]. The development and analysis of a passive wireless Electronic Structural Surveillance (ESS) sensor platform for structural health monitoring, with specific emphasis on corrosion in steel reinforced concrete, is discussed. The general concept of the sensor system is to have a small, self-contained sensor which would be embedded in the concrete of the structure the sensor is monitoring. The sensor is hermetically sealed, allowing the sensor to remain functional despite exposure to potentially harsh and corrosive environments. Inside the sensor housing is an inductive coil of wire which is magnetically coupled to a second “reader” coil outside of the concrete. This reader coil is used to both

power and interrogate the sensor and could be housed in a hand-held unit or mounted on the underside of a vehicle for the easy and rapid assessment of many sensors. Figure 1.2 provides an illustration of this concept.

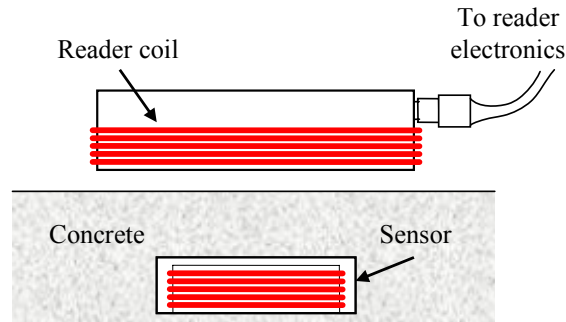


Figure 1.2 The hermetically sealed sensor is embedded in the concrete and wirelessly interrogated through a magnetically coupled reader coil.

Existing commercial wireless sensors as well as sensors under development are discussed in Chapter 2. The properties of these systems helped influence the design of the current sensor design. Chapter 3 presents the analysis of the proposed sensor system through the use of an idealized circuit model. Based on the results of the analysis, several suggestions are given for guiding the development of actual sensors. Chapters 4 and 5 discuss the development of prototype corrosion and conductivity sensors. The sensors are tested in a controlled laboratory environment as well as in concrete slabs. Chapter 6 discusses the adaptation of the sensor platform to other applications including temperature and relative humidity sensors as well as suggestions for future investigations. Chapter 7 presents a summary of the work.

CHAPTER 2

Design Considerations

2.1 DESIGN GUIDELINES

Throughout the course of the research done at The University of Texas at Austin, an emphasis has been placed on developing practical devices which could be put into actual use. Early in the design process, a set of design guidelines was developed for the prototype sensors. Not only did these attributes affect the conceptual design of the sensors, they also placed limits on the type of technology which could be used and by extension, the type and amount of information the sensors could provide. The design guidelines of the sensor are related to the cost, durability, power and mode of communication, and the reliability of the sensor readings.

2.1.1 Cost

Cost limitations are one of the most important aspects related to the design of the sensors. The cost of implementing structural health monitoring solutions must be in line with the derived benefits of such a system. In regards to reinforced concrete, corrosion can be widely distributed within a structure, making a dense sensor network preferable. With the possibility of installing hundreds to thousands of sensors in a single structure, the sensors must have a low initial unit cost as well as low lifetime costs. Implementing a low-cost sensor design also opens up other potential applications where the cost of individual sensors must be low. It is important to realize that cost limitations can substantially affect all other areas of the sensor design.

2.1.2 Durability

The final sensor design must be durable. Within the context of structural health monitoring, the sensors must be able to survive the rigors of traditional construction methods as well as function throughout the design life of the structure. The sensors may be subjected to large temperature variations, rough handling, vibration during concrete placement, and potential exposure to harsh environments. This may affect the type of components that are used in the sensor and strongly influences the packaging requirements. The sensor should also not reduce the durability of the structure in which it is placed.

2.1.3 Power and Communication

The ability to power and communicate with any sensor is an important part of the design consideration and can have a significant impact on the overall design. As mentioned previously, the decision was made to rely on wireless communication, making the sensors easy to place, and not to include a battery within the sensor, so that the life of the sensor would not be limited by the life of the battery.

2.1.4 Reliability

Clearly any sensor developed ultimately must produce repeatable, reliable results if it is to be useful in the field. This requires testing of the sensors in a variety of installations and environmental conditions. However, testing of sensors designed to be embedded in concrete is complicated by the fact that once concrete has cured, it is difficult to go back and determine what went on inside the concrete. Also, many of the changes in concrete occur over very large time spans and accelerated testing procedures must be developed in order to obtain results in a workable timeframe. Finally, although standard testing procedures have been developed for some concrete failure mechanisms, many of the underlying causes of

failure are at best only partially understood. Consequently, which variables are appropriate for observation and what values these variables should take is not always clear.

2.2 CURRENT PASSIVE WIRELESS SENSORS

There are many existing examples of unpowered wireless sensors. Some, like Electronic Article Surveillance (EAS) and Radio Frequency Identification (RFID) tags, have been successfully developed into commercial products. Both of these technologies were reviewed and evaluated as a starting point for future work.

2.2.1 EAS Tags

EAS tags are perhaps the most common form of unpowered wireless sensors today. This technology began to appear commercially in the late 1960s from companies such as Checkpoint, Knogo, and Sensormatic [12]. According to the Association for Automatic Identification and Mobility, there are now over 800,000 EAS systems installed worldwide [13]. The tags are designed to help curtail shoplifting in retail environments. There are many different types of EAS systems and almost all of them are low cost and easy to use. One very common design of interest is the radio frequency (RF) tag, shown in Figure 2.1.

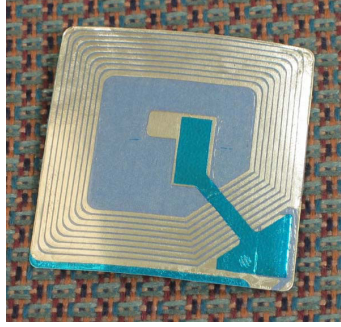


Figure 2.1 Commercial EAS Tag: This tag consists of several layers including a “pancake coil” inductor, a capacitor, and an adhesive layer.

These tags consist of a simple inductor-capacitor (LC) circuit which is characterized by a specific resonant frequency f_0 . The resonant frequency is determined by the values of the inductor and capacitor through the following relationship:

$$f_0 = \frac{1}{2\pi\sqrt{L \cdot C}}. \quad (2.1)$$

The tags can be deactivated at checkout time by disabling the capacitor in the circuit. Pedestals at the store exits monitor for intact tags by sweeping through specific frequency bands and monitoring for resonances. In this way, EAS tags function as a simple one-bit sensor. Most EAS tags are designed so they can be manufactured in bulk and are therefore extremely inexpensive. A quick search reveals typical RF sticker tags like those discussed above can be purchased for less than \$0.04 U.S. Dollars (USD) each, with possibly even lower prices in bulk [14]. The low cost and ease-of-use of these EAS tags makes them a good starting point for other passive wireless sensor designs.

Similar technology employing passive resonant circuits has also been proposed for use in marking underground objects such as water mains or buried

cables, dating as far back as the 1970s [15]. 3M currently produces and markets a line of such devices. Different frequencies are used to mark different types of utilities and are located from the surface using a hand-held instrument similar in size to a metal detector.

2.2.2 RFID Tags

Another commercially available wireless tagging technology is RFID. RFID tags come in both powered and unpowered versions. One of the main differences between RFID tags and EAS tags is that RFID tags contain a low power integrated circuit that allows the tag to transmit information, such as an ID number, back to the reader. Similar to EAS tags, passive RFID tags use a tuned antenna circuit to pick up energy from the electromagnetic field generated by the reader. RFID technology is now commonly found in security badges for access control, they are used in automated high-speed toll collection, and can even be made small enough to implant under the skin of animals and humans for identification purposes.

Although the most common write-once/read-many implementations of RFID tags might not be considered true sensors, there are a few designs that can transmit more than just a simple serial number back to the reader. One such design, the MCRF202 from Microchip Technology, allows the connection of a switch to a modified RFID tag [16]. If the switch is closed, the tag transmits information normally; however, if the switch is open, the tag inverts the bit stream it sends back to the reader. This allows the MCRF202 to be connected to a sensor which provides one bit of information. Another design named EmbedSense™ from MicroStrain goes a step further by including an analog-to-digital converter with a special RFID chip in one housing [17]. Rather than send back an ID number from static memory, the devices are able to transmit information back from sensors such as strain gauges and temperature sensors.

RFID tags have the benefit of transmitting more information than a simple EAS tag; however, there are costs associated with this increase in functionality. At the time this research was started, the monetary cost of RFID tags was several orders of magnitude higher than EAS tags. Therefore, more attention was given throughout this research to EAS style passive wireless devices. Although the price of RFID tags has dropped in the recent past – write-once/read-many tags can now be bought for approximately \$0.55 USD; the price still remains higher than simple EAS style technology. Should such simple RFID tags ever reach the \$0.10 USD price point that many manufacturers claim they are working towards, it may be possible to include such a tag in any wireless sensor platform which is developed simply for the purposes of providing a unique identifier. However, if the RFID platform is to be used in the actual sensing mechanism, the price continues to remain too high. Individual EmbedSense sensor nodes are priced at approximately \$300 USD each, which would most likely be cost prohibitive in applications requiring hundreds or thousands of sensors.

Another cost associated with RFID tags is their read range, which can be as low as a few centimeters for the most basic passive tags to as high as several hundred feet for high frequency active tags. The distance at which a tag can be read varies greatly depending on the size of the tag, the frequency of operation, the power of the reader, and whether the tag is active or passive. For example, the passive EmbedSense sensor tag discussed above claims a read range of approximately 2 cm, which is insufficient for many of the proposed applications in structural health monitoring. Active RFID tags can also be used to increase the working distance. Active RFID tags carry an onboard power supply in the form of a battery, which is used to boost the power of the signal transmitted back to the reader. These tags have the advantage of being able to carry more sophisticated electronics, faster data transfer rates, and greater read ranges. However, since the

batteries have finite lifetimes, they are not well suited to long-term embedded applications such as structural health monitoring.

2.3 SENSORS IN CONCRETE

During the course of this project, several other institutions have begun research aimed at developing sensors for monitoring corrosion in steel reinforced concrete. At least one sensor package has become available commercially during this time as well. A sample of these sensors are discussed briefly as a point of comparison.

2.3.1 Smart Pebble™

The Smart Pebble is one such device being developed by SRI International and the California Department of Transportation to monitor chloride ion concentrations in concrete [18]. As mentioned earlier, the presence of chloride ions in concrete can be a major contributing factor to the corrosion of the reinforcing steel. The sensor contains two electrochemical electrodes and is connected to the external “switch” input of the MCRF202 RFID tag mentioned in Section 2.2.2. A low-power comparator circuit compares the voltage of a silver/silver-chloride half-cell, which is sensitive to chloride ion concentration, to a copper/copper-sulfate reference half-cell. This comparator is calibrated to trigger the MCRF202 to invert the bit stream it sends back to the reader if the chloride ion concentration rises above a pre-set threshold. Unfortunately, this multi-step calibration procedure must be conducted on a per-unit basis and is a time-consuming process, requiring several weeks for the chloride concentration inside the electrochemical cell to stabilize before the calibration can be completed. The voltage the sensor produces is also temperature dependent, although steps are being taken to compensate for this in the on-board circuitry. Finally, the electrochemical cell is subject to temporal drift as well as to drying out, problems which must be solved before such a sensor could be

used in real-world long-term monitoring applications. The researchers expect the sensors to “cost less than \$100 each” [19].

2.3.2 Smart Aggregate

Researchers at the Johns Hopkins University Applied Research Laboratory are also working to develop a wireless embeddable sensor platform for use in steel reinforced concrete [20]. Their smart aggregate sensor is designed around a low-power microcontroller and other associated circuitry. The proposed sensor included integrated temperature and resistivity sensors. The device is powered via inductive coupling and transmits data back using the RS-232 protocol over a separate RF link. At the time of their last writing in 2003, the researchers were embedding several of the sensors in a bridge deck for testing, but no further information has been found.

2.3.3 ECI-1

The ECI-1 Embedded Corrosion Instrument from Virginia Technologies is one of the few concrete monitoring sensor packages that is available commercially. The ECI-1 combines several electrodes and an onboard microcontroller into one package for making multiple measurements related to corrosion including linear polarization resistance, open circuit potential, chloride ion sensitivity, resistivity, and temperature. Compared to many of the other devices mentioned previously, the ECI-1 is somewhat larger at 83 x 122 x 94 mm and the manufacturers suggest that project designers consider how the device may affect the structure it is embedded in. The device is powered and communicates through a wired sensor network. While this allows the use of sophisticated onboard electronics and sensors, it also increases the installation cost of the device and provides a potential ingress path into the concrete for harmful substances such as chloride ions. The cost of the unit itself is also somewhat high at approximately \$2000 USD per unit, which would restrict their use to applications which require only a limited number of sensing points.

CHAPTER 3

Sensor Basics

3.1 SENSOR PLATFORM

In an effort to produce a truly low-cost sensor, the use of simple magnetically coupled resonant circuits, similar in concept to EAS tags, were chosen to form the basis of the passive wireless sensor platform. The system consists of an inductive reader coil which is magnetically coupled to a second coil in a resonant tag circuit. Figure 3.1 is a schematic diagram of such a circuit, where M represents the mutual inductance between the reader and tag coils. The tag is interrogated by measuring the complex input impedance Z_{in} of the reader coil. Changes in the tag portion of the circuit, for example through the inclusion of a resistance or capacitance-based transducer, will cause a corresponding change in the measured impedance. Throughout this document the term “tag” is used to refer to the behavior of the circuit itself based solely on its component values. The tag can be made into a sensor, which is influenced by the outside world, by including some type of transducer.

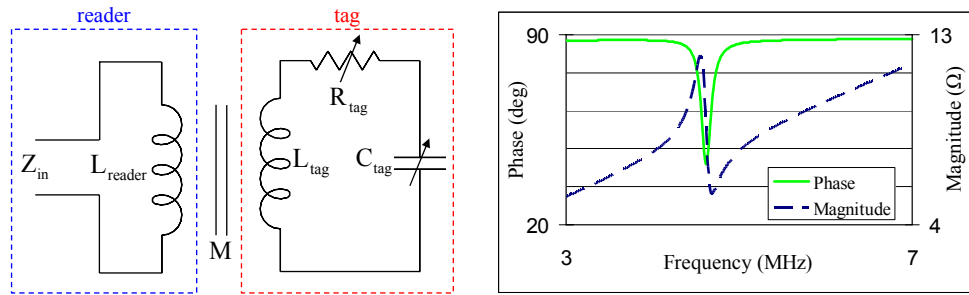


Figure 3.1 Schematic diagram of magnetically coupled circuit and corresponding impedance measurement.

3.1.1 Capacitance Based Sensor

A simple threshold sensing circuit can be developed using the circuit described above. As mentioned previously in Chapter 2, the resonant frequency of a simple LC circuit is given by

$$f_0 = \frac{1}{2\pi\sqrt{L \cdot C}} \quad (3.1)$$

A simple sensor which uses a change in capacitance to cause a shift in the resonant frequency can be realized by connecting a second capacitor to the circuit via a switch which changes state based on the variable which is to be monitored. Figure 3.2 provides a schematic illustration of this concept. Opening the switch changes the capacitance of the circuit from the parallel combination (C_1+C_2) to the single capacitance C_1 . As can be seen in Figure 3.2, the resulting shift in resonant frequency is readily observable in the phase of the measured reader coil impedance.

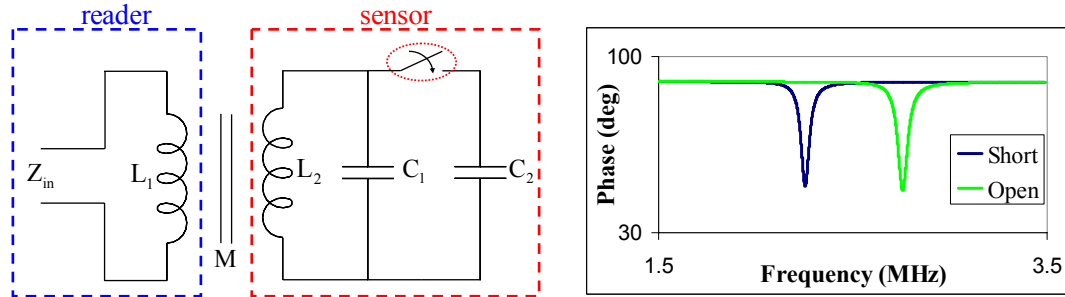


Figure 3.2 The resonant frequency of the sensor can be changed based on the state of a switch connecting a second capacitor.

A prototype wireless corrosion sensor was developed based on this design and was tested in the laboratory as well as in concrete slabs. The sensor consisted

of a sealed housing containing an inductor and two capacitors. A length of bare steel wire that extended outside of the sealed sensor housing served as the switch connecting the second capacitor to the circuit, as shown in Figure 3.3.

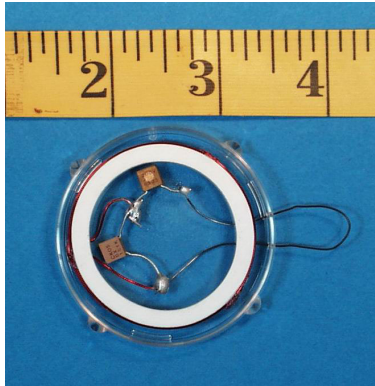


Figure 3.3 Prototype corrosion sensor consisting of inductor coil, two capacitors, and an exposed steel wire acting as a switch [3].

With the sensor embedded in concrete, the steel sensing wire is exposed to the same environment as the steel reinforcement and thus is subject to corrosion. Once the wire corrodes all the way through, the second capacitor is removed from the circuit shifting the resonant frequency. By changing the gauge of the steel sensing wire, the amount of corrosion necessary to break the wire could be varied, allowing adjustment of the corrosion threshold of the sensor.

The sensors were subjected to accelerated corrosion by immersing them in salt water solutions. Periodically, the sensors were removed from the salt water and measured. It was shown that once the corroding wire broke, the resonant frequency of the sensor shifted as expected and experiments were done in an attempt to correlate the time-to-failure with the gauge of the steel sensing wire as well as the amount of corrosion that had occurred on test specimens of rebar which were

subjected to the same corroding environment as the sensing wires [3]. The sensors performed well in these tests and were next subjected to tests in actual concrete.

The tests were conducted by casting several sets of sensors into concrete slabs. The concrete used in these tests was designed to be highly permeable by using large quantities of an air-entraining admixture. It was felt that this would allow faster penetration of corrosion-causing agents, such as chloride ions. The cured beams were then loaded on the ends to facilitate crack formation, and the complete setup was then subjected to accelerated corrosion by means of salt water ponds on top of the concrete slabs, as shown in Figure 3.4 [9, 21].



Figure 3.4 Accelerated corrosion tests in concrete were conducted by creating salt water ponds on sections of the loaded concrete slabs [21].

Although the response from the sensors changed over time, their response did not match the previous results obtained from the lab tests in salt water. Unlike the initial tests where the corroding wire essentially behaved as a simple switch, the sensors in the concrete slabs did not show a distinct, immediate change from the intact-wire to the broken-wire resonant frequency. Instead, there was a “transition region,” shown in Figure 3.5 (center), in which no clear resonance was visible.

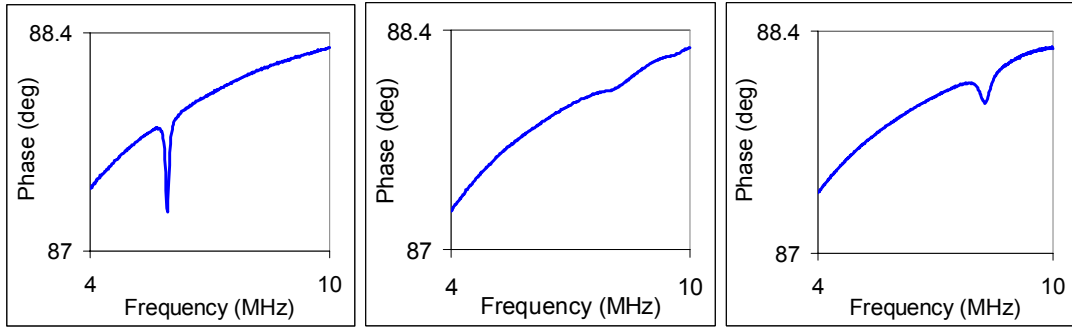


Figure 3.5 Corrosion sensor response in concrete showing, from left to right, an intact steel sensing wire, the transition region, and a broken sensing wire[21].

Further testing and modeling suggested that, rather than behaving as a simple switch, the corroding steel wire embedded in the concrete was acting more like a variable resistor. As the wire transitioned from low to high resistance, there was a period where the resonance was almost completely damped and the sensor could not be reliably read. While the sensor was designed as a threshold sensor – either the wire is intact or broken – it was concluded that the circuit is more accurately represented as shown in Figure 3.6. The switch in Figure 3.2 has been replaced with a resistor to represent the physical behavior of the steel sensing wire.

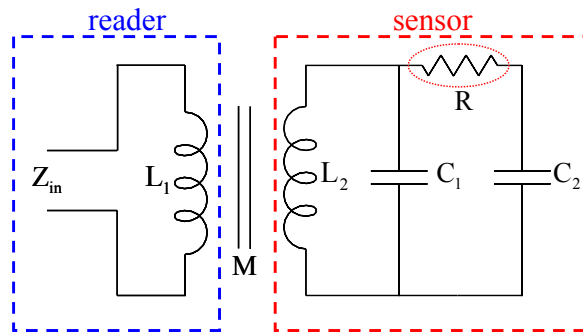


Figure 3.6. Modified corrosion sensor circuit model using a resistor to depict the corroding steel wire.

3.1.2 Resistance Based Sensor

In response to the behavior encountered during the testing of the corrosion sensor in concrete, efforts were made to develop a method to detect changes in the resistance of the original resonant tag circuit depicted in Figure 3.1. While a change in the capacitance of the circuit causes a relatively simple-to-detect change in the resonant frequency, the change in the impedance of the reader coil due to a change in the resistance of the tag is more complicated.

The circuit model in Figure 3.1 was used to analyze the affects of varying circuit parameters on the measured reader coil impedance. The input impedance of the reader coil can be expressed in terms of the circuit parameters as follows

$$Z_{in} = j\omega L_{reader} + \frac{\omega^2 M^2}{j\omega L_{tag} + R_{tag} - \frac{j}{\omega C_{tag}}} . \quad (3.2)$$

Figure 3.7 shows the magnitude and phase for two simulated tag resistances where $R_1 < R_2$ and the frequency has been normalized to the resonant frequency of the tag given by (3.1).

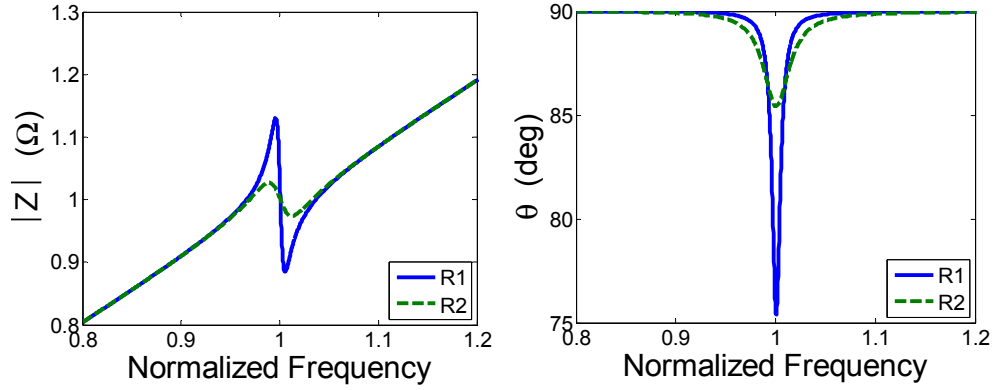


Figure 3.7 Changes in the magnitude (left) and phase (right) of the reader coil input impedance due to a change in sensor resistance are visible in both the magnitude and phase.

The coupling between the reader and the tag can be expressed in terms of the mutual inductance M or the coupling factor k . The mutual inductance is related to the flux linkage between the two coils and is a function of the geometry of the coils themselves as well as the spatial orientation of the coils with respect to one another. The mutual inductance can be expressed as

$$M = \frac{1}{I_{reader} I_{tag}} \iiint (\mu \vec{H}_{reader} \cdot \vec{H}_{tag}) dv, \quad (3.3)$$

where M is the mutual inductance between two coils, \vec{H}_{reader} is the field produced by the current I_{reader} and \vec{H}_{tag} is the field produced by I_{tag} . M is expressed in the units of inductance, henrys. Often, the coupling factor k is used instead of M as it gives a more intuitive idea of how two inductors are coupled without needing to know the self-inductance of either coil. The coupling factor k is related to the mutual inductance and the self-inductance of each inductor as

$$k = \frac{M}{\sqrt{L_{reader} \cdot L_{tag}}}, \quad (3.4)$$

and ranges from zero (no coupling) to one (perfect coupling). Transformers are often idealized as having perfect coupling. To achieve this type of coupling, however, the coils are usually wound either directly on top of each other or in close proximity, often on some type of core. Even in the best of circumstances, achieving this level of coupling is impractical when dealing with a remote embedded sensor.

For the following simulations, k has been set to 0.05. To give a sense of scale, this corresponds to a separation of roughly 3 cm between a single-turn reader coil and five-turn tag coil used in early experiments [22]. The effects of varying k on circuit behavior are discussed later in Section 3.1.2.3.

There are several obvious changes in both the magnitude and phase of the measured input impedance due to changes in the resistance of the sensor. Off-resonance, the circuit seems to appear as a simple inductor where $Z_{in} = j\omega L_{reader}$, such that the magnitude is linearly increasing with frequency and the phase is constant at 90 degrees. As ω approaches the resonant frequency of the tag, both the magnitude and phase of the reader coil input impedance deviate from this straight line behavior. In order to observe how these deviations behave as a function of sensor resistance, the circuit was simulated with varying tag resistance.

In an attempt to examine the behavior of the circuit without regard for specific circuit values, the input impedance expressed in (3.2) can be normalized to the impedance of the reader coil on resonance, $\omega_0 L_{reader}$. At the same time, (3.4) is used to substitute the coupling factor k in place of the mutual inductance M . The resulting normalized impedance is expressed as

$$\frac{Z_{in}}{\omega_0 L_{reader}} = j \left(\frac{\omega}{\omega_0} \right) + \left(\frac{\omega}{\omega_0} \right)^2 \frac{k^2}{j \frac{\omega}{\omega_0} + \frac{R_{tag}}{\omega_0 L_{tag}} - j \frac{\omega_0}{\omega}}, \quad (3.5)$$

where the normalized units of frequency are ω/ω_0 and the tag resistance is normalized to $\omega_0 L_{tag}$. The normalized units are used throughout the following analysis.

The maximum deviation between the magnitude of the normalized impedance with and without a resonant sensor present ($\Delta|Z|$) as a function of tag resistance R_{tag} is plotted in Figure 3.8. This deviation is proportional to R_{tag}^{-1} , which becomes clear when the data are plotted in log-log format. As the sensor resistance becomes large, the resonance is damped and the deviation due to the sensor tends towards zero. At the other extreme, as the sensor resistance approaches zero, the sensor becomes a perfect resonant LC circuit and the magnitude of the impedance approaches infinity.

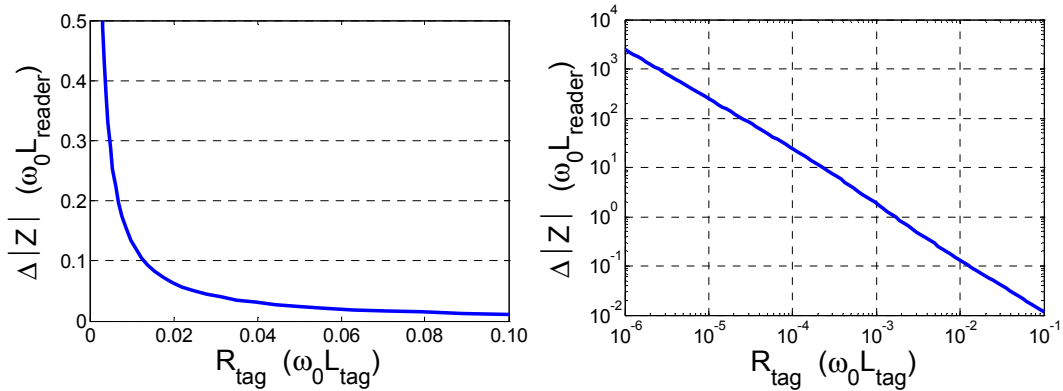


Figure 3.8 The maximum change in the magnitude of the reader coil impedance is proportional to R_{tag}^{-1} .

The maximum deviation in the phase of the impedance ($\Delta\theta$) due to the presence of the resonant tag exhibits a similar R_{tag}^{-1} behavior to the magnitude and tends towards zero for large R_{tag} . However, as can be seen in Figure 3.9, as R_{tag} becomes very small, between 10^{-3} and $10^{-4} \omega_0 L_{\text{tag}}$, the phase dip begins to level off and asymptotically approach 180 degrees. This is due to the fact that even with zero tag resistance, the phase of the impedance has a lower bound at -90 degrees.

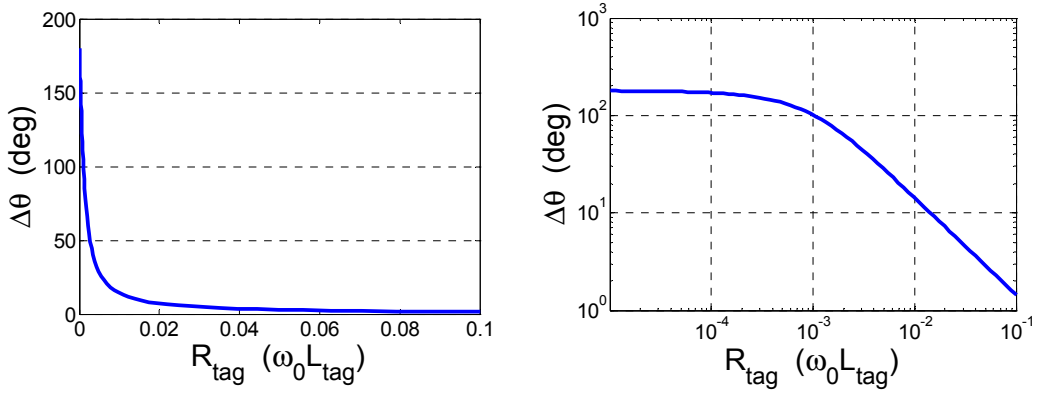


Figure 3.9 change in the calculated phase of the reader coil input impedance due to the tag is proportional to R_{tag}^{-1} .

All of this behavior can be explained by examining the expression for the reader coil input impedance given in Equation (3.2). As the resistance approaches infinity, the term contributed by the tag portion of the circuit goes towards zero, leaving only the impedance due to the reader coil. At this point, the deviation from the impedance with no tag present is zero:

$$\lim_{R_{\text{tag}} \rightarrow \infty} \left[j\omega L_{\text{reader}} + \frac{\omega^2 M^2}{j\omega L_{\text{tag}} + R_{\text{tag}} - j/\omega C_{\text{tag}}} \right] = j\omega L_{\text{reader}} + \frac{\omega^2 M^2}{\infty} = j\omega L_{\text{reader}}. \quad (3.6)$$

When the tag resistance goes to zero, care must be taken when examining the behavior of the circuit as the frequency approaches the resonant frequency ω_0 . Solving (3.1) for C, substituting into (3.2), setting R_{tag} to zero, and rearranging terms leads to

$$Z_{in} = j\omega \left\{ L_{reader} - \frac{M^2}{L_{tag} \left[1 - \left(\frac{\omega_0}{\omega} \right)^2 \right]} \right\}. \quad (3.7)$$

Examining the limit as ω approaches ω_0 from the left and the right gives

$$\begin{aligned} \lim_{\omega \rightarrow \omega_0^-} Z_{in} &= j\omega_0 [L_{reader} - (-\infty)] = j\infty \\ \lim_{\omega \rightarrow \omega_0^+} Z_{in} &= j\omega_0 [L_{reader} - (\infty)] = (-j\infty). \end{aligned} \quad (3.8)$$

If the imaginary part of Z_{in} is plotted as a function of frequency, as shown in Figure 3.10, this behavior can be illustrated graphically. Since the limit is different when approaching ω_0 from different directions, the limit is undefined at exactly ω_0 . As ω approaches ω_0 from both directions, the magnitude of the impedance approaches +infinity. Before ω reaches ω_0 , the imaginary part of Z_{in} is positive and the real part is zero, giving a phase angle of +90 degrees. However, when $\omega_0 < \omega < \omega_0 / \sqrt{1-k^2}$, the imaginary part of Z_{in} is negative, giving a phase angle of -90 degrees, which leads to a maximum deviation in the phase due to the sensor of 180 degrees. This analysis explains the behavior observed in the above simulations.

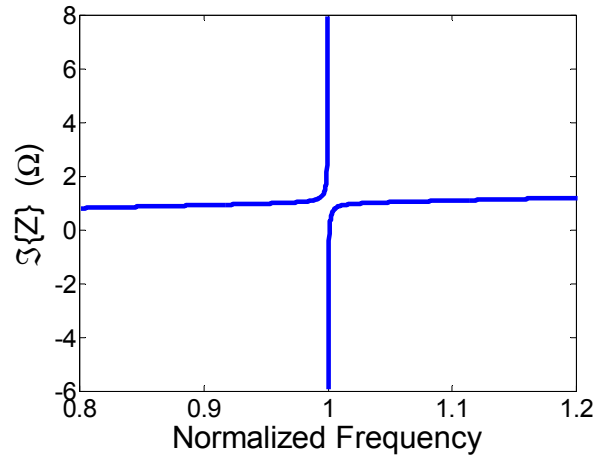


Figure 3.10 Observing the imaginary part of Z_{in} explains the behavior of the magnitude and phase observed above.

The above data suggest that either the magnitude or phase deviation could be measured at very high resistances. The magnitude may appear to be a more useful measurand than the phase since it does not saturate at very low resistances. However, it seems intuitive that arbitrarily large or small tag resistances would be impractical in real-world applications. For example, as R_{tag} becomes large, $\Delta|Z|$ and $\Delta\theta$ both go towards zero. In any real-world system used to measure the reader coil input impedance, there will be some finite minimum detectable change in $|Z|$ and θ . These limits will be determined by the resolution of the instrument as well as the overall signal to noise ratio. The minimum detectable $\Delta|Z|$ and $\Delta\theta$ will therefore set some maximum R_{tag} above which no signal can be detected.

3.1.2.1 Parasitic Losses

Another practical limit on the circuit performance comes from the finite parasitic resistance any real-world inductor coil possesses. Figure 3.11 shows a modified circuit diagram which includes the resistance of both the reader and sensor coils, which will have an effect on the behavior of the sensor system.

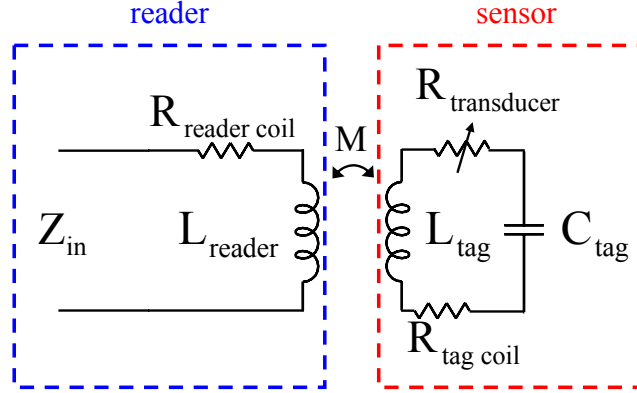


Figure 3.11 Modified circuit diagram showing the parasitic resistance of the two inductor coils.

The effect of these two parasitic resistances will be considered separately beginning with the tag coil resistance.

The inclusion of the tag coil resistance in the reader coil input impedance is fairly straight forward and is in fact equal to (3.2), with $R_{\text{tag}} = R_{\text{transducer}} + R_{\text{tag coil}}$:

$$Z_{in} = j\omega L_{\text{reader}} + \frac{\omega^2 M^2}{j\omega L_{\text{tag}} + (R_{\text{transducer}} + R_{\text{tag coil}}) - j/\omega C_{\text{tag}}} . \quad (3.9)$$

In this way it serves to create a lower limit on the total tag resistance. In the original circuit with no parasitic resistance, as R_{tag} approaches zero $\Delta|Z|$ increases unbounded. The inclusion of $R_{\text{tag coil}}$ sets an upper bound on $\Delta|Z|$ as can be seen in Figure 3.12. The deviation in magnitude is plotted for the original ideal inductor coil as well as two other values of $R_{\text{tag coil}}$.

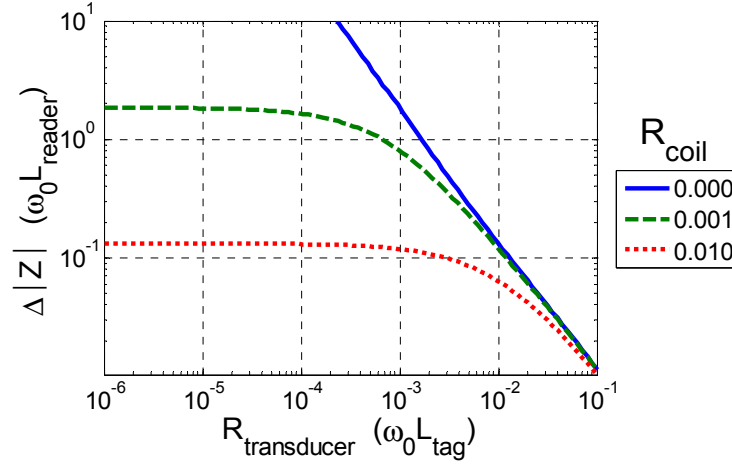


Figure 3.12 The parasitic resistance of the tag coil limits the maximum magnitude deviation as the tag resistance goes to zero.

In the ideal circuit with no parasitic resistance, the maximum phase dip at zero resistance was limited to 180 degrees. As can be seen in Figure 3.13, the addition of the sensor coil resistance lowers the maximum possible phase dip to a value less than 180 degrees.

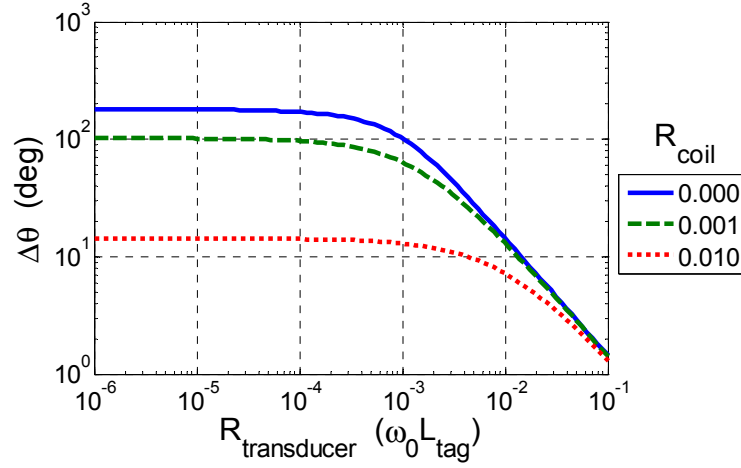


Figure 3.13 The tag inductor coil resistance limits the maximum phase dip achieved at low transducer resistances.

The effects of the parasitic resistance of the reader coil are also fairly easy to calculate. In this case, $R_{\text{reader coil}}$ appears as an additional term along with the reader coil inductance:

$$Z_{in} = (R_{\text{readercoil}} + j\omega L_{\text{reader}}) + \frac{\omega^2 M^2}{j\omega L_{\text{tag}} + R_{\text{tag}} - j/\omega C_{\text{tag}}}, \quad (3.10)$$

which changes the input impedance measured when no tag/sensor is present from that of an ideal inductor to

$$Z_{in} = R_{\text{readercoil}} + j\omega L_{\text{reader}}. \quad (3.11)$$

The affect of the reader coil resistance is most apparent in the phase of the measured input impedance, though the magnitude is affected as well. The measured

phase vs. frequency for three different reader coil resistances are shown in Figure 3.14. The presence of the parasitic resistance causes the phase angle of the impedance to deviate from that of an ideal inductor. While the impedance of an ideal inductor has a phase angle of +90 degrees over all frequencies, the inclusion of the coil resistance, and thus the inclusion of a real component to the impedance, alters the phase angle. This effect is most prominent at lower frequencies where $R_{\text{reader coil}}$ is comparable to ωL_{reader} .

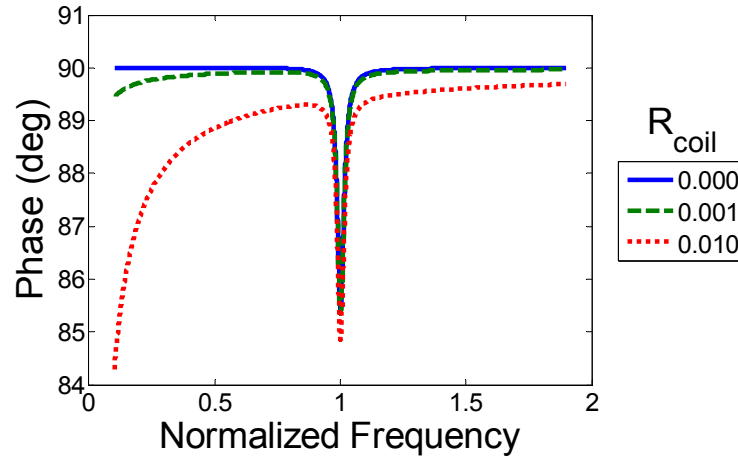


Figure 3.14 The parasitic resistance of the reader coil primarily affects lower frequencies where R is comparable to ωL_{reader} .

Despite the clear change in the actual phase of the measured impedance due to the reader coil resistance, the depth of the phase dip, as calculated by the difference between the phase of the reader coil with and without a tag present, remains largely unchanged, as shown in Figure 3.15. The deviation in the magnitude of the impedance is similarly unaffected by the reader coil resistance.

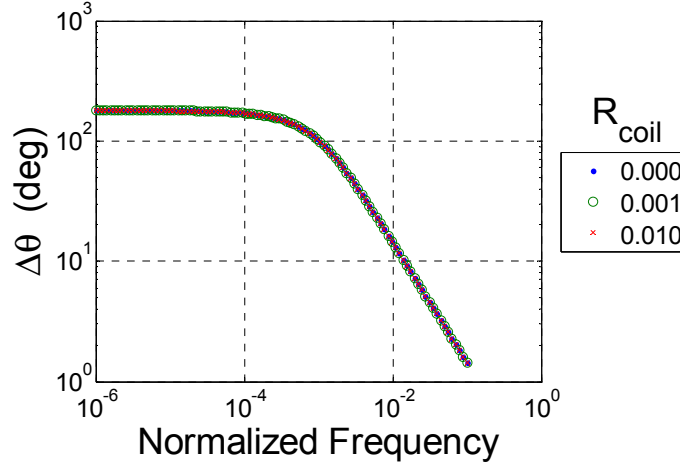


Figure 3.15 Despite the clear change in the phase of the measured impedance, the change due to the tag resistance is largely unaffected by the reader coil resistance.

3.1.2.2 Sensitivity

When considering the application of the circuit shown in Figure 3.1 as a means of sensing changes in the environment through some transducer, it is important not only to consider what parameters of the measured input impedance change as a function of the environmental stimulus, but also *how* these parameters change as a function of the stimulus. The percent change of a measured output O of the circuit to a change in an environmental stimulus S can be expressed as

$$\frac{1}{O} \frac{\partial O}{\partial S}. \quad (3.12)$$

This can be further broken down by considering that the change in the output of the circuit is caused by a change in the impedance of a generic transducer, which is in turn caused by a change in the stimulus. Using the chain rule, (3.12) becomes

$$\frac{1}{O} \underbrace{\frac{\partial O}{\partial Z_{transducer}}}_{\text{circuit response}} \underbrace{\frac{\partial Z_{transducer}}{\partial S}}_{\text{transducer response}}. \quad (3.13)$$

Further analysis requires some knowledge of how the transducer behaves as a function of the stimulus.

Using a familiar example, the resistance of a metal as a function of temperature is often approximated by a one-term Taylor series expansion as

$$R \approx R_0 + \left. \frac{\partial R}{\partial T} \right|_{T_0} \bullet \delta T = R_0 \left(1 + \frac{1}{R_0} \left. \frac{\partial R}{\partial T} \right|_{T_0} \bullet \delta T \right). \quad (3.14)$$

This can be represented as

$$R \approx R_0 (1 + \alpha \bullet \delta T), \quad (3.15)$$

where α is the temperature coefficient of resistance:

$$\alpha = \frac{1}{R} \frac{\partial R}{\partial T}. \quad (3.16)$$

If we assume that the small-signal response of a generic transducer can be approximated using the one-term Taylor series expansion

$$Z_{transducer} \approx Z_0 (1 + \alpha \bullet \delta S), \quad (3.17)$$

where α is the transducer response, then

$$\frac{\partial Z_{transducer}}{\partial S} = Z_{transducer} \cdot \alpha . \quad (3.18)$$

Substituting (3.18) into (3.13) yields the final result

$$\frac{1}{O} \frac{\partial O}{\partial S} = \left[\frac{Z_{transducer}}{O} \frac{\partial O}{\partial Z_{transducer}} \right] \cdot \alpha . \quad (3.19)$$

For convenience, the operator Ψ is defined as operating on an observed parameter O as

$$\Psi(O) = \frac{Z}{O} \frac{\partial O}{\partial Z} \quad (3.20)$$

and is used as the figure of merit when evaluating the sensitivity of the tag circuit. This allows the consideration of the tag behavior separately from the transducer behavior.

This metric can be used to examine how the deviation in the magnitude of the impedance of the reader coil, $\Delta|Z|$, behaves as a function of tag resistance:

$$\Psi(\Delta|Z|) = \frac{R_{tag}}{\Delta|Z|} \frac{\partial \Delta|Z|}{\partial R_{tag}} . \quad (3.21)$$

This equates to the percent change in the output due to the percent change in tag resistance.

If $\Delta|Z|$ is indeed directly proportional to R_{tag}^{-1} , that is $\Delta|Z| = \text{const} \cdot R_{\text{tag}}^{-1}$, then $\psi(\Delta|Z|)$ would be equal to -1. Figure 3.16 shows that when $R_{\text{transducer}}$ becomes large compared to R_{tagcoil} , $|\psi(\Delta|Z|)|$ does approach the value one. Due to the fact that $\Delta|Z|$ asymptotically approaches a finite value when $R_{\text{transducer}} < R_{\text{tagcoil}}$, $\psi(\Delta|Z|)$ rolls off as $R_{\text{transducer}}$ becomes small. In order to display the data in a log-log format, the absolute value of the sensitivity is shown in the following plots.

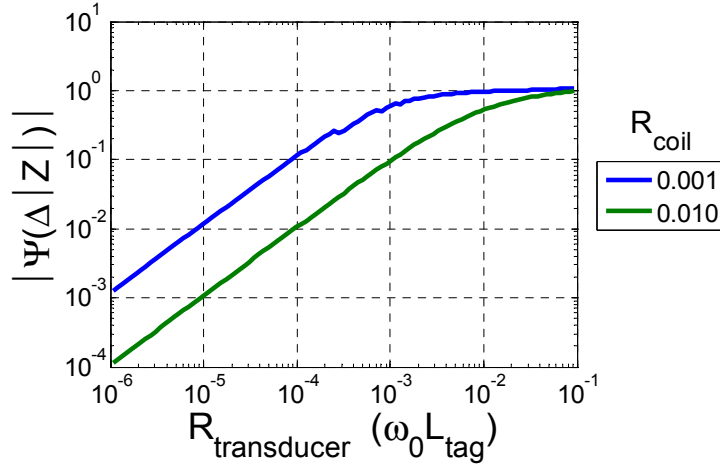


Figure 3.16 Due to the finite tag coil resistance, the sensitivity of the circuit goes to zero when $R_{\text{transducer}} \ll R_{\text{tag coil}}$.

The sensitivity of the phase dip of the impedance shows a similar behavior, as seen in Figure 3.17. As expected, $R_{\text{tag coil}}$ affects the roll off of $\psi(\Delta\theta)$ at low $R_{\text{transducer}}$. Because $\Delta\theta$ is also proportional to R_{tag}^{-1} , $|\psi(\Delta\theta)|$ also approaches a constant value of 1 when the transducer resistance is approximately three times the tag coil resistance, the same as for the magnitude deviation.

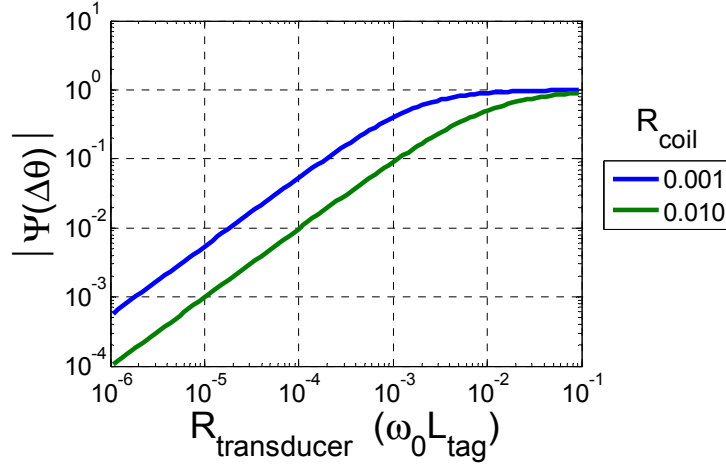


Figure 3.17 The sensitivity of the phase to $R_{transducer}$ appears to approach a constant when $R_{transducer}$ becomes large.

3.1.2.3 Coupling Factor Dependence

In addition to the affects of the lumped element circuit components in the sensor system, the coupling between the reader and the tag coils also plays an important role in the behavior of the overall circuit. As mentioned previously, the coupling factor k can range from zero when there is no coupling between the two coils to one when there is complete or perfect coupling; k is a function of both coil geometry as well as the spatial orientation between the reader and tag. Once fabricated, the geometry of the reader and tag coils should remain constant; however, the alignment of the two coils is a function of several parameters including the relative angle and the separation both vertically and horizontally, as pictured in Figure 3.18.

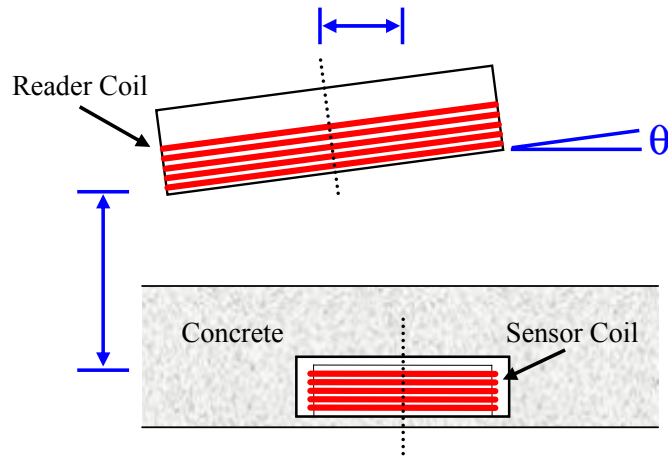


Figure 3.18 The coupling between the reader and tag coil is a function of the coil geometry as well as how they are aligned with one another.

As the completed sensors are expected to be embedded inside of structures, for example in a concrete bridge deck, once placed, the sensors most likely will not be visible to an inspector. As such, the two coils may not always be aligned the same way during successive measurements. While it may be simple to ensure the two coils are roughly parallel, the sensor's location is unlikely to be precisely known, making the axial alignment of the sensors more difficult. Also, although once in place the depth of an individual sensor should not change, the vertical spacing between the reader and sensor may differ for different sensors. The total spacing between the reader and sensor would also depend on the spacing between the reader and the surface of the structure, which may vary from one measurement to another.

It is important to consider how these variations in reader to tag distance affect the coupling factor k and in turn how variations in k affect the measured impedance. Figure 3.19 shows an example of k as a function of vertical coil separation for two coils. The value of k was computed using Nagaoka's formula for coil inductance and Neumann's Form for determining the mutual inductance, the

details of which are discussed in Chapter 4 [23, 24]. When the coils are very close, the coupling is nearly perfect; as the coils are moved apart, k ultimately falls as one over the distance cubed.

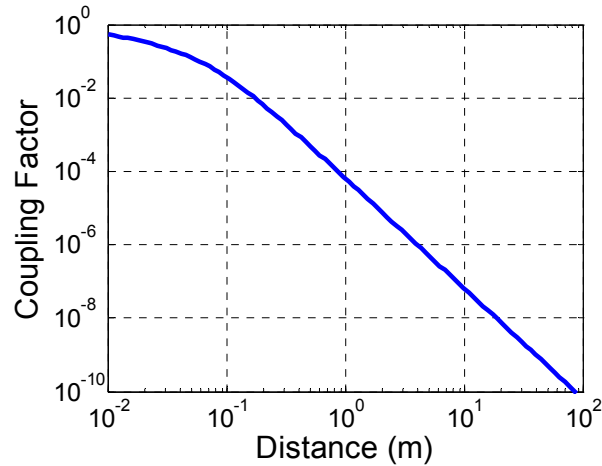


Figure 3.19 As two coils are moved apart, the coupling factor falls as one over the distance cubed.

The tag circuit presented in Figure 3.1 was simulated for varying values of k and the resulting reader coil input impedance is shown in Figure 3.20. As discussed earlier, when the tag resistance is zero, the magnitude of the impedance is infinite and the phase dip is constant at 180 degrees. This behavior is independent of the coupling factor so long as k is greater than zero. Once a finite tag resistance is included, both $\Delta|Z|$ and $\Delta\theta$ are dependent on the coupling factor and are proportional to k^2 . As the coupling becomes strong, the phase dip eventually saturates and therefore becomes independent of k . The value of k this occurs at is dependent on the tag resistance.

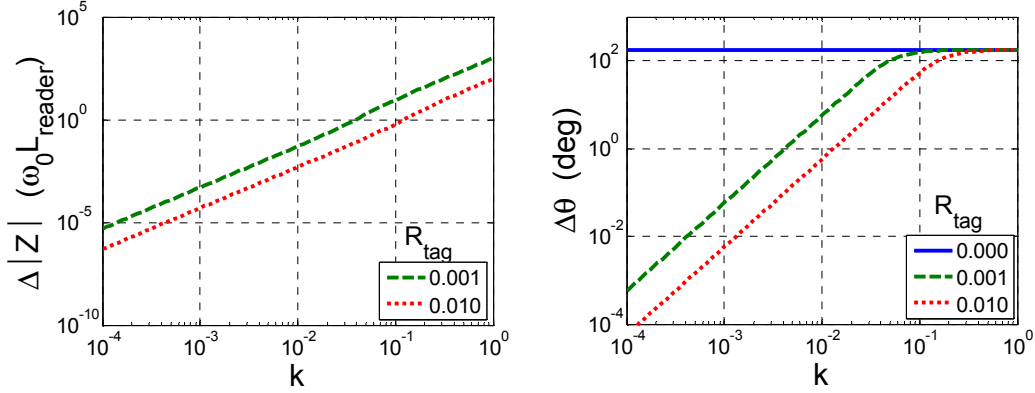


Figure 3.20 Both the magnitude and phase show a strong dependence on the coupling between the reader and tag.

As $\Delta|Z|$ and $\Delta\theta$ are proportional to k^2 and k is proportional to distance cubed, both $\Delta|Z|$ and $\Delta\theta$ are dependent on the distance to the sixth power. In a threshold type sensor, where a resistance changes from very low to very high values, this dependence may not be important. In such a case, the mere presence or absence of the resonance would be enough to indicate the state of the sensor. In fact, this is very similar in principle to how commercial EAS systems work. However, if it is necessary to be able to estimate an actual value of resistance and/or monitor how it changes over time, the variability of the deviation in phase and magnitude of the input impedance due to the coupling factor could lead to ambiguous or incorrect results. As such, another method of monitoring the tag resistance would be beneficial.

3.2 QUALITY FACTOR

In the previous section, the resistances used in the impedance evaluations were referenced in relation to the impedance of the inductor. This practice is fairly common in dealing with energy storage devices such as inductors and capacitors and is related to the quality factor, or Q , of a device or circuit. Q is conventionally

defined as the ratio of the amount of energy stored in a circuit to the amount of energy dissipated. For a simple inductor with finite resistance, Q can be expressed as

$$Q = \frac{\omega L}{R} . \quad (3.22)$$

From (3.22), it is clear that the previous normalization of the tag resistance to $\omega_0 L_{\text{tag}}$ is in fact $1/Q$ of the tag inductor on resonance.

When an inductor and capacitor are combined to form a resonant as shown in Figure 3.21, it is possible to discuss the Q of the resonant circuit itself.

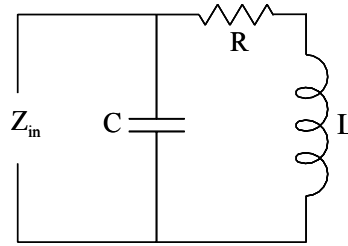


Figure 3.21 Simple RLC resonant circuit used for analyzing the quality factor.

On resonance, that is $\omega = \omega_0 = 1/\sqrt{L \cdot C}$, the Q can be expressed as

$$Q = \frac{\omega_0 L}{R} . \quad (3.23)$$

It can also be shown that the Q of the circuit is related to the shape of the impedance curve as follows

$$Q = \frac{\omega_0}{\Delta\omega}, \quad (3.24)$$

where $\Delta\omega$ is the width of the curve at the 3dB-down points [25]. Using (3.24), it is possible to determine the Q of the circuit from the shape of the measured impedance curves. Then, using (3.23), it is possible to determine the resistance of the circuit.

Figure 3.7 showed that the width of the phase dip due to the tag resonance is a function of the tag resistance. A new measurand is proposed which is the ratio of the frequency of minimum phase and the width of the resonance. This ratio is referred to as the pseudo-Quality factor or pseudoQ:

$$pseudoQ \equiv \frac{\omega_{\theta_{\min}}}{\Delta\omega}. \quad (3.25)$$

The width is defined as the full-width half-max (FWHM) of the phase curve. The values $\Delta\omega$ and $\omega_{\theta_{\min}}$ are shown in Figure 3.22. This value is referred to as the pseudoQ in order to differentiate it from the actual Q of the entire magnetically coupled circuit as it relates to energy stored and energy dissipated.

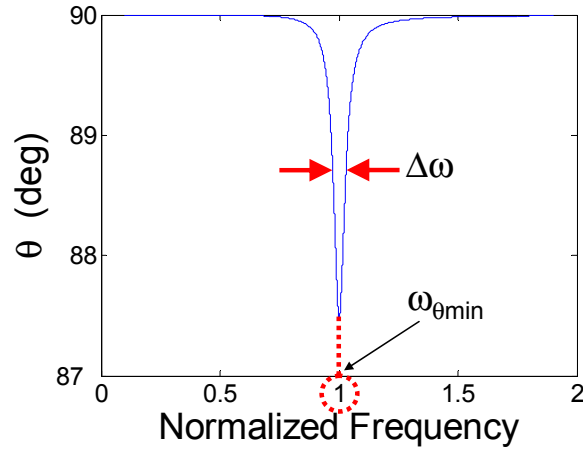


Figure 3.22 *pseudoQ* is calculated from the width of the resonance (FWHM) and the frequency at which the minimum phase occurs.

3.2.1 Resistance Dependence

In order to assess the viability of using pseudoQ as a means of determining the sensor resistance, the impedance data computed for the magnitude and phase deviation analysis above was re-examined. This was done by examining the phase data and finding the width of the dip in the phase curve at half of the maximum phase dip. Figure 3.23 shows that pseudoQ is indeed a function of the sensor resistance. Similar to both the magnitude and phase deviations discussed above, pseudoQ is proportional to R_{tag}^{-1} and in fact follows the form $\text{pseudoQ} = \omega_0 L_{\text{tag}} / R_{\text{tag}}$ as hypothesized. However, as R_{tag} becomes small, the pseudoQ value saturates.

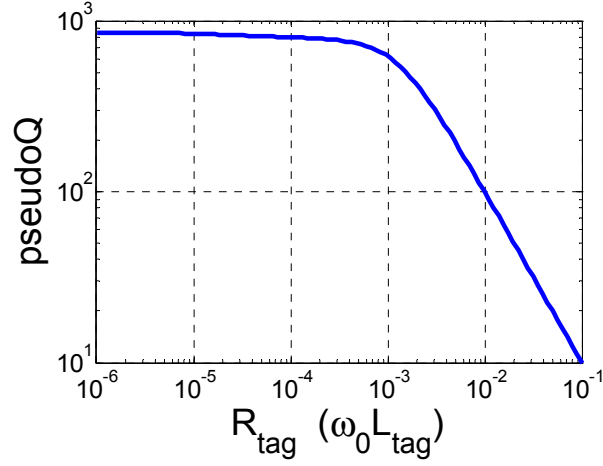


Figure 3.23 Similar to the magnitude and phase deviations discussed above, $pseudoQ$ is a function of R_{tag}^{-1} . The $pseudoQ$ saturates at low sensor resistance when the phase of the impedance saturates at -90 degrees.

This is due to the fact that as the sensor resistance becomes very small, the value of the impedance begins to approach the limits expressed in Equation (3.8). As mentioned, near this limit the phase angle quickly transitions from +90 degrees to -90 degrees for the interval $\omega_0 < \omega < \omega_0 / \sqrt{1-k^2}$. As such, the value of $\omega_0 / \Delta\omega$ saturates at

$$\frac{1}{1 - \sqrt{1-k^2}}. \quad (3.26)$$

Evaluating this expression for the value of $k=0.05$ used in the original impedance calculations leads to a value of approximately 800, which agrees with the data presented in Figure 3.23. This is a clear indication that although $pseudoQ$ may be equal to Q_{tag} over a region of R_{tag} , ultimately the values are not the same as the true quality factor of the tag would not saturate for small values of R_{tag} .

3.2.2 Coupling Factor Dependence

The reason for moving away from the relatively simple to measure quantities $\Delta|Z|$ and $\Delta\theta$ was their strong dependence on the distance between the reader and the tag; therefore, it is important to determine how pseudoQ varies with coupling factor and hence, distance. Figure 3.24 shows a plot of pseudoQ extracted for two different tag resistances as k is varied.

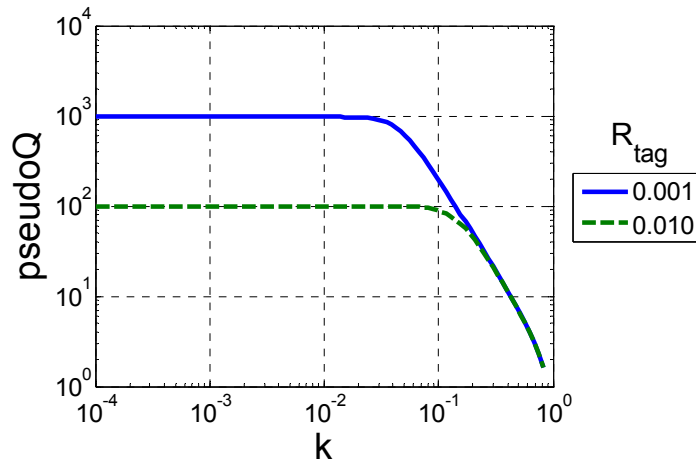


Figure 3.24 For low coupling factors, pseudoQ is independent of coupling factor.

For low coupling factors, pseudoQ is independent of k and is equal to the value $\omega_0 L_{\text{tag}} / R_{\text{tag}}$. However, it is important to keep in mind that k cannot be arbitrarily low as the signal due to the tag will eventually fall below the detectable limits of the measurement equipment. As the coupling factor increases, pseudoQ begins to drop. It may appear that as the coils become tightly coupled the circuit does not perform as well, which seems counter-intuitive. However, what actually happens is that, similar to the behavior when R_{tag} goes towards zero, for large coupling factors the phase saturates at -90 degrees when $\omega > \omega_0$ and therefore $\Delta\omega$

becomes very wide. An example is shown in Figure 3.25 where k is 0.8 and R_{tag} is $0.01 \omega_0 L_{\text{tag}}$.

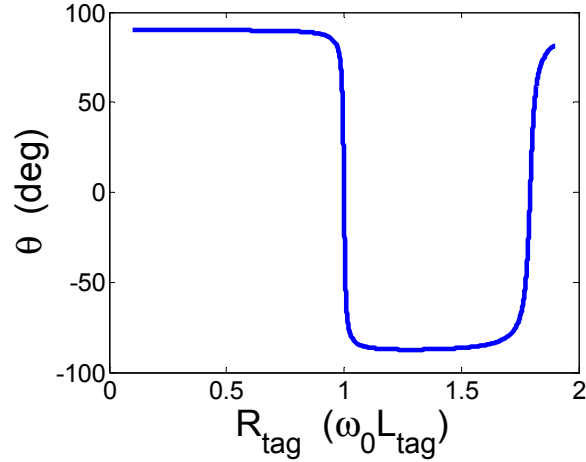


Figure 3.25 When the coupling between the reader and tag becomes very high, the phase saturates at -90 degrees and $\Delta\omega$ becomes very wide, approaching infinity.

As will be discussed in more detail later, this effect is of little concern in practice as the coupling factor is usually fairly small.

3.2.3 Coil Resistance Effects

As was the case in the earlier analysis, it is important to consider how finite coil resistances in both the reader and sensor inductors might affect pseudoQ. Here, the effects of the reader coil are analyzed first. Figure 3.26 shows a plot of pseudoQ for three different coil resistances. As is shown, the reader coil resistance has almost no effect on the calculated pseudoQ.

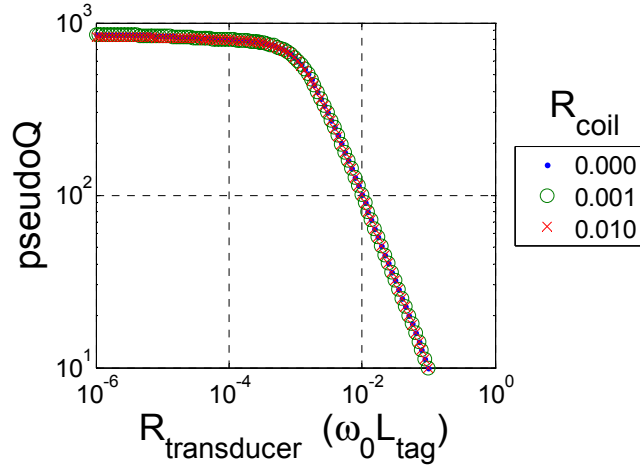


Figure 3.26 Finite reader coil resistance has little effect on the calculated pseudoQ.

Unlike the finite reader coil resistance, including a finite tag coil resistance has an obvious affect on the calculated pseudoQ. The effect is similar to that seen in the magnitude and phase deviation discussed above in that the sensor coil resistance affects the upper bound of pseudoQ as the sensor transducer resistance becomes small. The results of this simulation are shown in Figure 3.27.

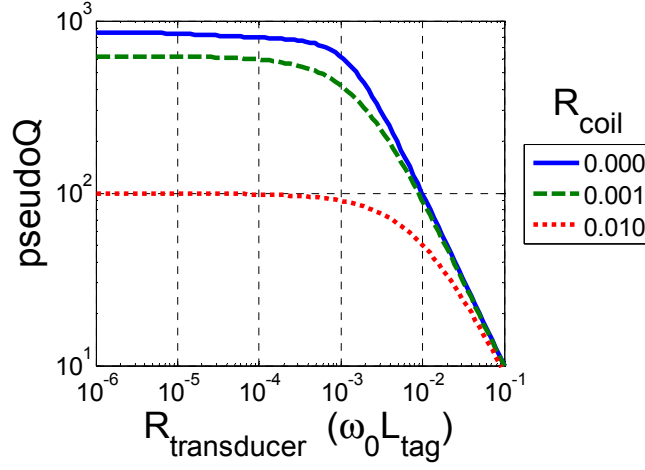


Figure 3.27 Finite tag coil resistance lowers the maximum value of pseudoQ achieved as the transducer resistance becomes small.

Up until now, the tag resistance has been swept from 10^{-6} to $0.1 \omega_0 L_{\text{tag}}$; however, the behavior of the circuit does not change much below $10^{-4} \omega_0 L_{\text{tag}}$. It may also be interesting to see how the circuit behaves as the tag resistance reaches the same order of magnitude of $\omega_0 L_{\text{tag}}$. Figure 3.28 shows the results for two different tag coil resistances while the transducer resistance is swept from 10^{-4} to $10 \omega_0 L_{\text{tag}}$.

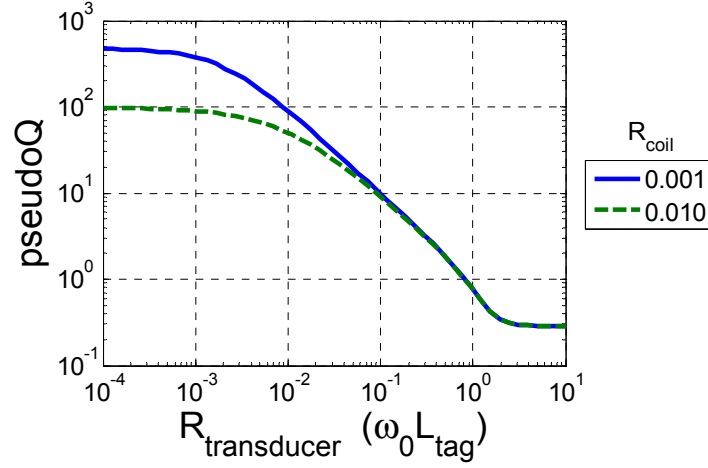


Figure 3.28 Extending the range of $R_{\text{transducer}}$ reveals that the relationship between pseudoQ and R changes around $R = \omega_0 L_{\text{tag}}$.

The results indicate that as $R_{\text{transducer}}$ approaches $\omega_0 L_{\text{tag}}$, that pseudoQ deviates from the $R_{\text{transducer}}^{-1}$ behavior. This can be explained by looking at the two components of pseudoQ , $\Delta\omega$ and $\omega_{\theta\min}$, which are plotted together in Figure 3.29.

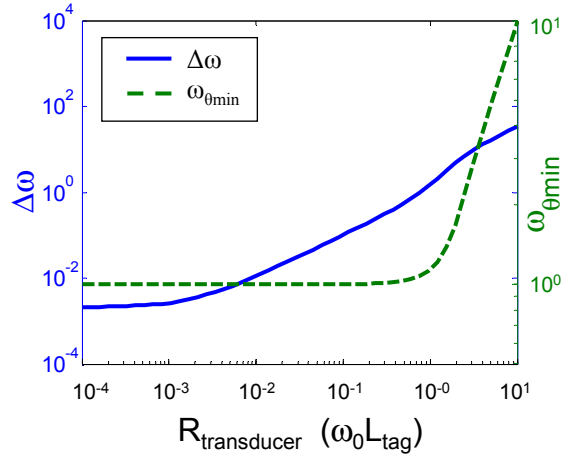


Figure 3.29 The behavior of $\omega_{\theta\min}$ helps explain the behavior of pseudoQ as $R_{\text{transducer}}$ becomes large.

This plot reveals that although $\Delta\omega$ continues to increase with increasing transducer resistance, $\omega_{\theta\min}$ begins to deviate from ω_0 when $R_{\text{transducer}}$ is equal to $\omega_0 L_{\text{tag}}$. Note that the scales on the two y-axes are not the same. Although it may appear as if $\omega_{\theta\min}$ is rising much faster $\Delta\omega$, they are actually somewhat similar rates of change. It may seem as if this would suggest that despite the variability seen around when $R_{\text{transducer}}$ is comparable to $\omega_0 L_{\text{tag}}$, $\Delta\omega$ would be a better measurand than pseudoQ due to its behavior at higher transducer resistances. However, it is important to note that in a real system, $\Delta\omega$ would likely exceed practical bandwidth constraints for large resistances anyway. Also, although these numbers can be computed to high precision on a computer using the input impedance equation, the phase dip at $R_{\text{transducer}} = \omega_0 L_{\text{tag}}$ is on the order of 0.1 degrees and would likely approach the resolution limits of practical measurement systems which could be deployed in the field in real-world situations.

When the sensitivity of pseudoQ to changes in $R_{\text{transducer}}$ is examined, the results, plotted in Figure 3.30, are similar to those found earlier for the magnitude and phase.

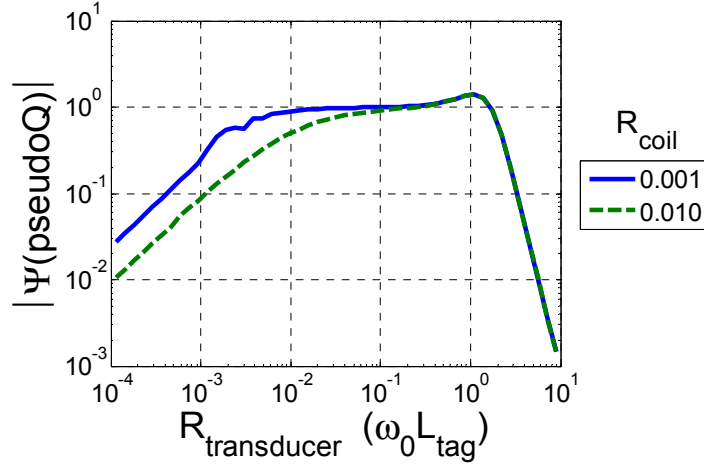


Figure 3.30 There is a region of relatively flat sensitivity when $R_{transducer}$ is greater than $R_{tag\ coil}$ and less than $\omega_0 L_{tag}$.

When $R_{transducer}$ is low, $R_{tag\ coil}$ dominates and $|\psi(\text{pseudoQ})|$ drops off. As $R_{transducer}$ becomes large enough, approximately three times $R_{tag\ coil}$, $\psi(\text{pseudoQ})$ appears to approach a constant value. Finally, when $R_{transducer}$ becomes large and pseudoQ levels off as discussed above, the sensitivity quickly drops off. Immediately before this drop-off, there is a small region of higher sensitivity. However, concerns of measurement bandwidth, minimum detectable phase, and the desired dynamic range of the transducer may make it more practical to work at lower resistances.

3.2.4 L and C Effects

Throughout the above analysis, the effects of L_{reader} , L_{tag} , and C_{tag} have not been explicitly addressed. However, all of the calculations were done in a “normalized” fashion, where ω was referenced to ω_0 and resistance was referenced to $\omega_0 L$, such that changing L_{reader} , L_{tag} , or C_{tag} would not have an effect on the data as it has been presented. For example, as shown in Figure 3.31, if L_{tag} is increased

by a factor of 1000, the response of pseudoQ as a function of transducer resistance, will not change.

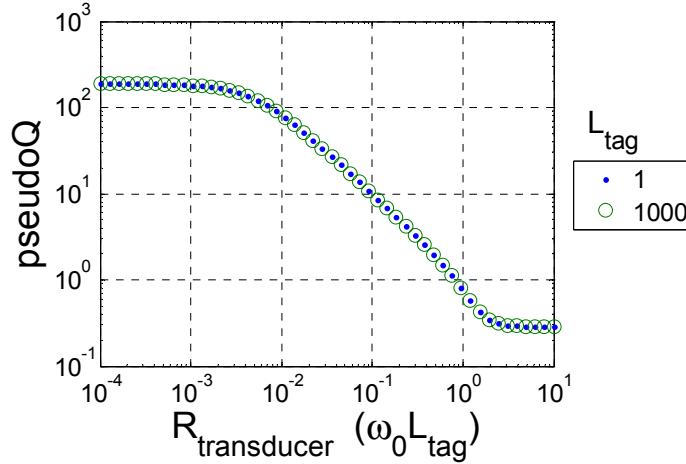


Figure 3.31 Changing the tag inductance does not affect the behavior of the normalized circuit.

This does not mean, however, that these values have no affect on the circuit. The inductance and the capacitance of the tag set the actual frequency at which the circuit will resonant and therefore the frequency that the measurement equipment will need to work at. The actual value of L_{tag} also effects the actual values of resistance which can be used. For example, if L_{tag} is originally 1 nH and C_{tag} is 1 nF, then ω_0 is approximately 1×10^9 rad/s and $R = \omega_0 L_{\text{tag}}$ is 1 Ω . If L_{tag} is increased by a factor of 1000, then ω_0 is 31.6×10^6 rad/s and $R = \omega_0 L_{\text{tag}}$ is about 31.6 Ω . Alternatively, C_{tag} could be decreased when L_{tag} is increased to keep ω_0 the same. In this case L_{tag} is 1 μH and C_{tag} is 1 pF, yielding a resonant frequency of 1×10^9 rad/s and $R = \omega_0 L_{\text{tag}}$ of 1 k Ω .

Another important point to consider is how L_{reader} and L_{tag} affect the mutual inductance M . Throughout the investigation of circuit behavior above, the coupling

factor k was treated as an independent parameter. In reality, changing the parameters of either coil – either the diameter or the number of turns – will affect both the self-inductance of that coil and the mutual inductance between the reader and the tag. However, this does not invalidate treating k as an independent parameter. As the mutual inductance is a function of the geometry of the two coils and their spatial relation to one another, several different sets of coils with varying self inductances could be arranged so that they all have the same coupling factor k .

While pseudoQ has been shown to be relatively independent of k , the phase data which pseudoQ is derived from was shown to depend on k and therefore the distance between the coils. The minimum detectable phase change of the measurement equipment and the dependence of the phase dip on coupling factor set the maximum distance at which the tag can be reliably detected.

3.3 DESIGN CONSIDERATIONS

The above discussion investigates the performance of a resonant tag based wireless sensing platform. A metric was developed which can be used to evaluate the performance of different measurands under the influence of different circuit parameters. Given a specific transducer, this information can be used as a starting point for selecting values for the rest of the circuit. In addition, if there is some flexibility in the design of the transducer itself, it could be tailored to better take advantage of the circuit performance.

Using a simple circuit model, the proposed design was evaluated for use with a resistance based transducer. Several trends in the circuit performance were revealed which can be used as a set of design guidelines. First, it is clear that if the reader coil is to be moved between repeated measurements and it cannot be guaranteed that the reader and tag coil will be aligned the same way each time, using the magnitude or phase of the measured impedance directly as an indicator of tag resistance is not the best solution. While these values are both functions of the

tag resistance, they are also strongly affected by the coupling factor between the reader and tag inductor coils.

The pseudoQ, which is based on the width of the measured phase curve, is related to the quality factor of the tag circuit and was shown to be generally independent of the coupling factor except for very high values of k . Analysis of the circuit behavior as a function of tag resistance revealed that pseudoQ saturates for very low and high values of R_{tag} . At the low end, this is due to the parasitic resistance of the tag's inductor coil. Once the transducer resistance is approximately three times the parasitic coil resistance, this effect is negligible and pseudoQ is a strong function of the transducer resistance itself. As the transducer resistance becomes comparable to the tag's inductor impedance on resonance, $\omega_0 L_{\text{tag}}$, pseudoQ behavior begins to change due to ω_{0min} deviating from ω_0 . Although there are other measurands, such as $\Delta\omega$, which continue to behave as a function of tag resistance beyond the point where pseudoQ saturates, due to constraints such as the bandwidth, phase resolution, and signal to noise ratio of the measurement system, very little would be gained by using such a measurand in practice.

In between these two limits, that is

$$3 \cdot R_{\text{tagcoil}} \leq R_{\text{transducer}} \leq \omega_0 L_{\text{tag}}, \quad (3.27)$$

pseudoQ is proportional to $R_{\text{transducer}}^{-1}$ and the sensitivity of pseudoQ to changes in transducer resistance is relatively flat and this is the desired operating range for the sensor. If a transducer with a given nominal resistance is to be used, this can aid in the selection of appropriate values for L_{tag} and ω_0 , and by extension, C_{tag} . Alternatively, if a specific operating frequency is desired or physical constraints on the sensor design dictate a practical range of tag inductance, this information can be

used to select an appropriate transducer resistance. The range over which $\psi(\text{pseudo}Q)$ is flat also gives an indication of the usable dynamic range of the sensor's transducer. Also, as the lower bound of the operating range is defined by the tag coil's parasitic resistance, it is advantageous to keep this value as small as possible. While some parasitic loss is unavoidable, good design practices should be used to avoid introducing unnecessary losses.

Recalling the original definition of Q given in (3.23), the relationship in (3.27) can be expressed as

$$1 \leq Q \leq \frac{1}{4} Q_0, \quad (3.28)$$

where Q_0 is the “intrinsic” Q of the inductor, that is, the Q due to the inductor and its associated parasitic loss, given by

$$Q_0 = \frac{\omega_0 L_{tag}}{R_{tagcoil}}. \quad (3.29)$$

This specifies the range over which the Q of the tag circuit can vary and illustrates the fact that keeping the inductor coil losses low raises the intrinsic Q of the circuit and hence increases the range of transducer resistances over which the sensor can be operated.

Although the motivation for this investigation comes from interest in a sensor for detecting corrosion in steel reinforced concrete, the information gathered is potentially useful for any sensor which uses a resistance based transducer. Further, using the figure of merit derived above, this analysis could be extended to other transducers which undergo a general change in impedance due to their stimulus.

CHAPTER 4

Embedded Corrosion Sensor

4.1 EXPANDED CIRCUIT MODEL

The idealized circuit model using normalized component values discussed in the previous chapter was useful for examining basic circuit behavior and formulating general design considerations. In order to further investigate how an actual circuit may perform in the real world, several changes were made to the model.

4.1.1 Physical Based Circuit Values

The first change was to abandon the normalizations used in the earlier simulations. In order to properly simulate the circuit, real component values must be used. For some of the circuit elements, like tuning capacitors and transducers with a known resistance, this is a simple matter of substituting in the component values. The coil inductances and their accompanying parasitic resistances must either be measured from actual coils or estimated based on the dimensions of the proposed coil. Both of these methods have been employed when simulating various coil designs throughout this work.

The original desire to be able to compute the circuit parameters of both the reader and tag coils came from an investigation of the sensor system using genetic algorithms [26]. After an investigation of the literature, Nagaoka's formula was chosen for calculating the coil inductance based on the geometry of the coil. Nagaoka's formula takes the basic equation for the inductance of a solenoid and applies a geometry correction factor dependent on the length of the coil compared to

the radius [23]. The formula calculates the inductance L of a solenoid based on the length ℓ , radius r , and the number of turns N of the coil and is expressed as

$$L = \frac{\mu_0 \pi r^2 N^2}{\ell} \xi \quad (\text{H}), \quad (4.1)$$

where ξ is Nagaoka's geometry correction factor:

$$\xi = \frac{2\beta}{\pi} \left[\left(\ln \left(\frac{4}{\beta} - \frac{1}{2} \right) + \frac{\beta^2}{8} \left(\ln \frac{4}{\beta} + \frac{1}{8} \right) - \frac{\beta^4}{64} \left(\ln \frac{4}{\beta} - \frac{2}{3} \right) \dots \right] \quad (4.2)$$

and

$$\beta = \frac{\ell}{2r}. \quad (4.3)$$

The dimensions of the coil are as shown in Figure 4.1

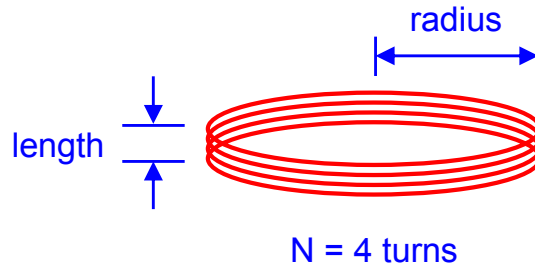


Figure 4.1 The inductance of short solenoids can be computed based on the length, radius, and number of turns using Nagaoka's formula.

The values computed using this method have been checked against actual coils which have been built and measured in the lab. The calculated and measured values typically agree within five percent; this margin of error was considered acceptable for modeling purposes.

The resistance of each coil was originally computed at DC using the length, diameter, and conductivity of the wire. However, the results obtained using this method were consistently lower than the values required in order for the simulation results to agree with measured circuit behavior. The estimate of coil resistance based on the geometry of the coil was improved by taking into account the frequency dependent skin effect on the resistance of the wire [24]. The resistance per unit length of wire is computed using the following simplification of the formula for the impedance of round wires:

$$R_{wire} = \Re \left\{ \frac{j}{2\pi r_{wire}} \sqrt{\frac{j\omega\mu_0}{\sigma}} \frac{J_0(jx)}{J_1(jx)} \right\} \quad (\Omega/\text{m}), \quad (4.4)$$

where

$$x = r\sqrt{j\omega\mu_0\sigma} \quad (4.5)$$

and J_0 and J_1 are the Bessel functions of the first kind, 0th and 1st order respectively, σ is the conductivity of the wire, and r_{wire} is the cross-sectional radius of the wire.

The value of the mutual inductance between the reader and tag coils, in henries, can also be computed based on the geometry of the two coils and their orientation using Neumann's Form [24]. For these calculations, it is assumed that the coils are coaxial, that is, the only separation between the coils is vertical spacing. Neumann's Form gives the mutual inductance as

$$M = N_{reader} N_{tag} \mu \sqrt{r_{reader} r_{tag}} \left[\left(\frac{2}{t} - t \right) K(t) - \frac{2}{t} E(t) \right] \quad (H), \quad (4.6)$$

where

$$t^2 = \frac{4r_{reader}r_{tag}}{d^2 + (r_{reader} + r_{tag})^2} \quad (4.7)$$

and r_{reader} and r_{tag} are the radii of the two coils, N_{reader} and N_{tag} are the number of turns of each coil, d is the distance between the two coils, and $K(t)$ and $E(t)$ are complete elliptic integrals of the first and second kind. The traditional argument of the elliptic integral k has been replaced with t to avoid confusion with the coupling factor. Again, the values produced using this formula were compared against numbers generated by fitting actual measured data from earlier experiments. The calculated and empirical values agreed quite well [22].

The final addition to the circuit model is the inclusion of a parasitic capacitance in the reader coil circuit, as shown in Figure 4.2. This represents the capacitance of the connector which is used to connect the reader coil to the measurement equipment. Measurements made on the connectors typically yield a connector capacitance of approximately 2 pF; subsequent comparisons between modeled and measured data suggest this is a reasonable figure.

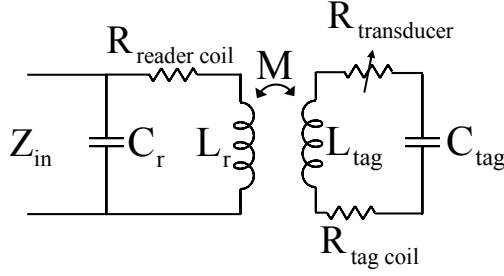


Figure 4.2 The full circuit model also includes a parasitic capacitance from the reader coil connector.

4.1.2 Coil Geometry Considerations

At this point it is worth discussing how the coil geometry might interact with the guidelines developed in the previous chapter. As mentioned at the end of that chapter, the intrinsic Q of the inductor (Q_0) sets a limit on the dynamic range of the system. To achieve the largest dynamic range possible, the intrinsic Q should be made as high as possible. Recall that Q is $\omega L/R$, which suggests that making ω and L large while keeping R small will increase Q_0 . However, ω , L , and R are interdependent and care must be taken to understand how the overall geometry plays into these relationships.

There are a large number of parameters which can affect the inductance and resistance of each coil as well as the coupling between the reader and the sensor. The analysis of coil geometry effects can be simplified by considering real world constraints on the coil size. For example, the coupling between the reader and sensor can be increased by increasing the diameter of the coils. However, the sensor must ultimately be designed so that it does not adversely affect the structure in which it is embedded. Ultimately, smaller sensors would be less likely to affect the structure and the maximum dimensions of the tag coil will be dictated not by circuit constraints but by the “construction deities”.

With the coil radius and length fixed by external constraints, the variables of interest are the operating frequency and the number of turns in the tag coil. Recalling that the coupling factor can be expressed in terms of the mutual and self-inductances of the coils as

$$k = \frac{M}{\sqrt{L_{reader}L_{tag}}}, \quad (4.8)$$

substituting (4.1) and (4.6) for L and M yields

$$k = \frac{N_{reader}N_{tag}\mu_0\sqrt{r_{reader}r_{tag}}\left[\left(\frac{2}{t}-t\right)K(t)-\frac{2}{t}E(t)\right]}{\sqrt{\frac{\mu_0\pi r_{reader}^2 N_{reader}^2}{\ell_{reader}}\xi_{reader}\frac{\mu_0\pi r_{tag}^2 N_{tag}^2}{\ell_{tag}}\xi_{tag}}}. \quad (4.9)$$

Equation (4.9) can be simplified to

$$k = \frac{\left(\frac{2}{t}-t\right)K(t)-\frac{2}{t}E(t)}{\pi\sqrt{\frac{r_{reader}r_{tag}}{\ell_{reader}\ell_{tag}}\xi_{reader}\xi_{tag}}}, \quad (4.10)$$

which is only a function of the external coil dimensions and the separation between the coils. It is not a function of the number of turns in either coil or the operating frequency. The result is that the operating frequency and the length of the tag coil can be adjusted to maximize the intrinsic Q of the tag without affecting the coupling and by extension, the read range.

At this point it would seem that making Q_0 as large as possible by adjusting ω and N_{tag} would give the best dynamic range for the sensor. However, it is important to consider the possibility that there is also some loss associated with the tag capacitor. The capacitor has its own associated Q which can be expressed as

$$Q_{\text{cap}} = \frac{\omega C}{G} = \frac{1}{\tan \delta}, \quad (4.11)$$

where G is a conductance in parallel with the capacitor and $\tan \delta$ is the loss tangent of the capacitor's dielectric. This can be combined with the Q of the inductor to give the overall intrinsic Q as

$$Q_0 = \left[\frac{1}{Q_{\text{coil}}} + \frac{1}{Q_{\text{cap}}} \right]^{-1} = \left[\frac{R}{\omega L} + \tan \delta \right]^{-1}. \quad (4.12)$$

If $\tan \delta$ is assumed to be an intrinsic property of the capacitor that is relatively frequency independent, then Q_0 will increase with increasing Q_{coil} until the loss due to the capacitor dominates the losses in the coil. No further benefit is derived from increasing Q_{coil} beyond this point.

The effects of geometry on Q_{coil} can be analyzed by combining the expressions for the coil inductance and resistance described above. However, in order to simplify the analysis, the expression for the coil resistance in terms of the Bessel functions is approximated as

$$R_{\text{coil}} = R_{\text{DC}} \left(1 + \frac{a}{2\delta} \right), \quad (4.13)$$

where a is the radius of the wire, R_{DC} is the DC resistance of the wire, and δ is the skin depth at the operating frequency ω , given by

$$\delta = \frac{1}{\sqrt{\omega\mu\sigma}}. \quad (4.14)$$

For a wire with a circular cross-section,

$$R_{DC} = \frac{\ell_{wire}}{\pi a^2 \sigma}, \quad (4.15)$$

where ℓ_{wire} is the total length of the wire used to wind the coil, which should not be confused with the length of the coil itself, ℓ_{coil} . For a coil of given length, both a and ℓ_{wire} can be expressed in terms of ℓ_{coil} , the number of turns N , and the radius of the tag coil:

$$\begin{aligned} \ell_{wire} &= N \cdot 2\pi r_{tag} \\ a &= \frac{\ell_{coil}}{2N_{tag}}. \end{aligned} \quad (4.16)$$

Under the constraint of a fixed coil length, as N_{tag} is increased the size of the wire is decreased to keep the coil length constant. Combining the above expressions with the original expression for inductance results in

$$Q_{coil} = \frac{\omega\mu_0\pi r_{tag}\ell_{coil}\xi_{tag}\sigma}{8N_{tag} + 2\ell_{coil}\sqrt{\omega\mu\sigma}}. \quad (4.17)$$

Equation (4.17) shows that Q_{coil} grows as a function of frequency and decreases with the number of turns in the inductor coil while everything else is a constant defined by the given geometry and the material properties of the wire used to wind the coil.

Substituting (4.17) into (4.12), Q_{coil} can be related to the loss tangent of the capacitor. The resulting expression can be solved for the optimum number of turns as a function of operating frequency:

$$N_{\text{tag}} = \frac{\omega\mu_0\pi r_{\text{tag}}\ell_{\text{coil}}\xi_{\text{tag}}\sigma \tan \delta - 2\gamma\ell_{\text{coil}}\sqrt{\omega\mu\sigma}}{8\gamma}, \quad (4.18)$$

where γ is the scaling factor defining how Q_{coil} should relate to Q_{cap} in order to be in the limit where increasing Q_{coil} has little effect on the overall intrinsic Q .

When N_{tag} is computed using the geometry constraints of the current prototype sensors where r_{tag} is 3 cm, ℓ_{coil} is 6 mm, $\tan \delta$ is assumed to be 10^{-3} , and γ is set to 10, N_{tag} is negative for frequencies below 427 MHz. In order to wind a real coil, N_{tag} must be greater than or equal to one. This does not suggest that the sensor system cannot be designed to operate below 427 MHz; it only means that Q_0 due to both the inductor and capacitor will not be as high possible. The minimum frequency at which $N_{\text{tag}} \geq 1$ is referred to as the critical frequency, f_{crit} , which is shown as a function of $\tan \delta$ in Figure 4.3. The critical frequency is the frequency at which Q_0 is said to be maximized and is approximately equal to $1/\tan \delta$.

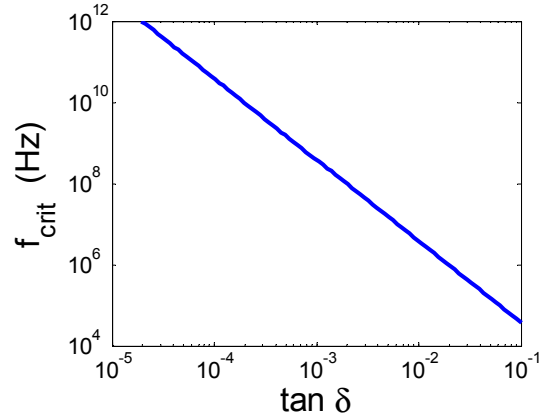


Figure 4.3 The critical frequency at which an optimum coil can be wound is a function of the loss in the capacitor.

Although it may appear that operating at a lower $\tan \delta$, that is, using a capacitor with more loss, might make designing the system easier due to a lower operating frequency, it is important to realize that this also lowers Q_0 which decreases overall performance. Also, as the frequency of operation is increased, the wavelength becomes comparable to the dimensions of the coil and the models used to derive this behavior are no longer valid. A general rule of thumb is that the largest dimension in the problem should be on the order of $\lambda/100$ or smaller. For a coil with a diameter of 6 cm, this restriction would limit the maximum operating frequency to approximately 50 MHz.

Given these constraints, the circuit can be operated at a frequency below f_{crit} and $\tan \delta$ should be kept low while Q_{coil} should be made as large as possible. While such a system may not achieve the theoretically optimal performance, in reality, the operating frequency of the system would be limited by other constraints. For example, FCC regulations will dictate which frequency bands are ultimately available for sensor operation. Additionally, low-loss capacitors with high operating frequencies may be difficult to find at a low cost. Finally, as the operating

frequency is increased, the skin depth in the medium the sensor is embedded in will decrease, limiting the depth at which the sensors can be embedded.

To summarize, (4.17) suggests that Q_{coil} should be maximized by operating at the highest possible frequency given regulations and practical constraints while using one turn of wire with a diameter that is equal to the maximum length of the coil. Practical issues may suggest the use of “ribbon” conductors, such as copper foil or pipe rather than a circular wire of large diameter.

4.2 CURVE FITTING

Throughout the analysis presented in Chapter 3, the “baseline” response of the reader portion of the circuit was known exactly and could be subtracted from the data captured in the presence of a tag. Unfortunately, this is much harder to implement in practice due to real-world constraints. Although one can argue that it should be a simple matter to measure the reader coil impedance with no tag present – for example, by positioning the reader coil in the air far from any resonant tags, there are other factors which are not as easy to control.

One such effect could come from nearby conductive objects in the environment which can affect the input impedance of the reader coil. For example, the corrosion sensors for reinforced concrete are designed to be attached to the top grid of reinforcing steel. As the arrangement of the rebar and relationship to the sensor will vary from sensor to sensor, there is no reliable way to measure the affects of the rebar at any one position and know that it will be consistent with the affects of the rebar at a different location.

A method is proposed in which only the measurement data with the sensor present is used to estimate pseudo Q . This method is based on curve fitting multiple lineshapes to the measured data in a multi-step process. The curve fitting is done in Matlab and attempts to minimize the sum of squares error between the measured data and the fit.

This method is based on the assumption that any perturbations due to the environment will have a broadband effect on the reader coil input impedance, that is, that they are non-resonant phenomena. It also assumes that the data is measured over a wide enough frequency sweep that the effects of the tag are minimal at the high and low end of the sweep. The middle portion of the data is then windowed out and the remaining data is fit using a baseline function. An example baseline fit on data from Chapter 3 is shown in Figure 4.4. The current baseline function being used is a fourth-order inverse polynomial and was chosen through trial and error when fitting early data sets.

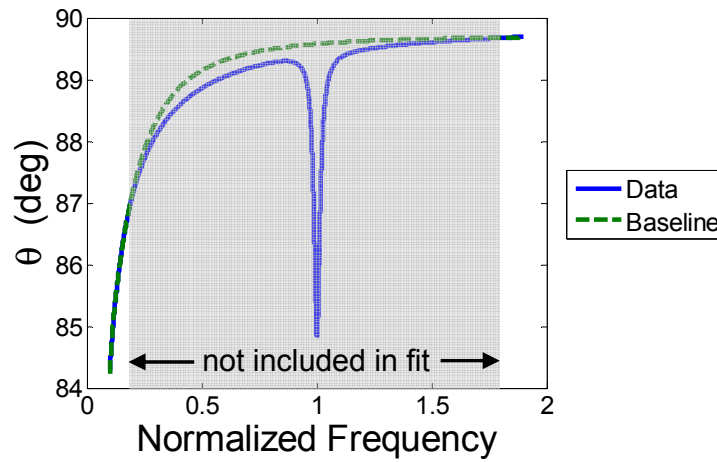


Figure 4.4 The baseline of the phase data is fit by windowing out the resonant tag behavior.

The data plotted in Figure 4.4 also help to illustrate another design consideration. When the reader response is not known ahead of time, it is helpful to keep the parasitic resistance of the reader coil low, as high reader coil resistance tends to increase the curvature of the baseline at low frequencies which can make curve fitting more difficult. It is also helpful to ensure that the resonant frequency

of the tag is above the steepest part of this curve – that is, when the inductive reactance of the reader coil dominates its parasitic resistance.

Originally, the fitting process was stopped after this first fit and the baseline was removed from the data. At this point $\Delta\omega$ and $\omega_{\theta\min}$ were estimated by simply finding the minimum of the phase curve and then interpolating the full-width half-max points. However, it was found that errors in the baseline fitting routine introduced error into the estimated pseudoQ. This was especially true when the phase dip was small, resulting in a low signal to noise ratio.

The method was modified by fitting a Lorentzian lineshape to the phase dip. The Lorentzian was chosen as it is the typical response in physical based resonant systems. The Gaussian lineshape was also tested. As expected, it produced inferior results to the Lorentzian. The Lorentzian lineshape can be expressed as

$$f(x) = \frac{1}{\pi} \frac{A(\Gamma/2)}{(x - x_0)^2 + (\Gamma/2)^2}, \quad (4.19)$$

where A is the area under the curve, x is the driving frequency, x_0 is the resonant or center frequency, and Γ is the linewidth which is dependent on the damping of the oscillator. It is relatively easy to extract pseudoQ from the coefficients of the Lorentzian as x_0 corresponds to $\omega_{\theta\min}$ and Γ is the full-width at half-maximum, $\Delta\omega$.

The Lorentzian is originally fit to the data after first removing the baseline. The original unaltered data set is then re-fit using a sum of the baseline and the Lorentzian with the previously calculated fitting parameters as the starting point for the new fit. This method appears to reduce error in the baseline fitting process and overall has resulted in good fits. The final fit of the data used in the above example is shown in Figure 4.5. The simulated phase data plotted in the figure have been

downsampled in order to aid in the visual comparison of the calculated data to the curve fit.

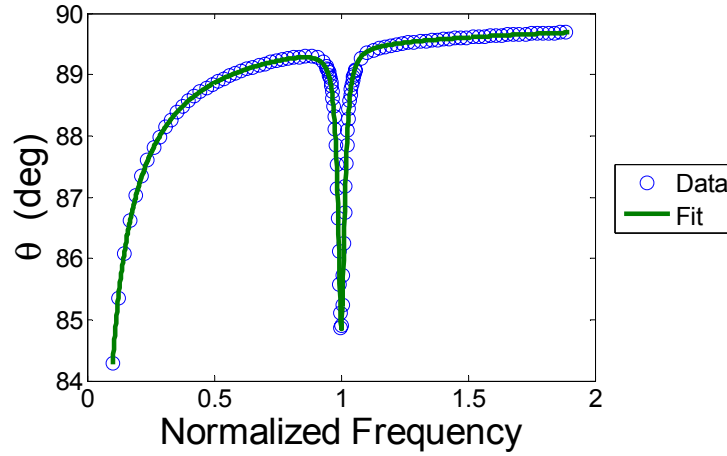


Figure 4.5 Example curve fit using polynomial baseline and Lorentzian.

The data in the previous chapter could be analyzed without the use of the above curve fitting routine due to the fact that the reader response could be computed exactly and removed from the data. A sample of this data was run through the curve fitting algorithm and compared against the results obtained by this more direct calculation using the exact reader coil impedance with no tag present. The results as a function of transducer resistance are shown in Figure 4.6.

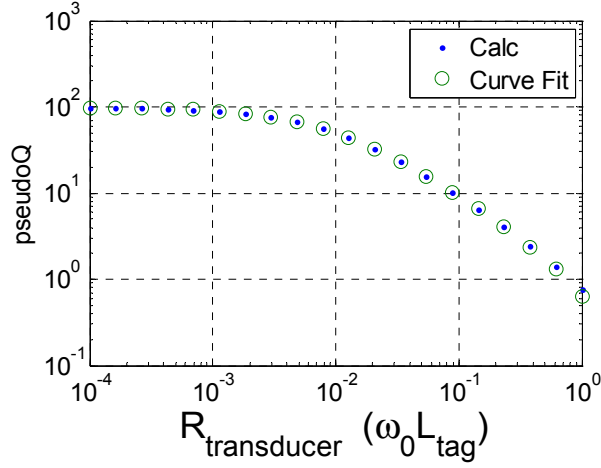


Figure 4.6 The curve fitting results agree quite well with the results calculated based on the known baseline reader coil impedance.

The curve fitting technique agrees quite well with the results obtained when the baseline response is known. The error of the curve fitting method is less than two percent over most of the range of simulated transducer resistances. As $R_{\text{transducer}}/\omega_0 L_{\text{tag}}$ approaches one, the error increases yet remains below approximately 10%. These results suggest the curve-fitting routine is relatively useful in analyzing data when separate baseline measurements are not possible.

4.3 CORROSION SENSOR

The desire to improve the original corrosion sensor came from the behavior of the resonant circuit at specific transducer impedances that severely damped the resonant response of the tag. Such behavior would make the sensor very difficult to detect in a real world environment. It was proposed that a sensing mechanism which relied on a change in resistance, rather than the original capacitance, be used.

4.3.1 Reference Coil

In the second iteration of the sensor design, the width and frequency of the resonance are extracted from the measured phase of the reader impedance and combined into the single value pseudoQ, which is a function of the tag resistance. However, as the tag resistance becomes large, the phase dip of the measured impedance becomes very small. At some point the signal to noise ratio and phase resolution of the measurement device render the resonance undetectable. This means that once the wire is sufficiently corroded, it will be impossible to detect any response from the tag.

This behavior is acceptable in implementations such as EAS anti-shoplifting systems where once the merchandise has been purchased there is no need to detect the tag anymore. However, in an embedded sensor deployed in the field, the ability to detect the sensor even after the transducer is off scale, i.e. the steel wire had corroded through, would be desirable. This ability is important to verify the location of the sensor; otherwise, no signal could either mean the wire had entirely corroded or that the reader was improperly positioned to couple to the sensor.

A simple method of providing the ability to detect the sensor regardless of the state of the transducer is to include a second resonant circuit in the sensor as pictured in Figure 4.7. This second resonant circuit is completely contained within the sensor housing. It is protected from the environment and contains no external transducer. In this way, this resonance serves as a reference and can be used to locate and verify the functionality of the sensor regardless of the state of the other resonant circuit. The two resonances are referred to as the reference and sense resonance, respectively.

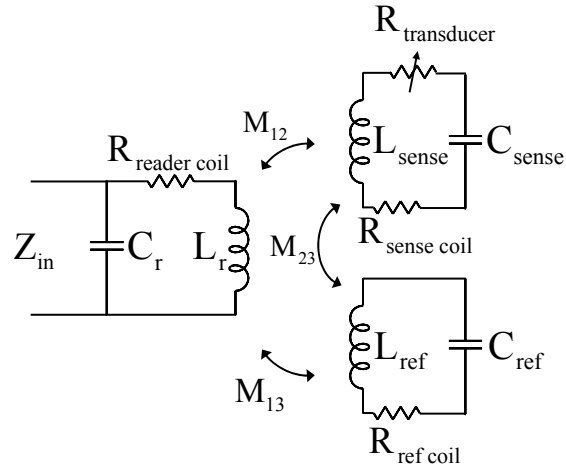


Figure 4.7 Schematic diagram of the circuit modified to include a reference resonance which is present regardless of the state of the sensor.

Figure 4.8 shows the impedance due to both the sensor and reference circuit alone as well as the combined response. Note that the response of the dual-resonant circuit is not equal to the superposition of the individual responses.

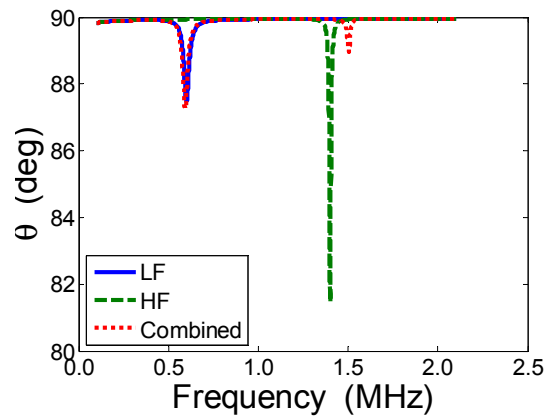


Figure 4.8 The high frequency (HF) resonance response is reduced by the presence of the low frequency (LF) resonance.

While the low frequency (LF) resonance remains relatively unchanged with the addition of the second resonance, the high frequency (HF) resonance shifts slightly in frequency and is also shallower when compared to the response produced by the HF resonance alone. The shift in resonant frequency is due to the mutual coupling between the low and high frequency coils. The reduction in the depth of the HF resonance can be explained by the application of Lenz's Law, which states that the emf induced in a closed conducting loop due to a changing magnetic field will be in a direction so as to oppose the change in the magnetic flux [27].

Consider two coaxial coplanar coils in a changing magnetic field. In the ideal case, the low frequency resonance is viewed as a short circuited loop while the high frequency resonance is an open loop. By Lenz's Law, the emf induced in the shorted coil will produce a current which opposes the change in the magnetic field. The changing magnetic field seen by the second coil is therefore reduced, producing a smaller induced voltage in the second coil than if the first coil were not present. Since no current can flow in the second coil, it does not affect the magnetic field and therefore does not affect the first coil.

As the sensor resonance is arguably the more important of the two resonances, with the reference resonance only necessary when the sensor resonance becomes undetectable, the sensor resonance should be made the lower resonant frequency. In this way, the maximum signal is returned from the sensor resonance at all times. Once the sensor resonance is completely damped the reference resonance signal strength increases. In the ideal case, this would mean that the sensing circuit, and therefore the pseudoQ, would be unaffected by the addition of the reference circuit.

The curve fitting routine discussed in Section 4.2 is readily modified to deal with two resonances. The initial baseline fit is done in the same manner as originally described. At this point, the data is partitioned into two components, one window containing the lower resonance and one containing the higher resonance.

Each resonance is then fit individually with the Lorentzian lineshape. Once the individual baseline and resonance fits are complete, the coefficients are used as the starting point for a final fit of all three curves combined.

The algorithm then attempts to ensure that two separate peaks were found. Although the two resonances are initially fit individually, if only one resonance is actually present during the final fit it is possible to find a solution that is a sum of the two Lorentzians centered near the one actual resonance. The solution may appear to be a good fit of the data based on the sum of squares error; however, neither Lorentzian will be an accurate representation of the resonance and the coefficients used to estimate pseudoQ will be meaningless. This situation is detected by examining the center frequency of each phase dip. If either center frequency is outside of an $\omega_0 \pm 25\%$ window around the expected resonant frequency, then a single resonance curve fit is performed using the original algorithm described above.

Using this updated curve fitting routine, it is possible to see how the presence of the reference resonance affects the relationship between the sensor transducer resistance and pseudoQ in the real-world circuit model. The modeling was done with a reader coil with a 3 cm radius and 5 turns of 18 AWG copper wire, a sensor coil with a 3 cm radius and 5 turns of 18 AWG copper wire, and a reference coil with a 2 cm radius and 5 turns of 18 AWG copper wire. The sensor and reference coil are coaxial and coplanar with a reader to sensor separation of 5 cm. The full circuit model shown in Figure 4.7 was used for the impedance calculations. The sensor was simulated both with and without a reference coil and the results are shown in Figure 4.9. The presence of the reference circuit does change the value of pseudoQ, but this effect is small. The change in pseudoQ ranged between three and four percent over the range of transducer resistances simulated.

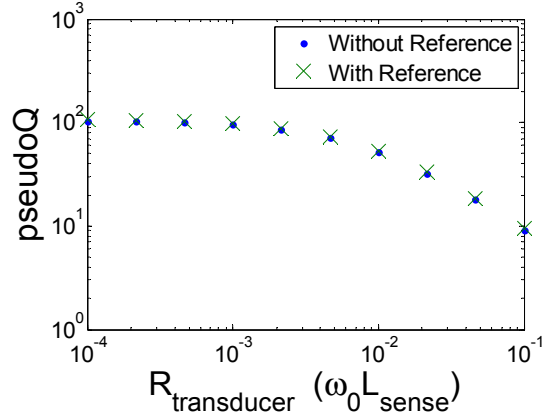


Figure 4.9 In the non-ideal circuit, the presence of the reference circuit affects the pseudoQ of the sensor circuit, however, this effect is small.

4.3.2 Next Generation Prototype

The proposed changes of removing the second capacitor in the sensing circuit and adding a separate reference circuit were built into a second generation prototype sensor. Several different configurations of the sensor were tested before settling on the design that is currently in use. Three different arrangements of the sense and reference coils were tested along with various potting compounds used to protect the sensor from the environment [21, 28].

The first coil arrangement tested consisted of two coaxial coils of the same diameter stacked on top of each other. Although this design worked, the spacing between the two coils meant that one coil was always farther away from the reader coil, resulting in a weaker signal. While pseudoQ was chosen as a measurand due to its relative immunity to changes in the coupling factor, the depth of the phase dip, and therefore the read distance, is still strongly dependent on coupling. This design also increased the height of the sensor to accommodate the height of two coils plus the space between them.

Another configuration consisted of two coplanar coils placed side-by-side. An advantage of this design is that it decreased the coupling between the sense and reference coils. However, it also required taking two measurements of each sensor with the reader coil positioned over each tag coil for maximum coupling. Another disadvantage of this design is that it is either necessary to double the width of the sensor or reduce the diameter of each coil to keep the overall sensor width the same as for a one-coil design. Although the sensors were not overly large, it was felt that the smallest form factor possible would be best as it would displace the least amount of concrete and therefore have minimal impact on the structure the sensor is embedded in.

The final design that was tested consisted of two coaxial coplanar coils. One coil is made smaller than the other and placed inside the larger coil as pictured in Figure 4.10. This is the smallest of the three designs as it takes up the same amount of space as a single coil. The current prototype sensors are fabricated using this concentric-coil design.

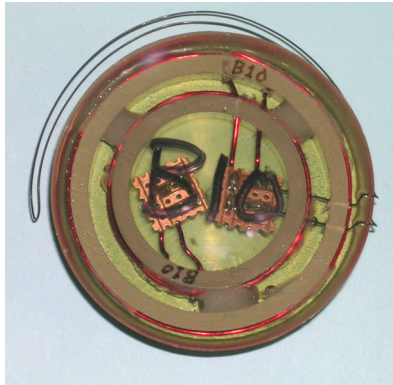


Figure 4.10 Second generation prototype corrosion sensor using concentric sense and reference inductor coils.

One disadvantage of this design is that one of the coils is smaller than the other and therefore has lower coupling to the reader coil. In this regard, it is better to make the sense coil the outermost coil as it is more important to be able to measure a strong signal from the sense circuit rather than the reference circuit.

Both computer simulations and laboratory measurements were used to select the components and coil geometries used in the current prototype sensors [26, 28]. Ultimately the objective is to provide the deepest phase dip in the measured reader coil impedance possible.

In general, the tag coils should be made as large as possible to maximize coupling. Currently, the sense coil is limited to a radius of 3 cm and a length of approximately 6 mm. These dimensions were chosen partially through experimentation with various coil designs as well as the desire to keep the overall sensor size relatively small so as to produce as little impact as possible on the structure the sensor is embedded in. The reference coil is sized such that it is easy to fabricate and readily fits inside of the sense coil. A radius of 2 cm is used for the reference coil. The coils are wound using 5 turns of 18 AWG copper magnet wire. The analysis presented in Section 4.1.2 suggests that this design could potentially be improved in future prototypes by using a single turn of a larger conductor. This could be realized by using copper tape or pipe cut to the appropriate dimensions, taking care to ensure that the thickness of the conductor is at least one skin-depth.

Ceramic disk capacitors are used to build the resonant circuits because they are inexpensive and robust. Through experimentation, it was found that not all ceramic capacitors behave equally [28]. Specifically, some capacitors produced sharper resonances, i.e. deeper phase dips and higher pseudoQs, than others. This effect is believed to be due to the lossy nature of some dielectrics used in the fabrication of capacitors and led to the specification of using capacitors with high-quality COG or NP0 dielectrics. This is consistent with the analysis in Section 4.1.2 that suggested increasing $\tan \delta$ decreases the overall Q_0 of the tag.

The values of the capacitance used in the sensors were based in part on the desire to set the resonant frequency of the circuits high enough to be in the region where $\omega L_{\text{reader}} \gg R_{\text{readercoil}}$. As discussed previously, increasing the operating frequency also increases the intrinsic Q of the tag circuit. However, the resonant frequency must also be kept low enough to be below the self resonance of both the reader and tag coils. Ultimately, the selection of capacitance values was based on what was readily available and inexpensive. Capacitors of 33 and 6.8 nF are used in the sense and reference circuits, respectively. The specifications of the sense and reference resonant circuits are listed in the Table 4.1. The values of L listed in the table were computed using Equation (4.1).

Table 4.1 Current sensor design parameters.

Sense		Reference	
Turns	5	Turns	5
Radius	3 cm	Radius	2 cm
L	3.2 μH	L	1.9 μH
C	33 nF	C	6.8 nF

Given the parameters of the sensing circuit, it is possible to estimate the desired characteristics of the transducer using the guidelines developed in Chapter 3. Based on the guideline that $3R_{\text{tagcoil}} \leq R_{\text{transducer}} \leq \omega_0 L_{\text{tag}}$, the resistance of the steel wire transducer should be between approximately 35 m Ω and 9.85 Ω . The transducer wire for the current prototype sensors is cut to a length of 10 inches or 25.4 cm. Combined with the conductivity of the wire, this information can be used to estimate the appropriate radius of the sensing wire. The conductivity of the wire is approximated using $\sigma_{\text{iron}} = 1.03 \times 10^7$ mohs/m. This yields a range of 4.73×10^{-4} to 2.82×10^{-5} meters for the radius of the sensing wire. In practice, 21 gauge wire is used for the steel sensing wire, which has a radius of 3.6×10^{-4} m, which falls near

the upper bound on the desired wire resistance. This allows the wire to corrode and still remain within the desired range.

Once the geometry of the sense coil is known, the affects of the reader coil geometry can be considered. The coupling from the reader to the tag is dependent on the amount of flux generated by the reader that links the area defined by the tag coil. For a given tag coil radius and reader to tag distance, there is an optimum reader coil size which maximizes the amount of flux coupling. If the reader is smaller than the optimum coil size, part of the tag coil area is “wasted” and receives little flux. On the other hand, if the reader is bigger than the optimum radius then part of the reader flux is wasted as it does not intersect the tag coil. Ultimately, the read range is dependent on the depth of the phase dip. Figure 4.11 shows a plot of phase dip versus reader coil radius for two different reader to tag distances.

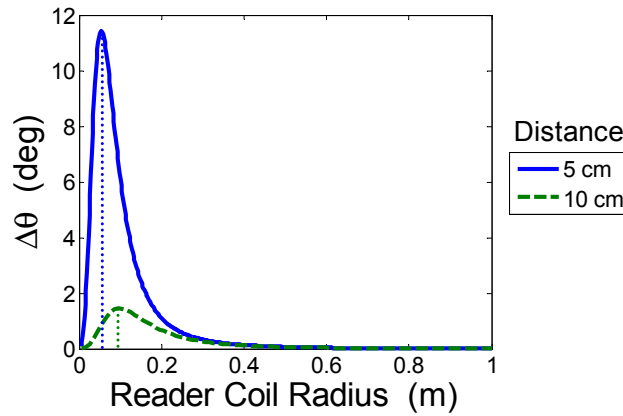


Figure 4.11 The reader coil radius that produces the largest phase dip is dependent on the spacing between the reader and tag.

As the tag is moved farther from the reader, the optimum reader coil size increases. However, even at the optimum reader size, the coupling, and thus the depth of the phase dip, is less than the phase dip when the reader and tag are close

together. Several different coils have been used to interrogate the prototype sensors. The most frequently used reader coil has a radius of 5.25 cm and 5 turns of 18 AWG magnet wire.

4.3.3 Concrete Tests

Similar to the original prototype sensors, the dual-resonance sensors were tested in two concrete slabs which were subjected to accelerated corrosion through the use of salt water ponds. Unlike the original slab tests, this concrete did not include large quantities of air-entraining admixtures, providing an environment closer to what could be encountered in the real world. In addition to casting sensors in slabs designed to simulate sections of a bridge deck, several sensors were also cast in concrete prisms which could be easily subjected to a variety of environmental conditions [28, 29].

The sensors were interrogated approximately every two weeks over a period of about one-and-a-half years. During this time, several of the sensors eventually indicated that the steel wire had broken. Figure 4.12 shows a contour plot of the raw phase data for one sensor over time. The main features of interest in the plot are the two regions corresponding to the sense and reference phase dips at 490 kHz and 1.4 MHz respectively. These values agree very well with the values calculated using the circuit parameters listed in Table 4.1. Around day 285, the phase dip corresponding to the sense resonance disappears and the reference resonance becomes much deeper – consistent with the behavior of a sensor whose sensing wire has broken.

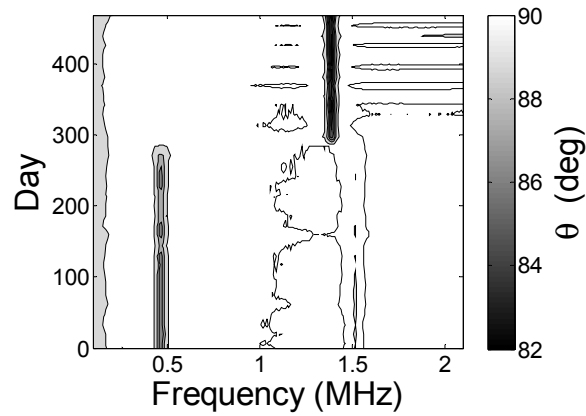


Figure 4.12 Contour plot showing the phase data vs. time of a sensor embedded in concrete. The sensor wire breaks around day 285 causing the sense phase dip to disappear and the reference phase dip to become much stronger.

The pseudoQ extracted from this data again shows that the sensing wire broke around day 285 as the sensor pseudoQ drops to zero at this point. In the time leading up to the wire actually breaking there is a clear decline in the pseudoQ indicating that the wire is corroding and therefore increasing in resistance.

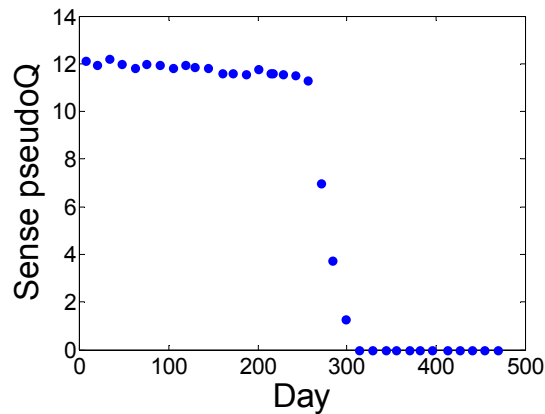


Figure 4.13 A plot of pseudoQ vs. time for a sensor embedded in concrete shows a relatively quick transition from an intact to a broken sensing wire.

Monitoring the corrosion sensors over time for changes in the pseudoQ may allow estimation of the corrosion rate. However, the transition from the original intact sensing wire to the broken wire occurred over a period of approximately 8 weeks. In a real-world structure it is possible that these sensors will be monitored infrequently, on the order of months or years between inspections. If the rate at which the test sensors transitioned from intact to broken steel sensing wires is indicative of the behavior to be expected in the real world, it would seem unlikely that the sensor would be inspected during this short period of time.

Once a large number of the sensors indicated that the sensing wire had broken, the concrete slabs were autopsied to examine the state of the steel reinforcement. There was a strong correlation between sensors that had broken and corrosion of the steel reinforcement in the area surrounding the sensor. Figure 4.14 illustrates the process of removing the concrete cover over the sensors and an example of reinforcement corrosion near a sensor.



Figure 4.14 Autopsies of the test slabs (left) revealed that there was a correlation between sensors with broken sensing wires and reinforcement corrosion (right).

The data from these tests and from other sensors which are currently embedded in another set of test slabs indicate that while more work may be necessary to be able to use the sensors to determine the corrosion rate, the current design is useful as a threshold sensor. As mentioned in Chapter 3, the gauge of the steel sensing wire can be tailored to adjust the amount of corrosion necessary to trigger the sensor.

The autopsies of the slabs and concrete prisms also revealed that the steel sensing wire and the surrounding reinforcement were often only corroded in isolated spots rather than uniformly along the length of the wire or over a wide area of rebar. This corrosion seemed to occur predominantly in regions where the concrete contained cracks formed from the loading of the slabs. This may help to explain the rapid change in the sensor pseudoQ seen in Figure 4.13 as only a small region of the wire corroding would have a much smaller effect on the wire resistance than if the entire wire had corroded evenly.

The analysis of the data returned from the slab experiment revealed several unexpected results which are all depicted in Figure 4.15.

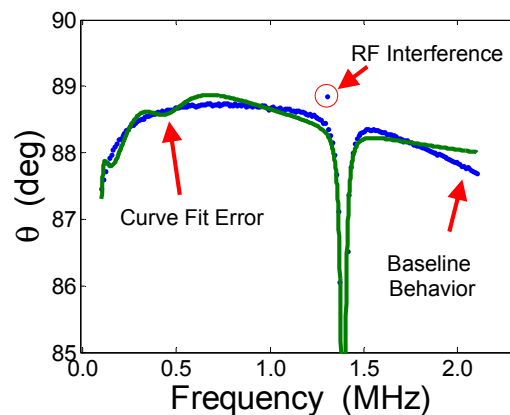


Figure 4.15 A depiction of several unexpected behaviors encountered during field testing of the corrosion sensors.

The first unexpected result was the repeated detection of what appeared to be an error in measuring the phase of the impedance in a very narrow band around 1.3 MHz. The fact that this error only occurred at one frequency point and always at the same frequency suggested a resonant phenomenon. Further investigation revealed that the transmitting tower for KVET AM, “The Longhorn Station,” which broadcasts at 1300 kHz, is located less than a mile from where the sensor tests were conducted. The fact that the measurement is susceptible to RF interference is not surprising, but it is an important fact to keep in mind when developing such a system. This particular interferer was easily filtered out during data analysis.

The second observation was that the current curve fitting routine does not always properly detect when there is only one resonance and may try to fit two Lorentzians to a data set containing only one phase dip. The example shown in Figure 4.15 demonstrates how this can lead to a poor fit and potentially incorrect values for pseudoQ. It is possible to go back and detect these cases manually by viewing the measured phase response and verifying that there is in fact only one resonance. The data can then be fit using the single resonance fitting routine. However, a truly automated sensor system which is simple to operate in the field and requires as little user intervention as possible will require improvements to the curve fitting routine.

Finally, the measured phase shown in Figure 4.15 shows a very strong droop in the baseline behavior at the high end of the frequency sweep. This behavior cannot be readily explained using the current circuit model and this is one of the reasons that the data is fit using lineshapes rather than attempting to fit the actual circuit model to the data. Investigations of the baseline drift have shown that it occurs whether a tag is present or not and that it is a time-dependent behavior, that is the baseline deviation will come and go as measurements are taken throughout the day. Also, the problem only occurs sporadically, complicating attempts to identify the cause. Steps are being taken to allow the measurement of a known reference

load without changing the connections of the measurement equipment to the reader in an attempt to isolate the source of this behavior.

4.3.4 Potential Improvements

Although the current prototypes performed well as threshold sensors in the last set of tests, there are several possible improvements which are being investigated. Of major concern is the ability to detect corrosion occurring over a wide area rather than only where the sensor is located. Although the exact mechanisms of corrosion in concrete are not completely understood, it is believed that one of the predominant driving forces is the creation of macrocells within the concrete slab. In a corrosion macrocell, the top and bottom rebar cages act as the anode and cathode of an electrolytic cell, with the concrete and its associated pore solution acting as the electrolyte. When a current pathway exists between the two layers of reinforcement, the entire reinforcing grid is subjected to the reduction-oxidation reaction, causing corrosion of the anode. If the steel wire of the corrosion sensor were made a part of the anode, then it would potentially corrode along with a large area of the reinforcement.

This concept is currently being tested in a new set of concrete slabs cast in March 2006. The steel sensing wire of each sensor was connected to the top layer of reinforcement by simply zip-tying the wire loop to the rebar, as shown in Figure 4.16.

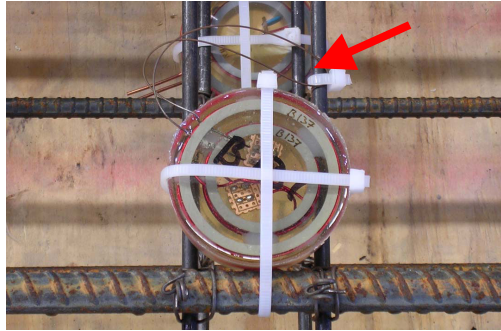


Figure 4.16 The steel sensing wire has been connected to the rebar to attempt to make it part of the larger electrochemical corrosion macrocell.

One possibility for providing a better electrical connection to the reinforcement is pictured in Figure 4.17. A second non-corroding wire extending outside of the sealed portion of the sensor would be used to make the electrical connection and could simply be wrapped around the reinforcing steel several times, making installation rather simple. An inductor could be included inside the sensor as an RF choke to attempt to isolate the circuit from potential high frequency interference due to being connected to the reinforcing grid while still providing the DC connection necessary to make the sensor a part of the corrosion macrocell.

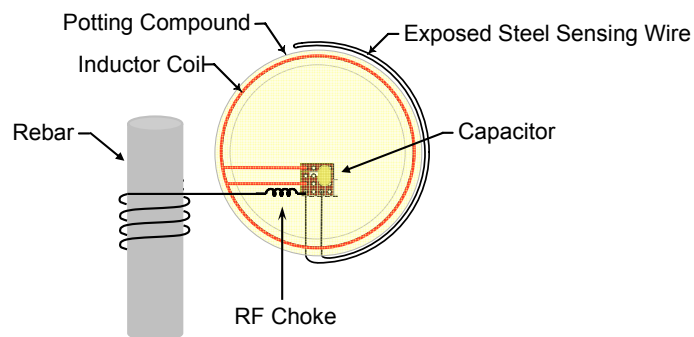


Figure 4.17 A second external wire connected via an RF choke may provide a better DC connection to the rebar.

The macrocell concept could be expanded further by making the sensing wire out of a sacrificial material such as zinc. As zinc is more electronegative than steel, it creates an electrochemical cell where the zinc is the anode and the steel is the cathode. In this state, the zinc will corrode while protecting the steel. This behavior is widely exploited in cathodic protection systems used in marine environments. Because the zinc in such a system tends to corrode before the steel begins to corrode, the sensor could potentially provide a warning that corrosive conditions exist before the steel actually begins to corrode. Investigations are currently underway to evaluate the viability and effectiveness of different sensing wire materials [30].

CHAPTER 5

Conductivity Sensor

5.1 CONCRETE RESISTIVITY

Steel in concrete naturally develops a passive oxidation layer due to the alkaline environment. This passivation layer helps to protect the steel from further corrosion. When the environment of the concrete changes, for example through the introduction of chloride ions, as is common when the concrete is exposed to marine spray or de-icing salts, this passivation layer can break down and allow corrosion to occur. If these changes in the environment could be detected through the use of an embedded sensor, it may be possible to take remedial action on the structure before significant corrosion occurs.

Other research has shown that once the passivation layer of the steel has been broken down, the resistivity of the concrete can affect if and at what rate corrosion actually occurs. One measure of the corrosion rate is the corrosion current density which is derived from linear polarization measurements at the surface of the concrete. Figure 5.1 shows a correlation between the corrosion current density and the concrete resistivity measured using a four-point Wenner probe.

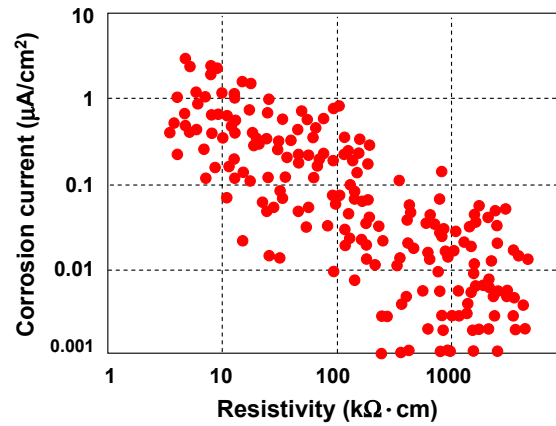


Figure 5.1 There is a correlation between the corrosion rate as measured by the corrosion current and concrete resistivity [31].

Unfortunately, although there appears to be a correlation between the corrosion current density and concrete resistivity, there is not a consensus on what constitutes an acceptable value of resistivity. Table 5.1 shows an example of resistivity versus corrosion from two different studies. Some of this uncertainty comes from the difficulties in making the resistivity measurements in the first place. This can in part be attributed to the inhomogeneous nature of the material itself as well as the lack of a standard measurement technique.

Table 5.1 There not a consensus on what values of concrete resistivity are associated with what level of corrosion risk [31].

Reference	Resistivity (k Ω ·cm)	Corrosion Risk
Feliu 1996	>100-200	Negligible corrosion; concrete is too dry
	50-100	Low corrosion rate
	10-50	Moderate to high rate when steel is active
	<10	Resistivity does not control corrosion rate
Bungey 1989	>20	Low
	10-20	Low/moderate
	5-10	High
	<5	Very high

The above information provides motivation for developing a wireless conductivity/resistivity sensor which can be embedded in concrete. Such a sensor may be able to detect elevated chloride ion levels due to the increase in available charge carriers. There is also evidence that the resistivity of the concrete may be directly related to the rate at which corrosion can occur. Finally, the availability of an embeddable conductivity sensor may allow better and more repeatable measurements of concrete resistivity which in turn would help clarify the relationship between resistivity and corrosion rate.

A simple conductivity sensor can be created by replacing the steel wire of the prototype corrosion sensor with two separate electrodes. These electrodes are exposed to the medium which is to be measured, in this case, the concrete. However, it is clear from the data in Table 5.1 that the resistivity of concrete is fairly high and therefore the resistance of the conductivity probe would be expected to be high as well. Such a large resistance would be impractical for use with the current circuit design.

5.2 MODIFIED CIRCUIT TOPOLOGY

In the circuits discussed earlier the transducer resistance was placed in series with the capacitor and inductor. In order to produce a detectable change in the reader coil impedance, the transducer resistance must be fairly low. Unfortunately, this requirement is incompatible with the high impedances expected when attempting to measure the relatively high resistivity concrete. This limitation can be overcome, however, by modifying the circuit topology. Figure 5.2 shows the transducer placed in parallel with the capacitor of the circuit rather than in series. When dealing with elements in parallel it is often easier to work with the admittance of the elements, which in this case would be the conductance of the probe, denoted G .

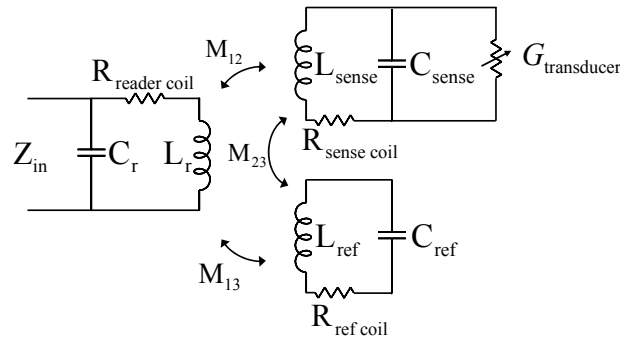


Figure 5.2 Modified circuit topology with the transducer in parallel with C_{sense} to allow the use of high-impedance transducers.

The normalized circuit model used in Chapter 3 was modified to place the transducer in parallel with the tag capacitor. This allows a quick check to determine how the previously developed guidelines might be applied to the new circuit configuration. In this case, the circuit is simulated for a range of transducer conductances which are normalized to $\omega_0 C_{tag}$, the admittance of the tag capacitor on

resonance. The simulation was performed with two different parasitic tag coil resistances. The results are shown in Figure 5.3.

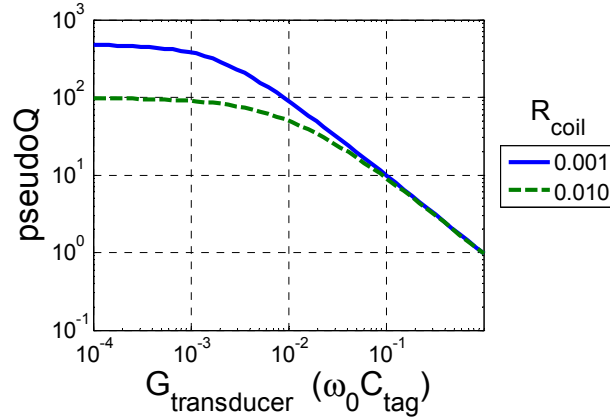


Figure 5.3 The pseudoQ of the parallel circuit configuration is a strong function of $G_{\text{transducer}}^{-1}$.

The pseudoQ of the circuit shows the same dependence on $G_{\text{transducer}}$ as the original circuit showed for $R_{\text{transducer}}$. The original design guidelines developed in Chapter 3 can be applied to the new circuit topology by substituting the transducer conductance as compared to $\omega_0 C_{\text{tag}}$ for the original transducer resistance as compared to $\omega_0 L_{\text{tag}}$.

5.3 PROTOTYPE SENSOR

A prototype sensor was designed and built to test the concepts described above. The conductivity probe of the sensor was built using a simple configuration of two parallel wires. This design was chosen both for its ease of fabrication as well as the ability to approximate the impedance between the two wires with relatively simple approximations. The impedance of the probe can be computed as a function of wire size and spacing as well as the material properties of the surrounding

medium. Figure 5.4 provides an illustration of these parameters where σ_m , ϵ_m , μ_m are the conductivity, permittivity, and permeability of the medium.

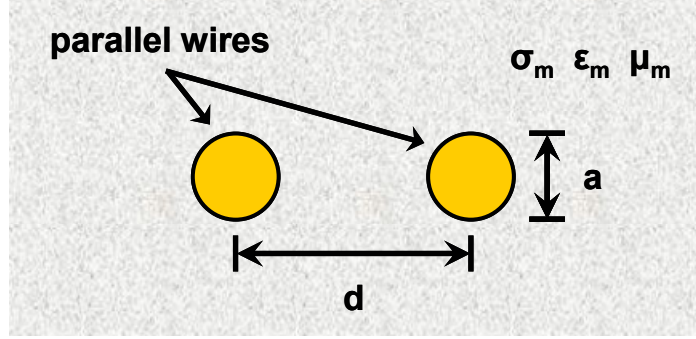


Figure 5.4 Arrangement of a simple two-wire conductivity probe.

The expression for the impedance between two parallel wires is classically derived by starting with two infinite line charges and relating them to two cylindrical conductors that match equipotential surfaces of the original line charges [32]. From this derivation, the capacitance per length is given as

$$\frac{C}{\ell} = \frac{\pi \cdot \epsilon_m}{\cosh^{-1}(d/a)}. \quad (5.1)$$

Similarly, the conductance per unit length is

$$\frac{G}{\ell} = \frac{\pi \cdot \sigma_m}{\cosh^{-1}(d/a)}. \quad (5.2)$$

A quick check was done to test the validity of these approximations for the conductivity probe. Two pieces of 18 AWG copper wire with a spacing of 5 mm

and a length of 37 mm were soldered to a standard RCA connector. This probe was then immersed in tap water and the impedance between the two wires was measured using an HP 4194A Impedance Analyzer between 100 kHz and 2.1 MHz, the same frequency range used for the wireless corrosion sensor. The built-in circuit parameter extraction capability of the 4194A was used to extract the capacitance of the probe and this was compared against the value calculated using Equation (5.1). A value of $\epsilon_m = \epsilon_0 \cdot 80$ was used for the calculations, where 80 is the approximate relative permittivity of water. The measurement data produced a value of 36.9 pF while the computed value was 36.3 pF – less than a two percent difference, suggesting that the approximation is reasonable at these dimensions.

The wide range of possible concrete resistivities, both from the table above and other resources, leave wide margins for the design of the prototype concrete conductivity probe [33-35]. Initial calculations suggested a probe conductance of 1 mS at a material resistivity of 10 k Ω ·cm would produce a reasonable design.

The wire chosen to construct the probe was 14 AWG copper wire commonly used in household wiring. This wire was chosen because it is relatively stiff and would keep its shape better than smaller wire, but was still simple to integrate with the current sensor geometry and the copper PC boards currently used to assemble the sensors. Based on (5.2), the length of the probe increases as the ratio of the wire spacing to the wire diameter grows. In order to keep the length of the probe short, this ratio should be small. An initial spacing of twice the wire diameter would give a separation of 3.3 mm for 14 AWG wire. For practical purposes the spacing was rounded up to 4 mm. Given these dimensions and the target conductance and resistivity values, it is possible to solve for the necessary length of the probe.

For the values cited above, the probe length should be approximately 5 cm. However, it was felt that a 5 cm probe length would increase the likelihood that the probe would be damaged during the placement of concrete. For this reason, the probe was shortened to 3 cm. Shortening the probe length has the effect of shifting

the target resistivity to approximately 6 k Ω ·cm. Given the wide range of possible concrete resistivities, this is still an acceptable value.

Eleven prototype conductivity sensors were fabricated for testing purposes using the probe geometry discussed above. In addition to the wireless conductivity sensors, wired probes with identical geometries were also constructed. The wired probes allow direct connection to the 4194A. Both the wireless conductivity sensor and wired conductivity probe are pictured in Figure 5.5.

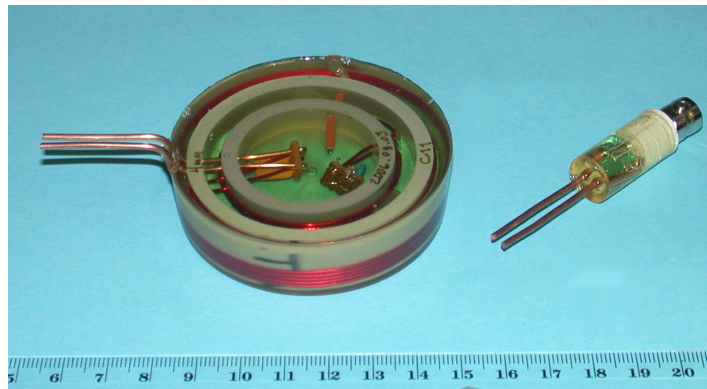


Figure 5.5 Prototype wireless conductivity sensor and matching wired reference probe.

After fabrication, nine of the conductivity sensors were immediately placed in concrete slabs which were being cast to test a new batch of corrosion sensors. Another sensor was simultaneously tested in varying concentrations of salt water. Testing the sensors in salt water provided a simple method of examining the performance of the sensor in an environment with varying conductivity.

5.4 SALT WATER TESTS

The sensor was tested by attaching a reader coil to the bottom of a 5 gallon plastic bucket. The bucket was then filled with tap water and the conductivity

sensor was placed inside the bucket and aligned with the external reader coil. The 4194A was used to measure the input impedance of the reader coil between 100 kHz and 2.1 MHz. This data was then analyzed using the curve fitting routine previously discussed. The impedance of the wired conductivity probe pictured in Figure 5.5 was also measured and recorded over the same frequency range. The effects of the cabling used to connect the probe to the impedance analyzer were minimized using an open-short calibration procedure.

In addition to recording the wired probe and wireless sensor response, a commercial conductivity meter was used to measure the conductivity of the water. The meter measured a conductivity of 290 $\mu\text{S}/\text{cm}$ at 23.2°C for the tap water. The City of Austin water quality reports at the time listed a conductivity of 301 $\mu\text{S}/\text{cm}$, suggesting the meter was reporting reasonably accurate values [36].

The conductivity of the water was increased incrementally by adding small amounts of a saturated solution of tap water and table salt (NaCl) to the bucket containing the sensor. This was done in an attempt to minimize the possibility of undissolved salt in the water. Overall, the conductivity of the water used in the tests ranged from 290 $\mu\text{S}/\text{cm}$ to 11.7 mS/cm. Figure 5.6 shows the phase data taken from the reader coil impedance measurements for two different water conductivities. The sense resonance clearly shows a change in the response due to the change in the conductivity.

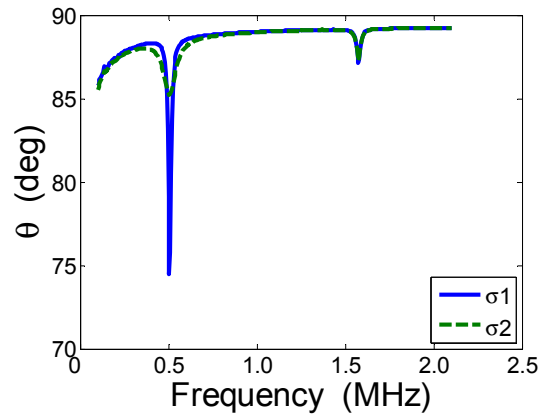


Figure 5.6 The phase of the impedance response of the conductivity sensor is clearly affected by the change in the conductivity of the salt water.

The wireless sensor data was then processed using the curve fitting algorithm to extract pseudoQ. Figure 5.7 shows pseudoQ ranged from approximately 30 to 1 as the conductivity of the water was increased.

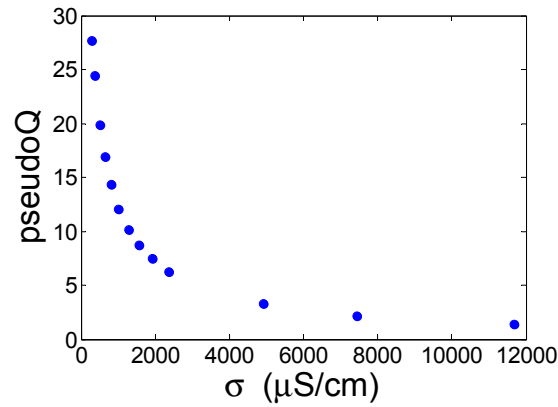


Figure 5.7 As expected, the pseudoQ of the sense circuit is dependent on the conductivity of the salt water.

The analysis can be taken one step further by attempting to estimate the conductivity of the medium based on the measured data and the probe geometry. In addition to interrogating the sensor in the water, an initial measurement was made with the sensor in air. As air is a relatively good insulator, this is a method of approximating the intrinsic Q of the sensor. For the particular sensor used in this test, the pseudoQ in air (\bar{Q}_{air}) was approximately 64. Based on the guidelines presented in Chapter 3, this would suggest the optimum operating range would be a pseudoQ between 1 and 16. However, as mentioned previously and as shown in Figure 5.7, a pseudoQ of approximately 30 was measured with the sensor in tap water. The pseudoQ does not fall below 16 until a water conductivity of about 800 $\mu\text{S}/\text{cm}$ is reached.

Although the data for conductivities below 800 $\mu\text{S}/\text{cm}$ does not fall into the optimum operating range, it may still be possible to use the data to estimate the water conductivity. Similar to the discussion in Chapter 4 of how Q_0 is a function of the coil Q and the capacitor Q, the total Q of the circuit is due to the intrinsic losses of the circuit as well as the losses induced by the medium through the conductivity probe:

$$Q_{total} = \left[\frac{1}{Q_0} + \frac{1}{Q_{medium}} \right]^{-1}. \quad (5.3)$$

As already mentioned, Q_0 can be estimated by measuring the response of the sensor in air. Replacing Q with pseudoQ (\bar{Q}) and solving (5.3) for Q_{medium} , the conductance of the probe can be estimated as

$$G_{probe} \approx \frac{\omega_{\theta\min} C_{tag}}{\bar{Q}_{medium}} = \omega_{\theta\min} C_{tag} \left[\frac{1}{\bar{Q}_{total}} - \frac{1}{\bar{Q}_{air}} \right]^{-1}. \quad (5.4)$$

Substituting the results from (5.4) into (5.2), it is possible to calculate a value for the medium conductivity based on the measured pseudoQ:

$$\sigma_m = \frac{G_{probe} \cdot \cosh^{-1}\left(\frac{d}{a}\right)}{\ell \pi} = \frac{\omega_{\theta \min} C_{tag}}{\bar{Q}_{medium}} \frac{\cosh^{-1}\left(\frac{d}{a}\right)}{\ell \pi}. \quad (5.5)$$

As a cross-check, the conductance of the wired probe can also be extracted from the measured data using a simple G parallel C model and the conductivity of the medium can be estimated based on this data as well. The conductance of the wired probe used to estimate the conductivity was extracted at $\omega_{\theta \min}$ in an attempt to compare measurements at similar frequencies.

It is instructive to compare the resistive and reactive components of the wired probe impedance, that is ωC_{probe} compared to G_{probe} , to determine if the probe truly appears as a shunt conductance in the circuit rather than an additional capacitance. The ratio of $G/\omega C$, which as mentioned previously is equal to the loss tangent of the capacitor, ranged from approximately 15,000 to 33,000 over the range of conductivities tested. Therefore, the probe can safely be considered as a conductance in parallel with the tag capacitor.

Figure 5.8 shows the extracted conductivity from both the wired and wireless sensors plotted against the value measured using the conductivity meter. For reference, a line indicating the meter reading has also been added to the plot.

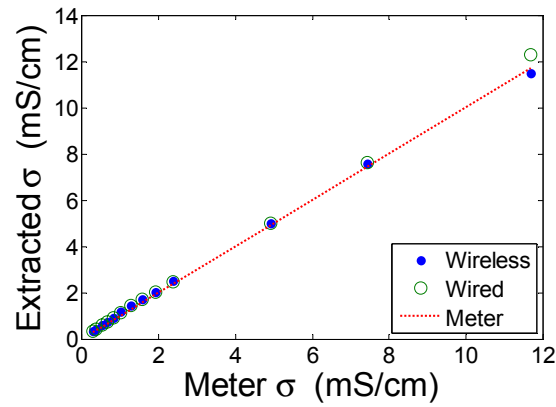


Figure 5.8 Both the wired and wireless conductivity sensors agree quite well with the commercial conductivity meter.

The two parallel wire probes agree fairly well with the commercial meter reading. The average error between both the wired and wireless probes and the meter reading is approximately 10% and the error decreased with increasing conductivity. The wireless sensor had an error of 22% at the lowest conductivity, 290 $\mu\text{S}/\text{cm}$, and an error of 2% at the highest conductivity, 11.7 mS/cm. The wired and wireless probes also agreed well with each other. The wireless probe had an average deviation from the wired probe of 1.3%.

The fact that the responses from the wired and wireless probes agree quite well suggests that the wireless measurement method works well; however, there is clearly some error in measuring the conductivity with the current probe design and data extraction techniques. As mentioned previously, there was an approximate 3.7% difference between the meter reader and the water quality reports for the conductivity of tap water. It is possible that there was some error in the commercial meter calibration which would contribute to the difference between the meter and the experimental probes.

A second potential source of error could come from relating the geometry of the probe to the conductance. The equation given in (5.2) was derived for infinite length wires. Truncating the wires to a finite length will introduce some error due to the fringing fields present at the ends of the probe. However, the comparison of the calculated and measured capacitance of the probe in tap water suggests that the error due to this approximation is relatively small.

It is also possible that the error between the experimental probe and the commercial meter is caused by frequency dependencies in the measurements. Sources of frequency dependence include possible frequency dependent material parameters, including conductivity and permittivity, as well as electrode-electrolyte interface effects. Although frequency dependent material parameters are possible, the frequency dependence of electrode impedance is most often attributed to effects from the electrode-electrolyte interface. At the electrode-electrolyte interface, metal ions enter into solution and ions from the electrolyte combine with the electrode. Due to these potentially complex chemical reactions, a net charge distribution or electric double layer forms at the electrode surface [37]. This charge distribution is the source of the familiar half-cell potential and also creates a frequency dependent capacitance coupling the electrode to the electrolyte.

Since both electrodes in the prototype conductivity probe are made of the same material and are immersed in the same electrolyte, they will be at the same potential. Therefore the electrode potential can be safely ignored. The impedance of the electrode-electrolyte interface is often modeled as either a series or parallel combination of a capacitor and resistor. Both models have their advantages and drawbacks and neither is a perfect representation of the behavior at all frequencies [37].

It is also possible that there is additional connector impedance which has not properly accounted for in the open/short calibration procedure. Several attempts were made at estimating the potential electrode and connector effects. The

estimated impedance of the medium was calculated using (5.1) and (5.2) combined in a parallel GC model. This impedance was subtracted from the measured impedance and the result was fit with various circuit models. Several of the circuit models, including the classical electrode-impedance models, produced negative values for some of the circuit parameters. However, these results do not necessarily mean the classic models do not apply. The contributions of the electrode effects are expected to be small at the frequencies of measurement and are most likely much smaller than the associated cabling and connector impedances used to connect the probe to the measurement equipment. Any noise or errors in calibrating out these impedances could lead to errors in attempting to extract the electrode impedance. There are established procedures for calculating the electrode impedance for a given electrode-electrolyte combination; however, as these sensors are ultimately for use in concrete and not salt water, these measurements are left as possible future work [37].

One simple method of dealing with the error in calculating the medium conductivity from the sensor pseudoQ is to use the above measured data as a means to calibrate the sensor. The measured pseudoQ shows a strong σ_m^{-1} dependence and, rather than attempting to extract G from the pseudoQ and then estimating the conductivity based on the probe geometry, simple curve fitting techniques can be used to relate pseudoQ and σ_m .

The data was fit using the Matlab Curve Fitting toolbox with the following equation:

$$\sigma_m = \frac{a}{\overline{Q}_{total}} + c, \quad (5.6)$$

where a and c are the fitting parameters and have units of conductivity. The values for a and c along with their 95% confidence bounds are listed in Table 5.2.

Table 5.2 Curve fitting results for estimating σ_m based on the measured pseudoQ.

Parameter	Units	Value	95% Confidence Limits
a	(mS / cm)	16.62	(16.47, 16.77)
c	(mS / cm)	-0.3109	(-0.3494, -0.2725)

The measured data along with the resulting curve fit are plotted in Figure 5.9.

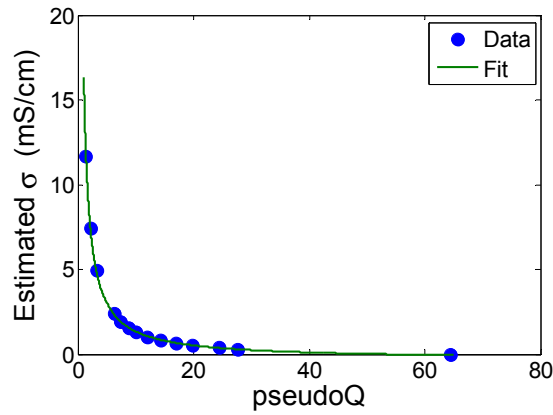


Figure 5.9 Curve fitting can be used to relate the measured pseudoQ of the conductivity sensor to the conductivity of the medium.

Figure 5.10 shows the measured data, the curve fit, and the 95% prediction bounds of the fit. The prediction bounds indicate that as the measured pseudoQ increases, approaching the intrinsic Q of the sensor, the prediction bounds become wider. This is to be expected given that as $\bar{Q}_{measured}$ approaches \bar{Q}_0 , small errors in $\bar{Q}_{measured}$ can cause large errors in the estimated \bar{Q}_{medium} . Note that the scale has been expanded from that of Figure 5.9 to show the prediction bounds more clearly.

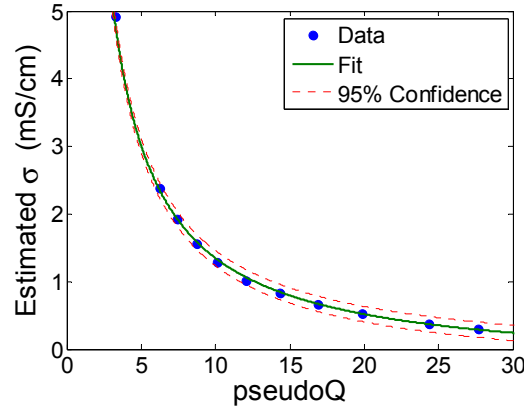


Figure 5.10 The prediction bounds of the fit grow wider as pseudoQ approaches the intrinsic Q of the sensor.

The original expression derived for relating σ_m and pseudoQ given in (5.5) has a similar form to (5.6). Inserting the dimensions of the probe, the value of the tag capacitance, and ω_0 for $\omega_{\theta\min}$ into (5.5) yields

$$\sigma_m = 16.69 \frac{1}{\bar{Q}_{medium}} \text{ (mmho/cm)}, \quad (5.7)$$

which is very similar to the results obtained with (5.6) and the Matlab Curve Fitting toolbox. This suggests that the assumptions and models used to derive (5.5) are reasonable.

The sensor works reasonably well given the constraints and possible sources of error discussed above. Although it may be possible to reduce some of these errors with further measurement and modeling, the sensor is ultimately intended for use in concrete and the interaction of the electrode-electrolyte interface will ultimately be different from that of salt water. The above analysis is simply intended to show that the wireless conductivity sensor performs reasonably well.

5.5 TESTS IN CONCRETE

As mentioned previously, in addition to testing the sensor in salt water, nine of the conductivity sensors were placed in concrete slabs which were being cast to test a new round of wireless corrosion sensors. Four conductivity sensors were placed in each of two test slabs. Three of the sensors in each slab were attached to the top layer of reinforcing steel, resulting in approximately one inch of concrete cover over the sensors in the completed slabs. One sensor was placed inside the salt water ponding area, one immediately outside the ponding area, and one far from the ponding area. The fourth sensor was attached to the lower layer of reinforcing steel at the bottom of the slab inside the ponding area. This was intended to help determine how quickly moisture and chloride ions penetrate through the slab. In addition to the two large test slabs, a small control slab was also cast. The control slab was designed to mimic a small section of the larger slabs and was subjected to the same environmental conditions, such as temperature and humidity, without being subjected to corrosion-accelerating measures such as salt water ponding. The ninth sensor was cast in the control slab, along with a wireless corrosion sensor.

The salt water ponds used to accelerate corrosion are alternately filled and emptied such that the slab is wet for two weeks and then dry for two weeks at a time. Measurements of all sensors in the slabs are made at the end of each two week period. Analysis of the data collected to date is presented in Figure 5.11. Table 5.3 lists the corresponding position of each sensor in the slabs.

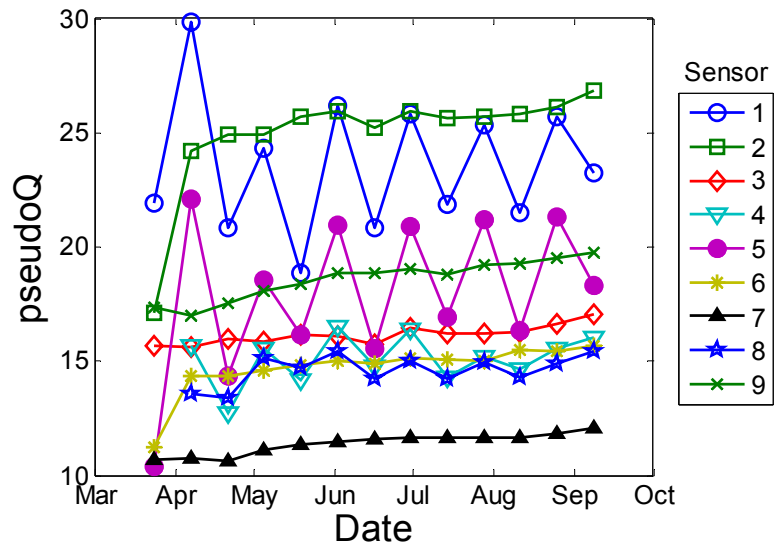


Figure 5.11 The pseudoQ of the conductivity sensors in the slab ponding area exhibit a periodic nature that coincides with the wet-dry cycle of the salt water pond.

Table 5.3 Conductivity sensor position with respect to salt water pond.

Sensor	Slab	Position
1	1	In ponding area, top of slab
2	1	Outside ponding area, top of slab
3	1	Far from ponding area, top of slab
4	1	In ponding area, bottom of slab
5	2	In ponding area, top of slab
6	2	Outside ponding area, top of slab
7	2	Far from ponding area, top of slab
8	2	In ponding area, bottom of slab
9	Control	No ponding

The pseudoQ of sensors 1 and 5 clearly indicate a cyclic pattern with a period of two weeks, corresponding to the wet and dry periods of the salt water ponds. The high values of pseudoQ correspond to the end of the two week dry period. The sensors outside of the ponding area and the sensor in the control slab do not show this behavior. This behavior suggests that the conductivity of the concrete is indeed changing in response to the presence of salt water.

Interestingly, the pseudoQs of sensors 4 and 8, which are at the bottom of the slab in the ponding area, also show periodic behavior corresponding to the wet and dry cycles, though the amplitude of the variation is smaller than for the sensors located at the top of the slab. This suggests that at least some of the moisture from the pond is penetrating through to the bottom of the slab.

While the changes in pseudoQ observed in the slab sensors matches the expected behavior of the sensor in a medium with changing conductivity, it is important to ensure the changes are caused through the sensor probe rather than through losses induced in the medium itself by the reader's magnetic field. An experiment was done in which a reader coil and sensor were fixed so that different materials could be placed between them. Three one inch thick cylinders of concrete were cast from the same batch of concrete used in the test slabs. Once cured, one cylinder was soaked in the salt water ponding solution, one cylinder was soaked in tap water, and one was left dry. After three weeks, the test sensor was interrogated with each of the three concrete cylinders in between the reader and sensor. Figure 5.12 shows the testing jig with a concrete sample between the reader and sensor.

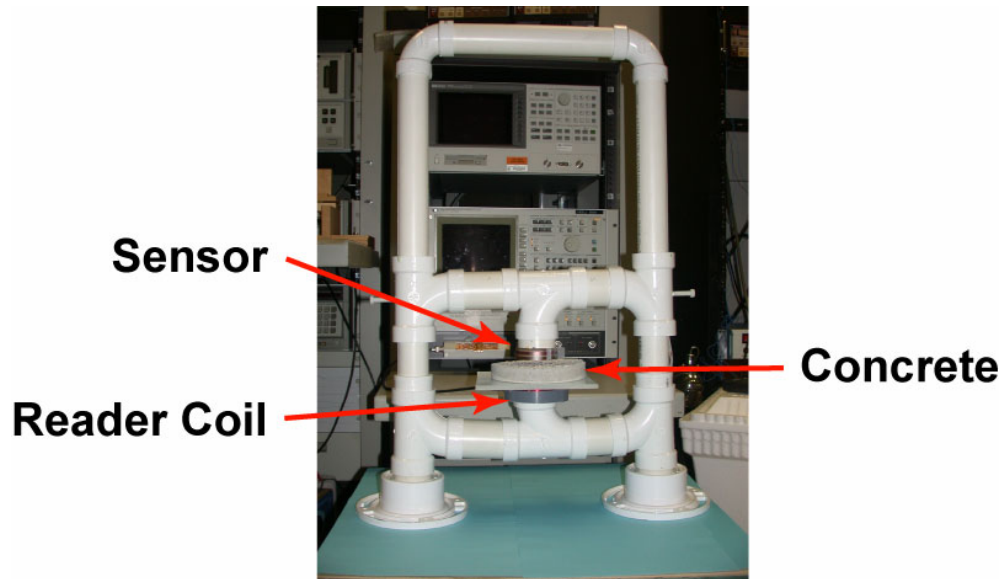


Figure 5.12 Test jig to allow substitution of the material between the reader and sensor without changing the reader and sensor alignment or spacing.

No appreciable changes were measured in the input impedance of the reader coil for all three samples, suggesting that the changes in pseudoQ observed in the sensors in the test slab were in fact caused by the interactions of the probe with the concrete rather than induction losses in the medium.

The sensors were all interrogated after fabrication and before placing the sensors in the test slabs. The sensors had an average pseudoQ_{air} of approximately 40. The sensors were then placed in the slab formwork and attached to the reinforcing steel. The sensors were interrogated again once they were attached to the steel reinforcement and before the concrete was placed. The pseudoQ_{air} measured with the sensors in place varied from approximately 12 to 28 – a change of 30-70% from the results measured in air with no rebar present. The presence of the rebar could potentially influence both the self-inductance of the sensor as well as the losses in the overall circuit due to eddy currents induced in the reinforcing steel. Both of these effects would affect the measured pseudoQ.

Thanks to the resonant nature of the sensor circuit, if the capacitance of the sensor is assumed to remain constant, the change in the inductance caused by the presence of the reinforcing steel can be estimated by examining the change in the resonant frequency. All nine sensors showed a shift in the resonant frequency of less than one percent when measured with the rebar present. This suggests that the inductance changed by less than two percent and therefore most of the change in pseudoQ is attributed to additional losses induced in the circuit due to the presence of the rebar.

Analysis of the data gathered after the concrete was placed, presented previously in Figure 5.11, shows that the measured pseudoQ is approximately equal to the intrinsic pseudoQ in the presence of the rebar. This suggests that once cured, the resistivity of the concrete combined with the geometry of the prototype conductivity probe result in a low probe conductance.

In some cases, the pseudoQ is higher after placing the concrete than when measured before casting the concrete. Rather than implying that the concrete has a lower conductivity than air, this suggests that there is potential error in the intrinsic pseudoQ measured before the concrete was placed. The large change between the intrinsic pseudoQ measured with and without the rebar present suggests that the intrinsic pseudoQ is very sensitive to the presence of the rebar. Therefore, small changes in the position of the sensor relative to the reinforcement may change the intrinsic pseudoQ. Movement of the sensor during the placement of the concrete could potentially account for the change in the intrinsic pseudoQ of the sensor. If the intrinsic pseudoQ increased as a result of sensor movement, it would be possible for the pseudoQ measured with the sensor in concrete to be higher than the original pseudoQ measured before placing the concrete.

Using the method expressed in (5.4) and (5.5) to remove the intrinsic losses of the circuit can result in a negative value for conductivity when the measured pseudoQ is higher than the previously measured intrinsic pseudoQ. Clearly, the

conductivity of the concrete cannot be negative; however, the data can still be used to view general trends in the conductivity. Figure 5.13 shows the calculated conductivity data for the nine sensors. The data has been shifted such that the lowest conductivity plotted is zero. While the plotted conductivity is not equal to the actual conductivity of the concrete, it does indicate that the conductivity of the sensors in the ponding areas fluctuates with the wet-dry cycles. The conductivity outside of the ponding area indicates that it is decreasing with time as would be expected as the concrete continues to cure.

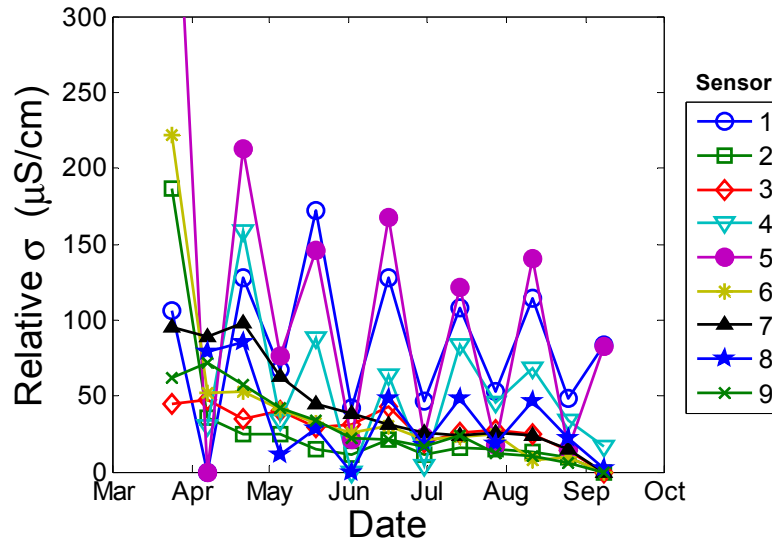


Figure 5.13 The relative conductivity extracted from the slab sensors shows a clear dependence on the salt water ponding cycle.

5.6 CURING TESTS

In addition to the tests in salt water and the long term tests in concrete, an experiment was conducted to monitor sensor behavior continuously as the concrete was curing. A test slab was constructed in the same manner as the control slab

mentioned previously which itself was designed to mimic a small section of the full-scale test slabs. The slab was outfitted with several sensors including one corrosion sensor, one conductivity sensor, and one wired conductivity probe which matched the probe used on the wireless sensor. Similar to the salt water tests conducted above, the wired probe was included as a means of cross-checking the data extracted from the wireless sensor. Figure 5.15 shows the sensors in place before casting the concrete and Figure 5.15 shows the final setup.

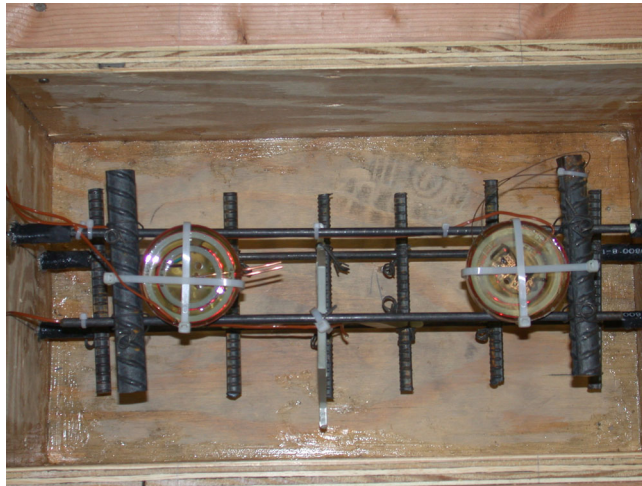


Figure 5.14 Conductivity (left) and corrosion sensor (right) in place in test slab before casting concrete.

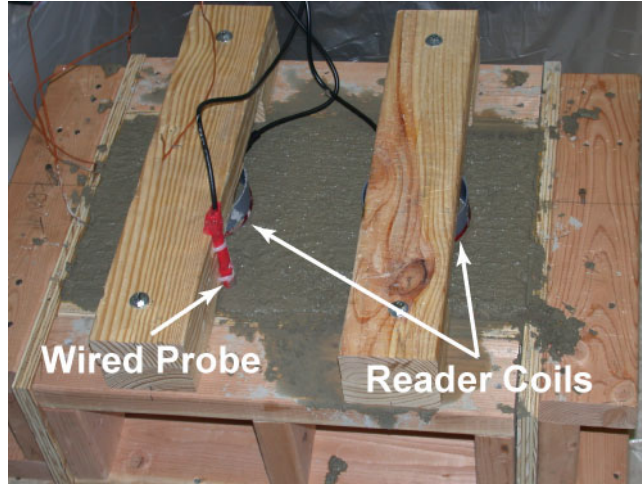


Figure 5.15 Final arrangement of reader coils and wireless probe after casting concrete.

In addition to the prototype sensors, the slab was also wired with three thermocouples for monitoring temperature. One thermocouple was embedded in each of the wireless sensors and the third was placed near the middle of the slab. A fourth thermocouple was used to monitor the air temperature.

In addition to monitoring all of the sensors mentioned above, a shielded reference inductor with a manufacturer-quoted inductance of $2.7 \mu\text{H}$ was also measured to monitor for possible variations caused by equipment drift. The inductance of the reference load was calculated from the imaginary part of the complex impedance as $L_{ref} = \Im\{Z\}/\omega$. This calculation gives a value of L_{ref} at every frequency point in the impedance measurement. The average of L_{ref} over the entire frequency range of a typical measurement was $2.7 \mu\text{H}$, which matched the value quoted by the manufacturer. The coefficient of variation ($\text{CV}(\%) = 100 \cdot (\text{mean}/\text{standard deviation})$) was 0.28%, which suggests that the value of the inductance was stable over the entire measurement range.

A method was created to continuously monitor and record the data from all of the sensors for extended periods of time. All of the sensors were measured in place in the formwork before the concrete was cast to get a reading of the initial state. Once the concrete was cast, readings were taken every five minutes for a period of 48 hours. Unfortunately, due to an automatic WindowsXP update, the computer reset itself at 03:00 hours on the second day of measurements. The problem was not discovered until approximately 12:00 hours, resulting in a nine hour gap in the data. After the initial 48 hour period, the measurement period was reduced to 15 minutes. Once the concrete had been in place for one week, the continuous monitoring was completed and intermittent measurements were made with decreasing frequency for a total of approximately four and one-half months.

As mentioned previously, the value of the reference inductance was relatively stable over the entire frequency range of the impedance measurements. The value of L_{ref} was averaged over each frequency sweep providing one number which could be compared for successive measurements and would hopefully give an indication of variations introduced into the measurements due to the measurement equipment. The value of the reference inductance had a CV of 0.11% over the entire four and one-half month monitoring period, indicating that the system remained relatively stable and it is safe to compare measurements made at different times to one-another.

Figure 5.16 shows pseudoQ of the conductivity sensor as a function of time over the entire measurement period. The pseudoQ increases rapidly immediately after casting and then continues to increase at a much slower rate.

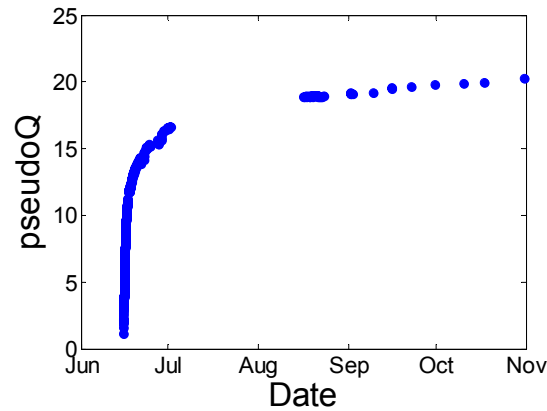


Figure 5.16 The pseudoQ of the conductivity sensor increased rapidly immediately after casting the concrete and then continued to increase at a slower rate throughout the measurement period.

As mentioned previously, in addition to the wireless conductivity sensor, a matching wired probe was also cast in the concrete. Similar to the analysis done on the data from the test in salt water, the conductance of the probe was extracted from both the wireless sensor and the wired probe. The pseudoQ of the wireless sensor was first adjusted using the intrinsic pseudoQ measured before the concrete was cast. Figure 5.17 is a semi-log plot of the probe conductance for the two probes. In order to make the behavior more visible, only the first week of the data is examined at this time. Also, although the data was measured at discrete time intervals, solid lines were used to represent the data to make the figure more readable.

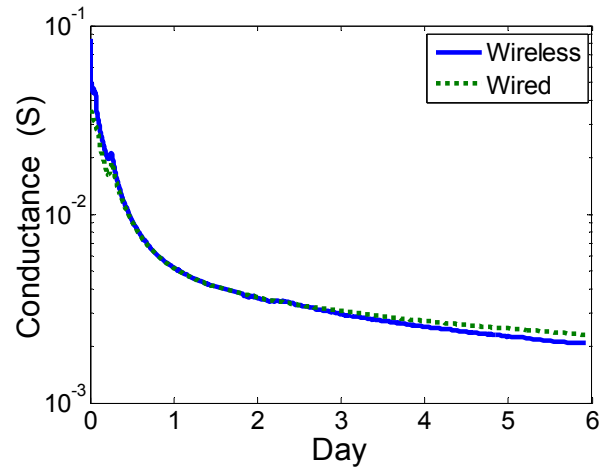


Figure 5.17 The conductance extracted from the wired and wireless probe agree quite well during the initial curing period.

The data from both probes agrees within 10% after the first 6 hours of curing and throughout the rest of the first week. The error during the first 6 hours of curing is attributed to both induction losses in the concrete, which the wired probe is not susceptible to, as well as the fact that the pseudoQ of the wireless sensor is close to one during this time, which is near the limit of the optimum range of sensor sensitivity. Although a previous experiment showed that the induced medium losses were negligible, that experiment was performed on concrete that was already cured. In this case, the concrete was initially in the liquid phase and it is possible that it was conductive enough to cause induction losses.

Figure 5.18 shows the conductance of both probes for the rest of the monitoring period – day 7 through 138.

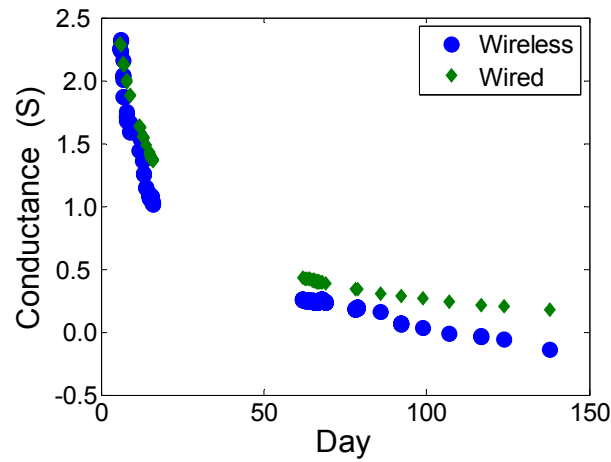


Figure 5.18 As the pseudoQ of the wireless sensor approaches the intrinsic pseudoQ, the error between the wired and wireless probes increases.

As the concrete continues to cure, the difference between the wired and wireless conductivity probes increases. After the first seven days of curing, the pseudoQ of the wireless sensor is approximately three-quarters of the intrinsic pseudoQ measured before casting the concrete. This is well outside of the optimal operating range. Even though attempts have been made to compensate for the intrinsic pseudoQ, when \bar{Q} becomes comparable to \bar{Q}_0 , small errors in measuring pseudoQ translate to large errors in estimating the probe conductance.

Using the wired conductivity probe data, the conductivity of the concrete can be estimated throughout the entire curing process. This data will be useful in designing future versions of the wireless sensor. Figure 5.19 shows the data plotted as the resistivity of the concrete to allow comparison to the values quoted in the literature and presented in Table 5.1.

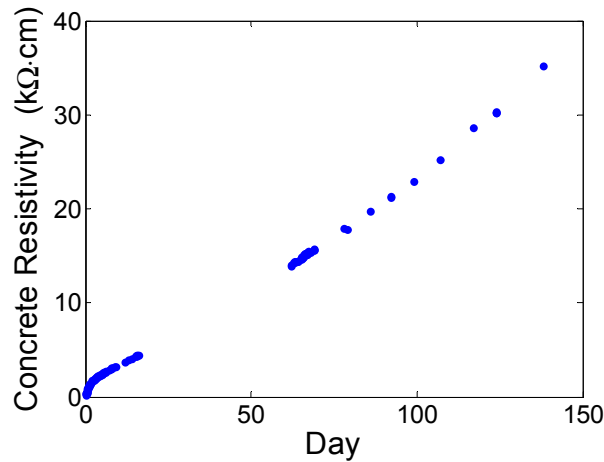


Figure 5.19 Concrete resistivity as a function of curing time.

Although no attempt has been made to deal with potential error due to the electrode-electrolyte interface, the tests of the probe in salt water suggest that the calculated resistivity should be at least the same order of magnitude of the actual resistivity. It is interesting to note that the resistivity is still increasing 140 days after casting the concrete. Also, at day 140, the resistivity measured with the wired probe is approximately one order of magnitude larger than the target resistivity used to design the wireless conductivity sensor.

5.7 POTENTIAL IMPROVEMENTS

There are several possibilities for improving the wireless conductivity sensor in future designs. It would be advantageous to minimize the effects of the reinforcing steel on the intrinsic Q of the sensor. Currently, the sensors are mounted directly to the reinforcement virtually ensuring a strong interaction between the reader coil, the tag, and the rebar. The losses due to the presence of the rebar could potentially be minimized by developing a mounting scheme in which the tag is mounted farther away from the reinforcement. One method of accomplishing this goal would be to include some type of non-conducting mounting bracket in the

sensor housing. This bracket could be designed to quickly and easily attach to the steel reinforcement while keeping the actual inductor coils separated from the rebar.

Improvements are also needed in the design of the conductivity probe electrodes. The electrodes should be redesigned with three considerations in mind. First, the current design is most likely very susceptible to damage during the placement of concrete. Although the sensor may still function if one or both of the wires are bent, the geometry of the probe would no longer be known accurately; thereby introducing error into the extracted conductivity. Unknowingly changing the spacing of the electrodes would also potentially shift the probe conductance away from that specified by the original design guidelines, forcing the sensor to operate outside the optimal range. A more robust electrode design is needed that will allow cement paste to easily fill the gap between the electrodes while at the same time not require any special handling on construction sites.

Different electrode materials should also be considered in future prototype sensors. Copper electrodes were used in the original sensors because of the ready availability of copper wire and the ease of integration into the existing sensor design. The electrode-electrolyte interface effects could potentially be reduced with a more appropriate choice of electrode material. Also, the sensors are expected to be embedded in concrete for long periods of time and the electrodes should be able to withstand the potentially corrosive environment without significant changes that may affect the performance of the sensor.

Finally, the concrete resistivity calculated above using the wired probe along with the guidelines developed in Chapter 3 should allow the electrode impedance to be better matched to the sensing circuit. The current sensors “saturate” at values close to the intrinsic Q for what appears to be relatively low values of concrete resistivity. Future designs should take these factors into consideration to allow the sensors to remain in the optimum operating range at higher resistivities.

5.8 CONCLUSIONS

This chapter discussed the development of a simple resonant wireless conductivity sensor. The sensors were tested in salt water and the results were correlated to secondary measurements of the water conductivity made using a commercial conductivity meter. Although there was some difference in the two measurements, the wireless sensor performed well and demonstrated the ability of the sensor to remotely monitor the conductivity of the medium in which it is embedded.

The sensors were also tested in concrete. Tests in the slabs used for accelerated corrosion tests showed a strong dependence on the wet-dry cycle of the salt water ponds. The dependence of pseudoQ was shown to be due to the interaction of the conductivity probe with the concrete rather than possible induction losses in the concrete between the reader and sensor. The sensors also showed that moisture from the salt water ponds is able to penetrate through the entire slab and reach a sensor that was placed at the bottom of the slab. A conductivity sensor was also monitored continuously as the concrete it was embedded in was curing. Both of these tests revealed that the rebar the sensor is attached to can adversely affect the performance of the sensor, an issue which should be addressed in future designs.

The test of the sensor in curing concrete revealed a strong time dependence as the concrete cured. It is possible that the sensor could potentially be useful in determining when the concrete has cured an appropriate amount. Finally, a wired probe was also included in the concrete curing test. The data from this probe was used to estimate the resistivity of the concrete, which may be useful when designing future versions of the wireless conductivity sensor.

CHAPTER 6

Looking Forward

6.1 ADDITIONAL POTENTIAL SENSORS

The corrosion and conductivity sensors discussed in the previous chapters have undergone significant testing in various environments, including actual concrete. There are several other sensor types which have been proposed and, to a limited extent, evaluated in the laboratory. Several of these sensors are discussed briefly below.

6.1.1 Temperature Sensor

There are many possible applications in which it would be beneficial to have an embeddable temperature sensor. Using the current sensor platform, such a device could be constructed using a temperature dependent resistor or a temperature dependent dielectric. In fact, this effect can be seen in the current prototype corrosion sensors.

Most metals have a temperature dependent conductivity. For example, copper has a temperature coefficient of resistivity of approximately $0.4\% / ^\circ\text{C}$. If the overall change in resistance of the wire used in the tag is large enough, this change in resistance will be visible as a change in pseudoQ. The capacitor in the tag is affected by temperature due to the temperature dependence of the dielectric. Finally, it is also possible the inductance would be affected due to the thermal expansion of the coil. A change in either the capacitance or inductance would affect the resonant frequency of the circuit, which would also change pseudoQ.

In order to examine the temperature effects on the existing sensors, a prototype corrosion sensor was placed in an insulated container. The temperature

inside the container was varied from approximately -14 to 60 °C using hot and cold gel-packs. The temperature was measured using a standard type K thermocouple. Figure 6.1 shows the pseudoQ and resonant frequency of the reference circuit sealed inside the corrosion sensor as a function of temperature.

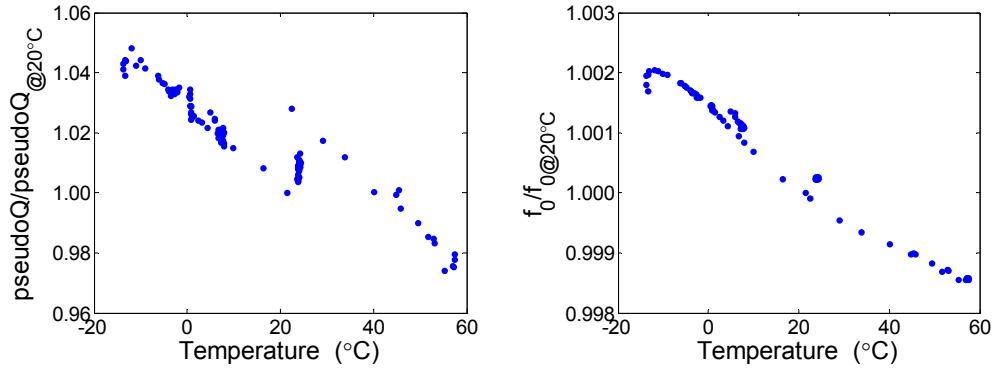


Figure 6.1 Both the pseudoQ and resonant frequency of the sensor are temperature dependent.

Both the pseudoQ and the resonant frequency are clearly dependent on temperature, though there is also some apparent noise in the data. The pseudoQ varies approximately 0.11 %/°C while the resonant frequency varies approximately 0.005 %/°C. As mentioned previously, changes in pseudoQ can be caused by changes in either the resonant frequency of the tag or the loss of the circuit. However, the resonant frequency is not affected by the loss term. Therefore, by using the resonant frequency, it should be possible to separate the changes in pseudoQ caused by changes in L or C from changes in R. Furthermore, based on knowledge of coil geometry and capacitor characteristics, it may be possible to determine if the change in resonant frequency is primarily due to the inductor or capacitor.

Temperature dependent effects can also be seen in the data from the reference circuit of the corrosion sensor that was tested in curing concrete as seen in Figure 6.2. In this case, the values are normalized to their respective mean.

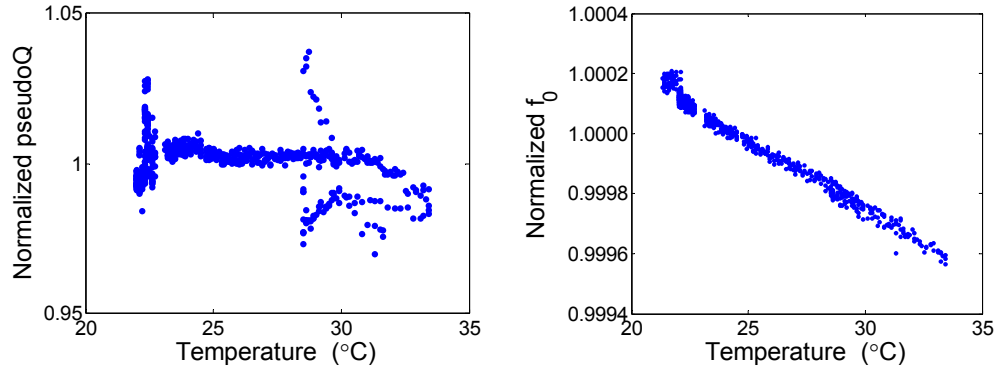


Figure 6.2 The resonant frequency of the corrosion reference circuit in the curing slab shows the same temperature dependence as the previous example.

The resonant frequency shows an almost identical temperature dependence to that of the previous experiment. The data also appears less noisy than the data from the previous experiment, which may be due to the fact that the thermocouple was actually embedded inside the corrosion sensor. In the original experiment, the thermocouple was inside the insulated container near the sensor rather than embedded in the sensor itself, allowing the possibility that the thermocouple and the sensor were not at the same temperature. Such a discrepancy in temperature could explain some of the noise in the original measurements.

The pseudoQ of the corrosion sensor reference circuit shows very little temperature dependence in the second set of data. This may be due to the losses induced in the circuit due to the presence of the rebar dominating any effect the temperature may have had on pseudoQ. It is also possible that the induction losses due to the increased conductivity of the liquid phase concrete helped mask the

effects of temperature during the initial curing period in which most of this data was collected.

The fact that the pseudoQ dependence on temperature is small is beneficial when considering the normal operation of the corrosion and conductivity sensors. Although both the pseudoQ and resonant frequency show some temperature dependence, the effects amount to changes of a few tenths of a percent to a few percent over a 70 degree temperature range.

As initially mentioned, a true wireless temperature sensor could be designed by using a temperature dependent transducer or dielectric. Alternatively, a simple threshold temperature sensor could also be built using a temperature dependent switch. Such a switch could be constructed using a phase change material with a melting point at the desired trigger temperature. This material could hold two spring-loaded contacts together and when the temperature rises above the set-point, the material would melt and allow the contacts to separate. Such a switch could easily be integrated into the existing sensor platform and may be useful in monitoring curing concrete.

Along with corrosion of the reinforcing steel, an additional source of concrete deterioration is delayed ettringite formation (DEF). One of the critical parameters related to DEF is the concrete curing temperature [38]. If the curing temperature exceeds 70 °C, the probability of DEF is greatly increased. A threshold temperature sensor could be designed to trigger at 70 °C and would warn inspectors if the concrete was at increased risk of DEF. Threshold temperature sensors also have applications in other areas. For example, sensors could be designed with low threshold temperatures to monitor frozen goods to ensure they do not thaw and re-freeze.

6.1.2 Humidity Sensor

In addition to temperature, there are many applications in structural health monitoring and elsewhere in which a relative humidity (RH) sensor would be useful. For example, the conductivity of concrete has been shown to be dependent on moisture content as well as other factors [34]. An RH sensor could be embedded in concrete along with a conductivity sensor. It may then be possible to combine the two measurements in order to differentiate between changes in conductivity due to shifting moisture levels from changes due to other affects, such as an altered chloride ion concentration. Additionally, water-based glues are often used to attach flooring to concrete slabs. If the flooring is attached too early, the moisture content of the curing concrete can weaken the glue and cause delamination of the flooring. A relative humidity sensor embedded in the concrete would allow a builder to know when it is safe to place flooring.

There are several types of humidity transducers which are commercially available. Three common types of sensors are capacitive, resistive, and thermal conductivity based transducers [39]. The capacitive and resistive sensors undergo a change in impedance due to changes in RH, usually through the action of a hygroscopic medium attached to a substrate. The thermal based sensors measure the absolute humidity based on the change in the thermal conductivity of air caused by changes in moisture content. The difference between the resistance of two matched thermistors, one exposed to the air and one sealed in a dry gas such as nitrogen, is proportional to the absolute humidity.

Both the capacitive and resistive types of RH transducers could be readily integrated to the existing sensor platform. As a simple test, a capacitive transducer was connected to an inductor coil to form a simple resonant circuit. A magnetically coupled reader coil was used to interrogate the circuit and the resulting phase of the measured impedance for two different RH levels is shown in Figure 6.3. The humidity around the sensor was changed by simply breathing on the transducer.

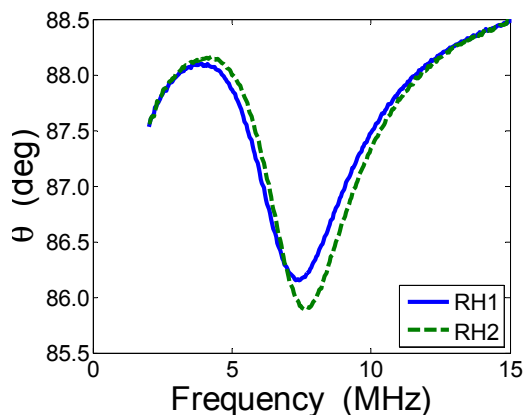


Figure 6.3 Demonstration of a capacitance-based wireless humidity sensor.

No attempt was made to optimize the behavior of this circuit and it simply serves to demonstrate the concept of a wireless humidity sensor.

6.1.3 Micro-fluidic Analysis

The concepts developed in this research are also being applied to the area of micro-fluidic analysis. Advancements are currently being made to allow complex chemical lab work to be done on a single chip requiring only a small amount of reactants. The results of these reactions must then be analyzed, often through complex optical processes that require large, expensive equipment, which undermines one of the advantages of having a lab-on-a-chip.

Researchers at The University of Texas at Austin are working to integrate photo-diodes into current micro-fluidic chips [40]. Coupled with chemiluminescent reactions, the results from such a chip could potentially be read without the cumbersome external optics and illumination sources traditionally used to monitor the reactions on the chip. In order to eliminate the need to make direct electrical connections to the chip, the use of resonant coupling is also being investigated.

The impedance of the integrated photo-diode is a function of the incident light. Specifically, there are changes in the capacitance as well as the resistance of the device. By attaching the diode to an inductor coil, it should be possible to use the techniques developed in this research to interrogate the micro-fluidic chip without requiring direct electrical contact.

6.2 ALTERNATE MEASUREMENT TECHNIQUES

In addition to improving the current prototype sensors as well as developing new sensors, work is also being done to improve the interrogation and data analysis methods currently employed. Two impedance/gain-phase analyzers were used to interrogate the sensors – an HP 4194A and a Solartron 1260A. While both instruments performed well, they are both impractical for long-term use in the field due to size, weight, and cost constraints. A portable cost-effective reader must ultimately accompany any sensor design which is to be deployed in the real world.

While it is possible to design a portable impedance analyzer, it is also possible that the sensors could be interrogated without needing to do a full swept-frequency complex impedance measurement. One possibility is to use a simple AM transmitter to transmit multiple simultaneous sinusoidal waveforms through the reader coil. At least one waveform would be tuned to the resonant frequency of the sensor while the others would be spaced off-resonance. The loading of the reader coil by the resonant tag would have different effects at each of the transmitted frequencies which could be detected by measuring the voltage across the reader coil.

Another possibility is to use a “Q-meter” style circuit. Such a circuit is typically used to measure the Q of an inductor. An example schematic is pictured in Figure 6.4.

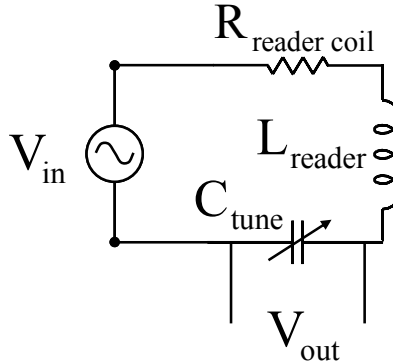


Figure 6.4 Example schematic of a Q-meter circuit which could be used to interrogate the sensor tags.

In the operation of this circuit, the voltage V_{in} is set to oscillate at the frequency at which Q is to be measured. The tuning capacitor is then adjusted to maximize the voltage across C_{tune} . At this point V_{out} is proportional to the Q of the inductor. The Q of the reader coil inductor is affected by the presence of a tag. Preliminary results show that if the oscillator frequency of V_{in} is set to the resonant frequency of the tag, the voltage V_{out} is proportional to Q_{tag} as well as the coupling factor k .

In addition to exploring possible reader alternatives, it may also be beneficial to examine the curve fitting technique used to determine pseudo Q . As already mentioned, there is some error introduced by the curve fitting routine, especially when the tag signal is small. One possibility is to try fitting a full circuit model to the data rather than the lineshapes that are currently used. This would have the advantage of reporting all of the component values. The transducer value would then be a direct output of the circuit fit. Additionally, values that should not typically change, such as the reader and tag inductances, could be cross-checked against expected values to make sure that the fit is reasonable. The coupling factor would also be one of the outputs of the full circuit fit. If the fit is done in real time,

this value could be reported to the inspector and the reader coil could be moved around to attempt to maximize the coupling factor. This could be used to increase the positioning accuracy of the reader coil over the embedded sensor.

A full circuit model fit has been tried using the current prototype sensors and the current circuit model with mixed results. The fit appeared to work well in some cases but not others. One potential reason for the mixed performance of the full circuit model fit is that the model is incomplete. As already mentioned, there are some behaviors, such as the baseline drift sometimes seen in field measurements, that are not adequately explained by the current circuit model. Another possibility is that the current fitting methodology – that is, how the parameter space is searched to attempt to minimize the sum-of-square error between the data and the fit – is inadequate. Currently, the fitting is done in Matlab using the Nelder-Mead Simplex method [41]. It is possible that using a different fitting method that is better suited to problems with a large number of degrees of freedom may provide better results.

6.3 SUMMARY

Although the original motivation of this work was to develop sensors for detecting corrosion in steel reinforced concrete, the general sensor circuit can be applied to many different problems. Examples of other possible sensors include wireless temperature and relative humidity sensors. Both of these sensors would compliment the prototype corrosion and conductivity sensors for use in reinforced concrete structures. Each sensor could also be used in other applications.

One example outside of the realm of structural health monitoring is the adaptation of the sensor design for use in micro-fluidic chips. Accompanied by other innovations in this area, the use of magnetic coupling would allow non-contact interrogation on-chip sensors.

In addition to expanding the sensor platform for use in other areas, there is also the potential to improve the data analysis techniques currently used with the

prototype sensors. One area of interest is in developing a low-cost portable measurement system to take the place of the impedance analyzers currently used. In parallel with developing new reader instrumentation, attention should be given to the post-processing of the data. There is potential for improving the current curve fitting techniques as well as developing a new curve fitting algorithm based on the circuit model of the sensor.

CHAPTER 7

Conclusion

7.1 MOTIVATION OF WORK

The goal of this research was to develop a versatile low-cost passive wireless sensor platform, motivated by a need for a better method of detecting corrosion of reinforcing steel in reinforced concrete structures. Corrosion in concrete is a worldwide problem, particularly in marine environments and on roadways subjected to de-icing salts. The damage caused by the corrosion of the steel reinforcement has a large economic impact due to the direct cost of repairing or replacing structures as well as associated indirect costs such as those incurred due to traffic delays and lost productivity. Current inspection methods are often invasive, expensive, and difficult to interpret. This work presents a new type of sensor which could be embedded inside the concrete and wirelessly interrogated whenever an inspection is needed.

Passive wireless sensors are well suited to structural health monitoring as the sensors can be permanently embedded inside of a structure where future maintenance may be difficult or impossible. In order to be practical in situations where hundreds to thousands of sensors may be installed in a single structure, the sensors must have low per-unit costs as well as low operating costs. Additionally, the sensors must be able to withstand traditional construction techniques without significant special handling.

Several existing and emerging technologies were examined to provide a comparison point for this work. Two of the most common passive wireless systems, EAS and RFID tags, were discussed as potential starting points for developing new sensors. EAS systems are based on simple resonant tags which are wirelessly

interrogated at the store exit. These tags represent a truly low-cost product and can be purchased for less than \$0.04 each. The tags are effectively one-bit sensors that can be used to set off an alarm if they are not deactivated at the store checkout. RFID tags are based around low-power integrated circuits which are powered inductively through the reader that is used to interrogate the tags. These tags have the potential to transmit more data than a simple EAS tag and some RFID systems are capable of being integrated with external sensors. However, the increased capabilities of RFID tags come at a higher per-tag cost.

Several sensors which are under development for monitoring reinforced concrete structures were also examined. One proposed sensor design includes an electrolytic cell in a passive wireless sensor package for monitoring chloride ion concentration in concrete. Elevated chloride ions are believed to be one of the dominant causes of corrosion of the reinforcing steel. However, the sensor is difficult to calibrate and is subject to drift over time. It is also not clear that a liquid electrolyte will last throughout the long timeframes necessary for monitoring concrete structures.

A corrosion sensor package which is currently commercially available is the ECI-1. The sensor appears to offer several potentially useful measurements typically used when inspecting concrete structures. However, it is a wired sensor and any wires which must break the surface of the concrete provide potential ingress paths for moisture and chloride ions into the concrete. At a per-unit cost of approximately \$2,000 USD, these sensors are impractical for installation in structures which require a large number of sensors. Also, the installation costs associated with wired sensors would most likely be higher than those for wireless sensors.

7.2 SENSOR DESIGN GUIDELINES

A passive wireless platform based on simple resonant LC circuits was proposed for the embedded sensor design. The sensors are interrogated by measuring the input impedance of a reader coil which is magnetically coupled to a second coil in the sensor. Changes in the sensor circuit are reflected in the input impedance of the reader coil.

Several possibilities for extracting data from the measured impedance were considered. Ultimately, it was found that the ratio of the resonant frequency to the width of the resonance was proportional to the losses in the sensor circuit. The width and the resonant frequency were combined into a single parameter called the pseudoQ, which is related to the quality factor of the circuit. It is possible to detect changes in the sensor caused by a resistance-based transducer by monitoring the pseudoQ of the circuit. An advantage of using pseudoQ over other possible measurands is that it is relatively independent of the coupling between the reader and the sensor. The coupling factor is dependent on the sixth power of the distance between the reader and the sensor. Due to the potential for variations in this distance, it is desirable to use a measurand which is not strongly dependent on the coupling factor.

An idealized form of the proposed sensor circuit was used to investigate the affects of the various circuit parameters. A metric was developed for assessing the sensitivity of pseudoQ to these changes and based on the analysis of the circuit model, a set of guidelines was developed to aid in initial sensor development. The idealized circuit model was then expanded to include real-world effects based on the geometry of the reader and tag coils as well as potential parasitic losses.

A second resonance was also added to the tag circuit to serve as a reference when the sense resonance becomes too small to detect. The effects of the additional resonant circuit on the sensor behavior were examined and the design guidelines

were expanded to include comments on the relationship between the sense and reference resonances.

A curve fitting routine, which is designed to remove the baseline reader coil affects from the measured data and estimate the pseudoQ of one or two resonances, was developed to aid in the analysis of the sensor data. In steel reinforced concrete the reader coil interacts with the embedded rebar which makes calculating or measuring the baseline difficult. While it would be possible to take a baseline measurement with no sensor present, a measurement at one location may not exactly correspond to the baseline in another location due to variations in the rebar embedded in the concrete.

The general circuit topology of the sensor platform is shown in Figure 7.1 and the design guidelines are summarized below.

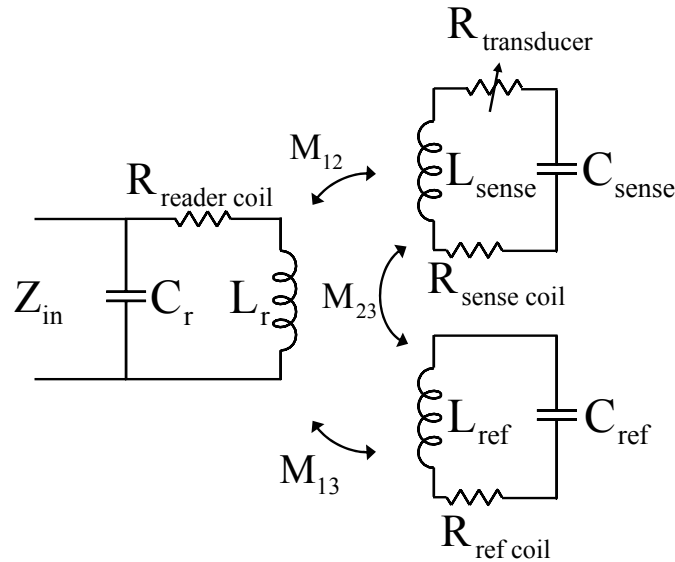


Figure 7.1 Circuit diagram of resistance-based sensor circuit with reference resonance.

- $3 \cdot R_{sensecoil} \leq R_{transducer} \leq \omega_0 L_{sense}$, which can also be expressed as $1 \leq \bar{Q} \leq \frac{1}{4} \bar{Q}_0$, where \bar{Q} is the measured pseudoQ and \bar{Q}_0 is the intrinsic pseudoQ due to parasitic losses in the circuit.
- Tag coils should be designed to fill the maximum dimensions as dictated by constraints of the sensor application. The coil should be made with one turn of a conductor that fills the space. Care should be taken to ensure the conductor is thick enough to avoid skin-depth limitations.
- The sensor should be designed with the highest possible operating frequency given constraints such as allowable operating bands, equipment capabilities, available components, and coil self-resonances.
- Due to flux shielding of the higher resonance by the lower resonance, the sense circuit should have the lower of the two resonant frequencies.
- In concentric coil designs, where one of the coils is smaller and set inside of the other coil, the sense coil should be the larger of the two.

7.3 PROTOTYPE SENSORS

Two prototype sensors were developed and tested for use in reinforced concrete. The first is a sensor designed to monitor for corrosion in steel. The sensor consists of the previously discussed resonant circuit with a piece of exposed steel wire as the sensing element. When the sensor is embedded in concrete, the wire is exposed to the same environment as the reinforcing steel and is subject to the same corrosive effects. As the wire corrodes, the resistance of the wire changes, which is reflected in the pseudoQ of the sensor. Once the wire completely corrodes, the sense resonance is fully damped and only the reference resonance remains.

Tests of the sensor in concrete revealed that the pseudoQ of the sensor did indeed change over time as the wire corroded. This change occurred faster than originally expected and in practice, if the sensors are interrogated infrequently, it may be possible for the wire to completely transition from intact to broken between successive measurements. Nevertheless, there was a strong correlation between the sensor response and corrosion of the actual reinforcing steel of the concrete. As is, the sensor is useful as a simple threshold sensor and may still be potentially useful in estimating a corrosion rate depending on how long the wire takes to corrode in real world environments.

Several possible improvements were suggested for the sensor including electrically connecting it to the reinforcing steel in an attempt to monitor a wider area than that covered by the sensing wire. The possibility of using a sacrificial material, such as zinc, in the sensor was also discussed. In such a system, the zinc would be designed to corrode while protecting the steel. As the zinc corrodes, the response of the sensor would change, potentially alerting inspectors of the need for repairs before the steel has begun to corrode.

In addition to the corrosion sensor, an embeddable conductivity sensor was also developed and tested. The resistivity of concrete has been related to the rate at which corrosion occurs. Chloride ions also play a significant role in the corrosion of steel in concrete and an embedded conductivity sensor may provide one part of a solution to detect elevated chloride ion levels.

The topology of the original circuit is altered by placing the transducer in parallel with the capacitor in the sense circuit. This allows the circuit to work at relatively low conductivities as might be expected in concrete. A simple conductivity probe was constructed from two parallel copper wires. Both wireless sensors as well as wired probes were created using the design. The wired probes were used to provide a cross-check of the wireless sensors.

Prototype conductivity sensors were tested in concrete as well as salt water. The tests in salt water provided a simple method of testing the sensors in a medium in which the conductivity could easily be changed. Measurements made with a commercial conductivity meter were compared against the results obtained from the prototype sensors. Both the wired and wireless probes correlated fairly well with each other as well as with the commercial conductivity meter. Potential sources of error, such as electrode-electrolyte interface effects, were also discussed. Overall, these errors were relatively low and the tests demonstrated the viability of the wireless conductivity sensor.

The conductivity sensors were also tested in concrete. Several sensors were embedded in slabs used for accelerated corrosion tests of the aforementioned corrosion sensors. The pseudoQ of the conductivity sensors strongly correlated to the wet-dry cycle of salt water ponds used in the testing. This indicated that the sensors were responsive to changes in the concrete environment. Unfortunately, the resistivity of the cured concrete was such that the transducer impedance of the conductivity probe was very high. It was also found that the presence of the rebar in the concrete appeared to lower the intrinsic Q of the sensor. These two effects combined caused the pseudoQ of the sensor to be approximately equal to the intrinsic Q which made measuring the conductivity with the wireless sensor difficult.

A conductivity sensor was also monitored throughout the curing process of a concrete test slab. The pseudoQ of the sensor was strongly dependent on the amount of curing time due to changes in the conductivity as the cement cured. In addition to the wireless sensor, a wired conductivity probe was also included in the curing concrete. The two sensors agreed fairly well during the initial curing of the concrete. The wireless sensor experienced depression of the intrinsic Q due to the presence of the rebar in the test slab. The low intrinsic Q of the sensor introduced potentially large errors into the extraction of the concrete resistivity. The wired

probe, however, was not subject to such limitations. The data from the wired probe was used to estimate the resistivity of the concrete throughout the curing process and will be useful in designing future conductivity sensors.

Potential areas for improvement in future designs were also discussed. An attempt should be made to minimize the effects of the reinforcing steel in the concrete on the intrinsic Q of the sensor. One possible method for doing this would be to develop a mounting method which attaches the sensor housing to the rebar while keeping the inductor coils a safe distance away.

Suggestions were also provided for improving the electrode design. A more robust design is needed for the sensor to be deployed in the real world under normal construction procedures. Additionally, the electrode chemistry with the concrete should be considered in selecting the material for probe designs. Finally, using the sensor design guidelines, the probe could be better matched to the sensor circuit and the expected concrete resistivity.

7.4 ALTERNATIVES

While the driving force in the development of these sensors has been the use of the sensors to monitor for corrosion in steel reinforced concrete, the general sensor design can be adapted to many different types of impedance-based transducers with many potential applications. The idea of a wireless temperature sensor was discussed. The behavior of the current prototype sensors was analyzed as a function of temperature and although there are clearly temperature effects in the pseudo Q and resonant frequency of the sensor, these effects are quite small. The small temperature dependence is good for the corrosion and conductivity sensors as moderate temperature changes would have little effect on the sensor output.

A true temperature sensor could be created by the inclusion transducer with large temperature dependence. A threshold temperature sensor could also be created through the use of phase-change materials in a spring loaded switch. Such a

sensor may be useful in during concrete cure to detect the possibility of delayed ettringite formation. Threshold temperature sensors would also be useful in other applications where a certain threshold should not be exceeded. For example, a sensor could be developed to monitor frozen goods to ensure they do not thaw and re-freeze.

The sensor platform could also be used to construct a relative humidity sensor using commercial off-the-shelf humidity transducers. These sensors could be used in conjunction with the conductivity sensors to separate changes in conductivity due to shifting moisture levels from changes due to other effects, such as an increasing chloride ion concentration. Embeddable relative humidity sensors could also provide feedback as to when it is safe to place flooring over concrete slabs. If flooring is laid down too early, moisture from the still curing concrete can break down the water-based glues used and cause delamination.

The concept of wirelessly measuring an impedance through a magnetically coupled circuit may also be useful in lab-on-a-chip applications. Using integrated electronics on such a chip, it may be possible to analyze the results of chemical reactions without the need for direct electrical contacts.

7.5 FINAL THOUGHTS

An important part of this research has been the constant consideration of real-world effects on the sensor design. Research often leads to concepts which look great on paper or perform well in laboratory simulations. Unfortunately, performance in the lab does not always translate to performance in the real world. Constraints such as cost and size are often ignored in the initial phases of design. While disregarding certain constraints can be useful in the initial development of an idea, it is important to keep in mind how the constraints will ultimately factor into the design.

It is also important to test concepts in situations that are representative of how the final product might actually be used. The sensors developed through this research have been tested in various environments including concrete. Testing in concrete has revealed several behaviors which have resulted in adjustments to future designs. The sensors have also been subjected to typical construction techniques without significant special handling. Figure 7.2 shows two sensors attached to the rebar of an elevated concrete bridge as workers cast the concrete deck.



Figure 7.2 Wireless sensors in place during typical construction process.

Six sensors were placed in this bridge and all six survived intact and could be interrogated after the concrete had cured.

The sensor circuit and the accompanying interrogation methods represent a versatile platform which can be tailored to a variety of different applications. Although there is still room for improvement, the prototype corrosion and conductivity sensors have performed well during testing. These sensors have the

potential to greatly improve the ability to monitor reinforced concrete structures throughout their design lives.

References

- [1] Los Alamos National Laboratory, "Structural Health Monitoring," http://www.lanl.gov/projects/damage_id/projects/SHM/index.shtml, 2006.
- [2] Koch, G.H., Brongers, M.P.H., Thompson, N.G., Virmani, Y.P., and Payer, J.H., "Corrosion Cost and Preventive Strategies in the United States," Office of Infrastructure Research and Development: Federal Highway Administration, FHWA-RD-01-156, September 30 2001.
- [3] Grizzle, K.M., "Development of a Wireless Sensor Used to Monitor Corrosion in Reinforced Concrete Structures," M.S. Thesis, Dept. of Civil Engineering, The University of Texas at Austin, 2003.
- [4] Korenska, M., Pazdera, L., Palkova, M., Korenska, M., and Ritickova, L., "Diagnostic of Rebar Corrosion Within Reinforced Concrete Specimens by Resonant Inspection," European Conference on Non-Destructive Testing, pp. 7, June 17-21 2002.
- [5] Gu, P. and Beaudoin, J.J., "Obtaining Effective Half-Cell Potential Measurements in Reinforced Concrete Structures," *Institute for Research in Construction: Construction Technology Update*, vol. 18, No. 4, July 1998.
- [6] ASTM C876, "Standard Test Method for Half-Cell Potentials of Uncoated Reinforcing Steel in Concrete," American Society for Testing and Materials, West Conshohocken, PA, 1999.
- [7] Novak, L.J., Grizzle, K.M., Wood, S.L., and Neikirk, D.P., "Development of state sensors for civil engineering structures," Proceedings of SPIE, Smart Structures and Materials 2003 - Smart Systems and Nondestructive Evaluation for Civil Infrastructures, vol. 5057, pp. 358-363, 2003.

- [8] Grizzle, K.M., Simonen, J.T., Andringa, M.M., Wood, S.L., and Neikirk, D.P., "Wireless sensors for monitoring corrosion in reinforced concrete members," Proceedings of SPIE, Smart Structures and Materials 2004 - Smart Systems and Nondestructive Evaluation for Civil Infrastructures, pp. 10, March 2004.
- [9] Simonen, J.T., Andringa, M.M., Grizzle, K.M., Wood, S.L., and Neikirk, D.P., "Wireless sensors for monitoring corrosion in reinforced concrete members," Proceedings of SPIE, Smart Structures and Materials 2004 - Sensors and Smart Structures Technologies for Civil, Mechanical, and Aerospace Systems, vol. 5391, pp. 587-596, March 2004.
- [10] Dickerson, N.P., Simonen, J.T., Andringa, M.M., Wood, S.L., and Neikirk, D.P., "Wireless low-cost corrosion sensors for reinforced concrete structures," Smart Structures and Materials 2005 - Sensors and Smart Structures Technologies for Civil, Mechanical, and Aerospace Systems, pp. 493-503, 2005.
- [11] Andringa, M.M., Puryear, J.M., Neikirk, D.P., and Wood, S.L., "Low-cost wireless corrosion and conductivity sensors," Proceedings of SPIE, Smart Structures and Materials 2006 - Sensors and Smart Structures Technologies for Civil, Mechanical, and Aerospace Systems, vol. 6174 I, 2006.
- [12] Landt, J., "The history of RFID," *Potentials, IEEE*, vol. 24, No. 4, pp. 8-11, 2005.
- [13] Association for Automatic Identification and Mobility, "Electronic Article Surveillance (EAS): An Overview of the Major Technologies," <http://www.aimglobal.org/technologies/eas/easoverview.asp>, 2006.
- [14] SecurityTagStore, "Checkpoint Series 410 Label," http://www.securitytagstore.com/product.aspx?name=Checkpoint_Series_410_Label_White, 2006.
- [15] Zimmermann, D. and Loughheed, J.H., *Encapsulated Electrically Resonant Circuit And Interrogating Apparatus And Method For Finding Same In Various Locations*, United States Patent 3,836,842, Bell Canada-Northern Electric Research Limited, 17 September 1974.

- [16] Microchip Technology, "microID™ RFID Devices," <http://www.microchip.com/1000/pline/frequency/rfcats/rfid/devices/mcrf202/index.htm>, 2003.
- [17] MicroStrain, "EmbedSense™ RFID Sensor Tag," <http://www.microstrain.com/embed-sense.aspx>, 2004.
- [18] Watters, D.G., et al., "Smart Pebble™: Wireless sensors for structural health monitoring of bridge decks," *Proceedings of SPIE, Smart Structures and Materials 2003*, vol. 5057, pp. 20-28, 3-6 March 2003.
- [19] Fortner, B., "Embedded Miniature Sensors Detect Chloride in Bridge Decks," *Civil Engineering*, vol. 73, No. 6, pp. 42-43, June 2003.
- [20] Carkhuff, B. and Cain, R., "Corrosion Sensors for Concrete Bridges", *IEEE Instrumentation and Measurement Magazine*, vol. 6, pp. 19-24, June 2003.
- [21] Simonen, J.T., "Development of an Embedded Wireless Corrosion Sensor for Monitoring Corrosion in Reinforced Concrete Members," M.S. Thesis, Dept. of Civil Engineering, The University of Texas at Austin, 2004.
- [22] Andringa, M., "Development of a Passive Wireless Analog Resistance Sensor," M.S. Thesis, Dept. of Electrical and Computer Engineering, The University of Texas at Austin, 2003.
- [23] Grover, F., *Inductance Calculations: Working Formulas and Tables*. New York: Dover, 1973.
- [24] Ramo, S., Whinnery, J.R., and VanDuzer, T., *Fields and Waves in Communication Electronics*, Second ed. New York: John Wiley & Sons, 1984.
- [25] Sedra, A.S. and Smith, K.C., *Microelectronic Circuits*, Fourth ed. New York: Oxford University Press, 1998.
- [26] Nainani, P.R., "Optimization of Passive Wireless Concrete Corrosion Sensors Using the Genetic Algorithm," M.S. Thesis, Dept. of Electrical and Computer Engineering, The University of Texas at Austin, 2004.

- [27] Iskander, M.F., *Electromagnetic Fields and Waves*. Englewood Cliffs, New Jersey: Prentice-Hall, 1992.
- [28] Dickerson, N.P., "Wireless Corrosion Sensors for Reinforced Concrete Structures," M.S. Thesis, Dept. of Civil Engineering, The University of Texas at Austin, 2005.
- [29] Dickerson, N.P., Andringa, M.M., Puryear, J.M., Wood, S.L., and Neikirk, D.P., "Wireless threshold sensors for detecting corrosion in reinforced concrete structures," *Proceedings of SPIE, Smart Structures and Materials 2006 - Sensors and Smart Structures Technologies for Civil, Mechanical, and Aerospace Systems*, vol. 6174 I, pp. 61741, 2006.
- [30] Personal Communication with Puryear, J.M., The University of Texas at Austin, 2006.
- [31] Carino, N.J., "Nondestructive Techniques to Investigate Corrosion Status in Concrete Structures," *Journal of Performance of Constructed Facilities*, vol. 13, No. 3, pp. 96-106, August 1999.
- [32] Hayt, W.H., *Engineering Electromagnetics*, Fifth ed. New York: McGraw-Hill, Inc., 1989.
- [33] Personal Communication with Folliard, K., The University of Texas at Austin, 1 February 2005.
- [34] Wilson, J.G., Whittington, H.W., and Forde, M.C., "Dielectric Properties of Concrete at Different Frequencies," *Proceedings of Institution of Electrical Engineers, Dielectric Materials, Measurements and Applications*, vol. 239, pp. 157-160, 10-13 September 1984.
- [35] Bungey, J.H. and Millard, S.G., *Testing of Concrete in Structures*, Third ed. London: Chapman & Hall, 1996.
- [36] "Drinking Water Quality Report," City of Austin, September 2006.
- [37] Geddes, L.A., *Electrodes and the Measurement of Bioelectric Events*. New York: Wiley-Interscience, 1972.

- [38] Collepardi, M., "A state-of-the-art review on delayed ettringite attack on concrete," *Cement & Concrete Composites*, vol. 25, No. 401-407, 2003.
- [39] Roveti, D.K., "Choosing a Humidity Sensor: A Review of Three Technologies", *Sensors Magazine*, 1 July 2001.
- [40] Park, Y.S., Andringa, M.M., Neikirk, D.P., Hewage, H.S., and Anslyn, E.V., "Smart microplates: integrated photodiodes for detecting bead-based chemiluminescent reactions," 5th IEEE International Conference on Sensors, 22-25 October 2006.
- [41] Lagarias, J.C., Reeds, J.A., Wright, M.H., and Wright, P.E., "Convergence Properties of the Nelder-Mead Simplex Method in Low Dimensions," *SIAM Journal of Optimization*, vol. 9, No. 1, pp. 112-147, 1998.

Vita

Matthew Michael Andringa was born in 1978 to Michael and June Andringa. Matthew attended Plano Senior High School and graduated as the valedictorian in May of 1997. In the fall of 1997, Matthew entered the College of Engineering at The University of Texas at Austin and graduated summa cum laude with his Bachelor of Science in Electrical Engineering in May of 2001. He continued on at The University of Texas at Austin, pursuing his Master of Science in Engineering under the direction of Dr. Dean P. Neikirk at the Microelectronics and Engineering Research Center. Matthew completed his Master of Science in August of 2003 and continued on in the pursuit of his Doctor of Philosophy. Matthew qualified for candidacy at The University of Texas at Austin in December of 2005.

Permanent Address: 4409 Early Morn Dr., Plano, TX 75093

This dissertation was typed by the author.